NONSTEADY FLUID MECHANICS OF VEHICLES IN TUBES

Thesis by

Magdi Hanna Rizk

In Partial Fulfillment of the Requirements

For the Degree of

Doctor of Philosophy

California Institute of Technology

Pasadena, California

1974

(Submitted April 26, 1974)

ACKNOWLEDGMENT

The author is most grateful to Professor T. Kubota for his advice and for many valuable discussions during the course of the research.

The author wishes to thank Professor H. W. Liepmann and Professor B. Sturtevant for offering generous financial assistance during graduate study. He wishes to thank the Link Foundation for its fellowship support.

Sincere appreciation is extended to Mrs. Virginia Conner for her excellent typing of this thesis, and to Mrs. Betty Wood for the graphs.

The author thanks his parents for their continuous support and encouragement.

ABSTRACT

A theoretical study is performed to investigate the drag experienced by vehicles travelling in tubes, the pressure distribution and flow velocities resulting from the vehicle's motion. The study deals with both the cases of vehicles accelerating from rest in the tube and vehicles entering a tube at finite speed. The effect of having a vent in the tube is also studied.

The unsteady compressible equations are used to describe the flow in the tube. Before the boundary layer fills the tube, an inviscid core-boundary layer formulation is used. However, it is found that the simpler one-dimensional formulation is adequate for describing the flow in the tube. The quasi-steady near-field assumption agrees well with the unsteady near-field solution except for the initial period of low velocities.

The solution is compared to that in which compressibility is neglected. It is found that the effect of compressibility is not large for short tubes, low blockage ratios and small velocities. However, its importance increases as the values of these parameters increase. Compressibility may not be neglected during the initial period in the case of vehicles entering tubes at finite speeds.

TABLE OF CONTENTS

TABLE OF CONTENTS (Cont'd)

LIST OF TABLES

LIST OF FIGURES

LIST OF FIGURES (Cont'd)

LIST OF FIGURES (Cont'd)

Figures for the Appendices:

LIST OF APPENDICES

NOMENCLATURE

a^* Speed of sound

a_o^* Speed of sound for the undisturbed condition

$a = \dfrac{a^*}{a_o^*}$

c_s^* Shock wave velocity

$c_s = \dfrac{c_s^*}{a_o^*}$

C_D Drag coefficient $= \dfrac{\text{Drag}}{(\frac{1}{2}\rho_o^* V^{*2}) \times (\text{vehicle c.s. area})}$

C_{D_o} Drag coefficient $= \dfrac{\text{Drag}}{(\frac{1}{2}\rho_o^* V_o^{*2}) \times (\text{vehicle c.s. area})}$

C_{pB} Base pressure coefficient $= \dfrac{p_B^* - p_3^*}{\frac{1}{2}\rho_3^* (V^* - U_3^*)^2}$

$C_{\Delta psi}$ Vent coefficient (inflow) $= K_i^2 \dfrac{p_o^* - p_a^*}{\frac{1}{2}\rho_a^* U_{vt}^{*2}}$

$C_{\Delta pso}$ Vent coefficient (outflow) $= K_o^2 \dfrac{p_a^* - p_o^*}{\frac{1}{2}\rho_a^* U_{vt}^{*2}}$

D^* Drag

D_F^* Skin friction drag

D_p^* Pressure drag

D_{pa}^* Pressure drag which would result if there were no friction forces in the annular region (for the actual flow velocities)

D_{pb}^* Pressure drag component resulting from the pressure drop in the annular region due to frictional forces on the tunnel wall

NOMENCLATURE (Cont'd)

D^*_{pc} Pressure drag component resulting from the pressure drop in the annular region due to frictional forces on the vehicle surface

e^* Acceleration of average flow velocity

f Friction factor $= \dfrac{|\tau^*|}{\frac{1}{2}\rho^* \times (\text{flow velocity relative to the surface})^2}$

$f(\eta)$ Similarity velocity profile in the boundary layer $= \dfrac{u^*(x, \eta, t)}{\hat{U}^*(x, t)}$

$g(r)$ Similarity velocity profile for tube flow $= \dfrac{u^*(x, r, t)}{\hat{U}^*(x, t)}$

h^* Enthalpy

K_i Vent constant (inflow)

K_o Vent constant (outflow)

L^* Tube length

L $= \dfrac{L^*}{L^*} = 1$

L^*_{vh} Vehicle length

L_{vh} $= L^*_{vh}/L^*$

M_o $= \dfrac{V^*_o}{a^*_o}$

p^* Pressure

p^*_o Pressure for the undisturbed condition

p $= \dfrac{p^*}{p^*_o}$

P Ring (band) source strength density

q^* Rate of heat transfer per unit area

NOMENCLATURE (Cont'd)

q $= \dfrac{q^*}{\rho_o^* V_o^{*3}}$

q_o^* Rate of heat transfer at tunnel wall

q_o $= \dfrac{q_o^*}{q_o^* V_o^{*3}}$

Q_{vh} = q at vehicle surface

Q_{TA} = -q at tunnel wall in annular region

Q Point source strength

r^* Radial coordinate

r $= \dfrac{r^*}{W^*}$

R^* Gas constant for air

R^* Radius of inviscid core

R $= \dfrac{R^*}{W^*}$

t^* Time

t $= t^* \dfrac{a_o^*}{L^*}$

$\bar{t}$ $= t^* \dfrac{U_o^*}{W^*}$

T Temperature

u^* Flow velocity in the x-direction

u $= \dfrac{u^*}{V_o^*}$

NOMENCLATURE (Cont'd)

$\bar{u}$ $= \dfrac{u^*}{U_o^*}$

U^* Average flow velocity in the x-direction

U $= \dfrac{U^*}{V_o^*}$

$\bar{U}$ $= \dfrac{U^*}{U_o^*}$

$\hat{U}^*$ Flow velocity in the inviscid core or at the tube centerline

$\hat{U}$ $= \dfrac{\hat{U}^*}{V_o^*}$

$\bar{\hat{U}}$ $= \dfrac{\hat{U}^*}{U_o^*}$

U_o^* Maximum average flow velocity

U_v Dimensionless average velocity in vehicle fixed coordinates = U-V

v^* Flow velocity in the r-direction

v $= \dfrac{v^*}{K V_o^*}$

V^* Vehicle velocity

V_o^* Maximum vehicle velocity

V $= \dfrac{V^*}{V_o^*}$

W^* Tunnel radius

W $= \dfrac{W^*}{W^*} = 1$

NOMENCLATURE (Cont'd)

x^*	Running coordinate along tube axis
x	$= \frac{x^*}{L^*}$
$\bar{x}$	$= \frac{x^*}{W^*}$
X^*	Fixed coordinate to vehicle axis
X	$= \frac{X^*}{L^*}$
y^*	$= W^* - r^*$
y	$= \frac{y^*}{W^*}$
γ	Ratio of specific heats
δ^*	Boundary layer thickness
δ	$= \frac{\delta^*}{W^*}$
η	$= \frac{y^*}{\delta^*}$
κ	$= \frac{W^*}{L^*}$
ρ^*	Air density
ρ_o^*	Air density for the undisturbed condition
ρ	$= \frac{\rho^*}{\rho_o^*}$
σ	Blockage ratio $= \frac{\text{vehicle c.s. area}}{\text{tube c.s. area}}$
σ_{vt}	$= \frac{\text{vent c.s. area}}{\text{tube c.s. area}}$

NOMENCLATURE (Cont'd)

τ^*	Shear stress
τ	$= \dfrac{\tau^*}{\rho_o^* V_o^{*2}}$
$\bar{\tau}$	$= \dfrac{\tau^*}{\rho_o^* U_o^{*2}}$
τ_o^*	Shear stress at tunnel wall
τ_o	$= \dfrac{\tau_o^*}{\rho_o^* V_o^{*2}}$
ψ	Stokes' stream function

Subscripts:

a	Conditions in the tunnel upstream of the vent
b	Conditions in the tunnel downstream of the vent
B	vehicle base
T	Tube inner surface
TA	Tube inner surface at the annular region
vh	Vehicle surface
vt	vent
1	Forward far-field, near-field interface
2	Forward end of the annular region
3	Rear end of the annular region
4	Rear far-field, near-field interface
5	Contact surface

I. INTRODUCTION

Trains moving in tubes experience drag forces which may be orders of magnitude higher than when in free air. A knowledge of such forces and their dependent parameters is essential in determining the tube optimal ventilation design as well as the moving and braking powers. As passengers are to be found in stations along the tube, a study of the air flow and pressure changes caused by the train's motion is also of importance.

The piston action of the train causes the air in the tube to move with a velocity which is dependent on the train speed and blockage ratio. When in steady state, the tube and train friction forces are the only cause of the drag. When in unsteady motion (acceleration), the fluid particles are accelerated, causing an additional inertial drag on the train. During the initial moments of a train's acceleration from rest in a tube, simple compression waves raise the pressure in front of the train, and simple expansion waves decrease the pressure behind it, causing thrust and suction respectively at these two ends. The waves reflect from the tube ends and interact with the train's forward and rear ends affecting the pressure and drag. Viscosity, which is the cause of frictional drag, has the effect of attenuating the strength of the pressure waves propagating through the tube, thus decreasing their effectiveness. Consequently wave drag and frictional drag are coupled and in general may not be studied separately.

The problem of a train entering a tube at finite velocity is of interest. In this case a sharp drag increase is experienced as the tube stagnant air is suddenly met. The sudden motion caused by the

entering train results in the propagation of a weak shock wave down the tube, raising the pressure and producing a sudden air flow at stations along the tube. A similar but less severe result occurs as a train passes a vent shaft.

Previous work in this field includes both experimental and theoretical efforts. Reference (1) describes experiments performed in a water tunnel to measure forces on models intended to simulate vehicles travelling in tubes. In this case the models were at rest with respect to the tube wall. Water was preferred to air as a working fluid, since the lower kinematic viscosity of the former allows the experiments to be conducted at Reynolds number closer to those attained in full-scale operations. The experimental portion of the work reported in references (2, 3) consists of measuring the velocity and thus the drag coefficient of spherical and cylindrical models dropped through vertical tubes submerged in different test fluids (water, glycerin, and others). The tubes used were 4-ft. long and the Reynolds number, based on model diameter and absolute velocity, varied from 1.0 to 5×10^5. Similar experiments are described in reference (4). However, a longer tube was used (12-ft.) and higher Reynolds numbers were achieved (2.5×10^6). Reference (5) describes experiments for measuring the drag and air flow resulting from the motion of a small-scale train in a small-scale tunnel (300 ft. long, 1-ft. diameter). The geometry of the model vehicle was similar to the corresponding full-scale geometry. Also, it was possible to control the vehicle's velocity profile (an electric motor was the source of power driving the vehicle). However, as the experiments were

conducted in air, full scale Reynolds number was not approached.

An experimental program has been conducted at the Jet Propulsion Laboratory in Pasadena (7, 8) for the purpose of obtaining information about the aerodynamic characteristics of vehicles travelling in tunnels under primarily equilibrium conditions. A family of 2-in. diameter vertical tubes of lengths 32-ft., 70-ft., 120-ft. was constructed. Train models were launched through the tubes, using gravity as a constant source of propulsive force. Using the three facilities, data were obtained for a wide range of Reynolds number. The 120-ft. facility had the capability of operating with either open, restricted, or closed-end test sections. The ability to operate it at ambient pressures from 0.1 atm. to 50 atm., made it possible to gather data at Reynolds number as high as 4×10^6. Besides air, CO_2 and Freon-12 were used in the experiments.

Theoretical work in the field includes the studies of references (2, 3) which deal with the laminar steady flow that exists when a semi-infinite cylinder moves at constant velocity in an infinite concentric tube. Sajben (9) uses an incompressible, one-dimensional fluid model to study the dynamic characteristics of vehicles moving in long finite tubes. Reference (11) is an attempt to divide the solution into two parts: a short time solution for the flow, steady in a coordinate system fixed in the initial waves produced by a vehicle's sudden motion; and a long time solution, steady in a vehicle-fixed coordinate system. Only infinitely long tubes are considered. The previous work is continued by Hammitt in reference (13). In (14) the wave and friction effects are decoupled. On that basis the problem of a vehicle moving

in a finite tube is solved. Strom (15, 16) uses a compressible, unsteady one-dimensional model to describe the flow in the far-field in a tube of finite length.

In the present work, a more detailed and realistic formulation of the problem is presented. This includes investigating the problem during and after the boundary layer growth period. The effect of vents is studied. The problem of a train entering a tunnel at finite speed is investigated.

II. THE PROBLEM OF A VEHICLE ACCELERATING FROM REST IN AN UNVENTED TUBE

A. Formulation of the Problem

A vehicle accelerating in a tunnel from rest, causes compression and expansion waves to propagate in the tube ahead and behind the vehicle respectively. The waves accelerate the tube air. The air flow at a particular cross section may be considered one-dimensional and inviscid immediately after the arrival of the initial wave at that position. However, the non-slip condition at the tunnel wall causes a boundary layer to develop. At a specific position, its thickness increases with time until it completely fills the tunnel cross section (see Appendix B for a rough estimate for the boundary layer growth). The waves propagating from the vehicle, eventually reach the tunnel ends where they are reflected towards the vehicle.

To investigate the problem at hand, the flow field is divided into a near-field and a far-field. The near-field includes the annular region between the vehicle and the tunnel, the nose region which extends a few vehicle diameters ahead of the vehicle (see Appendix A), and the base region which is also assumed to extend a few diameters behind the vehicle (see Figs. 1, 3). The far-field consists of the rest of the flow region in the tube.

1. The Far-Field

To describe the flow in the far-field during and after the period of boundary layer growth, two sets of equations are required.

a. Boundary Layer Growth Period

Figure (2) represents the flow during the boundary layer growth

period. It indicates the notation used for describing the inviscid core and the boundary layer.

As the flow in the tube is almost parallel, $u^* >> v^*$, the pressure variations in the r^* direction are negligible compared to those in the x^* direction (the change of $p^*/\rho^*\hat{U}^{*2}$ across the boundary layer is of order $(\delta^*/L^*)^2$). Therefore the pressure is assumed constant at each cross section. The flow Mach numbers involved are small enough ($M \sim 0.05$) to make the density variation in the r^* direction negligible ($\Delta T/T$ across the tunnel is of order M^2). Therefore, the density is assumed constant for each cross section. A similarity profile is assumed for the boundary layer velocity distribution.

$$\frac{u^*(x^*, r^*, t^*)}{\hat{U}^*(x^*, t^*)} = f(\eta), \qquad \eta = \frac{y^*}{\delta^*}$$

We now define

$$I_1 \equiv \int_0^1 f(\eta)d\eta$$

$$I_2 \equiv \int_0^1 f(\eta)\eta d\eta$$

$$I_3 \equiv \int_0^1 f^2(\eta)d\eta$$

$$I_4 \equiv \int_0^1 f^2(\eta)\eta d\eta$$

In our analyses the flow in the tunnel is assumed to be axisymmetric. The continuity and x-momentum equations are respectively

$$\frac{\partial}{\partial t^*}(\rho^* r^*) + \frac{\partial}{\partial r^*}(\rho^* r^* v^*) + \frac{\partial}{\partial x^*}(\rho^* r^* u^*) = 0 \tag{1}$$

$$\frac{\partial}{\partial t^*}(\rho^* r^* u^*) + \frac{\partial}{\partial r^*}(\rho^* r^* u^* v^*) + \frac{\partial}{\partial x^*}(\rho^* r^* u^{*2})$$
$$= -\frac{\partial}{\partial x^*}(r^* p^*) + \frac{\partial}{\partial r^*}(r^* \tau^*) \tag{2}$$

We introduce the following dimensionless quantities:

$$x = \frac{x^*}{L^*}, \qquad r = \frac{r^*}{W^*}, \qquad t = \frac{a_o^* t^*}{L^*}$$

$$u = \frac{u^*}{V_o^*}, \qquad v = \frac{v^*}{\kappa V_o^*}, \qquad V = \frac{V^*}{V_o^*}$$

$$a = \frac{a^*}{a_o^*}, \qquad \rho = \frac{\rho^*}{\rho_o^*}, \qquad p = \frac{p^*}{p_o^*}$$

$$M_o = \frac{V_o^*}{a_o^*}, \qquad \kappa = \frac{W^*}{L^*}, \qquad \tau = \frac{\tau^*}{\rho_o^* V_o^{*2}}$$

where

L^* is the tube length

W^* is the tube radius

V_o^* is the maximum vehicle velocity

a_o^*, ρ_o^*, p_o^* are the values of sound speed, air density and pressure in the initial undisturbed state. Equations (1), (2) rewritten in dimensionless form are

$$\frac{\partial}{\partial t}(\rho r) + M_o \frac{\partial}{\partial r}(\rho r v) + M_o \frac{\partial}{\partial x}(\rho u r) = 0 \tag{3}$$

$$\frac{\partial}{\partial t}(\rho r u) + M_o \frac{\partial}{\partial r}(\rho r u v) + M_o \frac{\partial}{\partial x}(\rho r u^2)$$

$$= -\frac{1}{\gamma M_o}\frac{\partial}{\partial x}(rp) + \frac{M_o}{\kappa}\frac{\partial}{\partial r}(r\tau) \tag{4}$$

The flow is assumed to be inviscid uniform flow with $u = \hat{U}(x,t)$ for $0 \le r \le R(x,t) = 1 - \delta(x,t)$. The momentum equation becomes

$$\rho \hat{U}_t + M_o \rho \hat{U} \hat{U}_x + \frac{1}{\gamma M_o} p_x = 0 \tag{5}$$

Here $(\ )_t \equiv \frac{\partial}{\partial t}$, $(\ )_x \equiv \frac{\partial}{\partial x}$

In addition the core-flow is assumed to be isentropic (no shock waves or very weak shock waves, if they exist, are assumed). Hence the density and pressure variations are related by

$$d\rho = \frac{\rho}{\gamma p} \, dp \tag{6}$$

The effect of the boundary layer on the core flow is through the continuity equation, which yields after integration across the tube:

$$\rho_t + M_o(1 - \beta_1)\rho \hat{U}_x + M_o(1-\beta_1)\hat{U} \rho_x$$

$$- M_o \beta_1' \rho \hat{U} \delta_x = 0 \tag{7}$$

where

$$\beta_1 \equiv 2(1-I_1)\delta - (1-2 I_2)\delta^2$$

$$\beta_1' \equiv \frac{d\beta_1}{d\delta} = 2(1-I_1) - 2(1-2 I_2)\delta$$

The equation for the boundary-layer growth is obtained by integrating the momentum equation with respect to r from R to 1:

$$\beta_1(\hat{U} \rho_t + \rho \hat{U}_t) + \beta_1' \rho \hat{U} \delta_t + 2 M_o \beta_2 \hat{U}^2 \rho_x$$

$$+ M_o(\beta_1 + 4 \beta_2)\rho \hat{U} \hat{U}_x + 2 M_o \beta_2' \rho \hat{U}^2 \delta_x$$

$$= - \frac{2 M_o}{\kappa} \tau_o \tag{8}$$

where

$$\beta_2 \equiv (I_1 - I_3)\delta - (I_2 - I_4)\delta^2$$

$$\beta_2' \equiv \frac{d\beta_2}{d\delta} = (I_1 - I_3) - 2(I_2 - I_4)\delta$$

By introducing the isentropic relation (6) into Eqs. (5), (7) and (8) we obtain

$$(1-\beta_1)U_t + \beta_1' U \delta_t + M_o U U_x + \frac{(1-\beta_1)^2}{\gamma M_o p^{1/\gamma}} p_x + \frac{M_o \beta_1' U^2}{(1-\beta_1)} \delta_x = 0 \tag{9}$$

$$p_t + \gamma M_o p U_x + M_o U p_x = 0 \tag{10}$$

$$\beta_1(1-\beta_1)U_t + \frac{\beta_1(1-\beta_1)}{\gamma} \frac{U}{p} p_t + \beta_1' U \delta_t + M_o(\beta_1+4\beta_2)U U_x + 2\frac{M_o\beta_2}{\gamma} \frac{U^2}{p} p_x + \frac{M_o}{1-\beta_1} U^2 \delta_x [\beta_1'(\beta_1+4\beta_2) + 2\beta_2'(1-\beta_2)] = -\frac{2M_o \tau_o}{\kappa p^{1/\gamma}} (1-\beta_1)^2 \tag{11}$$

Here $U(x, t)$ is the average velocity at a cross section. It is related to the core velocity $\hat{U}(x, t)$ by

$$\hat{U} = \frac{U}{1-\beta_1}$$

Equations (9) - (11) are three equations in the three unknowns U, p, δ. Proper combinations of the three equations may be taken, and lead to the following system of equations:

$$U_t + M_o \frac{(1 - 4\beta_2 - \beta_1^2)}{(1 - \beta_1)^2} U U_x$$

$$+ \left[\frac{1}{\gamma M_o p^{1/\gamma}} - \frac{M_o U^2}{\gamma p} \frac{(2\beta_2 - \beta_1 + \beta_1^2)}{(1-\beta_1)^2} \right] p_x$$

$$+ \frac{M_o}{(1-\beta_1)^2} \left\{ \beta_1' - \frac{1}{1-\beta_1} [4\beta_1' \beta_2 + 2\beta_2'(1-\beta_2)] \right\} U^2 \delta_x$$

$$= \frac{2 M_o \tau_o}{\kappa p^{1/\gamma}} \tag{12}$$

$$p_t + \gamma M_o p U_x + M_o U p_x = 0 \tag{13}$$

$$\delta_t + M_o \frac{(\beta_1^2 - \beta_1 + 4\beta_2)}{\beta_1'(1-\beta_1)} U_x$$

$$+ \frac{1}{\beta_1'(1-\beta_1)U} \left\{ \frac{M_o U^2 (2\beta_2 - \beta_1 + \beta_1^2)}{\gamma p} - \frac{\beta_1 (1-\beta_1)^2}{\gamma M_o p^{1/\gamma}} \right\} p_x$$

$$+ \frac{M_o U}{\beta_1'(1-\beta_1)^2} [4\beta_1' \beta_2 + 2\beta_2'(1-\beta_2)] \delta_x$$

$$= - \frac{2 M_o \tau_o (1 - \beta_1)}{\kappa p^{1/\gamma} U \beta_1'} \tag{14}$$

This system is of the form

$$\underset{\sim}{w}_t^{(a)} + C^{(a)} \underset{\sim}{w}_x^{(a)} = \underset{\sim}{f}^{(a)} \tag{15a}$$

or

$$\underset{\sim}{w}_t^{(a)} = A^{(a)} \underset{\sim}{w}_x^{(a)} + \underset{\sim}{f}^{(a)} \tag{15b}$$

where

$$\underset{\sim}{w}^{(a)} = \begin{bmatrix} U \\ p \\ \delta \end{bmatrix}$$

$$\underset{\sim}{f}^{(a)} = \begin{bmatrix} \dfrac{2 M_o \tau_o}{\kappa p^{1/\gamma}} \\ 0 \\ -\dfrac{2 M_o \tau_o (1-\beta_1)}{\kappa \beta_1' U p^{1/\gamma}} \end{bmatrix}$$

$C^{(a)}$ is the matrix whose elements are the coefficients of the components of $\underset{\sim}{w}_x^{(a)}$ in equations (12)-(14), and

$$A^{(a)} = - C^{(a)}$$

Boundary and initial conditions are required to solve the above equations. The initial conditions are those of the undisturbed state

$$U(x, 0) = 0 \tag{16a}$$

$$p(x, 0) = 1 \tag{16b}$$

$$\delta(x, 0) = 0 \tag{16c}$$

At the tube exit the condition of constant pressure is satisfied

$$p(L, t) = 1 \tag{17a}$$

At the tube entrance the condition of zero boundary layer thickness and the adiabatic energy equation are satisfied

$$\delta(0, t) = 0 \tag{17b}$$

$$\frac{p(0, t)}{\rho(0, t)} + \frac{\gamma-1}{2} M_o^2 U(0, t)^2 = 1 \tag{17c}$$

where $\rho(0, t) = p(0, t)^{1/\gamma}$ (isentropic relation)

b. Fully Developed Flow Period:

The boundary layer continues its growth and it eventually fills the tube cross section (provided the cross section considered is far enough from the rear tube end). When this happens, a new set of equations is used to describe the flow. Besides continuity and momentum, the equation of energy is also considered. If we neglect the v^* velocity, the governing equations are:

continuity:

$$\frac{\partial}{\partial t^*}(r^*\rho^*) + \frac{\partial}{\partial x^*}(r^*\rho^*u^*) = 0 \tag{18}$$

x-momentum:

$$\frac{\partial}{\partial t^*}(r^*\rho^*u^*) + \frac{\partial}{\partial x^*}(r^*\rho^*u^{*2}) = -\frac{\partial}{\partial x^*}(r^*p^*) + \frac{\partial}{\partial r^*}(r^*\tau^*) \tag{19}$$

energy:

$$\frac{\partial}{\partial t^*}\left[r^*\rho^*\left(h^* + \frac{u^{*2}}{2}\right)\right] + \frac{\partial}{\partial x^*}\left[r^*\rho^*u^*\left(h^* + \frac{u^{*2}}{2}\right)\right] = -\frac{\partial}{\partial r^*}(r^*q^*) + \frac{\partial}{\partial r^*}(r^*u^*\tau^*) + \frac{\partial}{\partial t^*}(r^*p^*) \tag{20}$$

equation of state:

$$p^* = \rho^*R^*T \tag{21}$$

Eliminating T from the energy equation and writing the equations in dimensionless form, they become

$$\frac{\partial}{\partial t}(r\rho) + M_o \frac{\partial}{\partial x}(r\,\rho\,u) = 0 \tag{22}$$

$$\frac{\partial}{\partial t}(r\rho u) + M_o \frac{\partial}{\partial x}(r\,\rho\,u^2) = -\frac{1}{\gamma M_o}\frac{\partial}{\partial x}(r\,p) + \frac{M_o}{\kappa}\frac{\partial}{\partial r}(r\,\tau) \tag{23}$$

$$\frac{\partial}{\partial t}\left[r\rho\left(\frac{1}{\gamma-1}\frac{p}{\rho} + M_o^2\frac{u^2}{2}\right)\right] + M_o\frac{\partial}{\partial x}\left[r\,\rho\,u\left(\frac{1}{\gamma-1}\frac{p}{\rho} + M_o^2\frac{u^2}{2}\right)\right] = -\frac{M_o^3}{\kappa}\frac{\partial}{\partial r}(r\,q) + \frac{M_o^3}{\kappa}\frac{\partial}{\partial r}(r\,u\,\tau) + \frac{1}{\gamma}\frac{\partial}{\partial t}(r\,p) \tag{24}$$

where $q = q^* / \rho_o^*\, V_o^{*3}$

Let $\hat{U}(x,t)$ be the velocity at the tube centerline, and let

$$\frac{u(x,r,t)}{\hat{U}(x,t)} = g(r)$$

Define

$$E_1 \equiv \int_0^1 r\,g(r)dr$$

$$E_2 \equiv \int_0^1 r\,g^2(r)dr$$

$$E_3 \equiv \int_0^1 r\,g^3(r)dr$$

Assuming the pressure and density do not vary with r at a specific cross section, and integrating equations (22)-(24) across the tube, we get

$$\rho_t + 2 M_o E_1 \hat{U} \rho_x + 2 M_o E_1 \rho \hat{U}_x = 0 \tag{25}$$

$$E_1 \rho \hat{U}_t + E_1 \hat{U} \rho_t + 2 M_o E_2 \rho \hat{U} \hat{U}_x + M_o E_2 \hat{U}^2 \rho_x + \frac{1}{2\gamma M_o} p_x = \frac{M_o}{\kappa} \tau_o \tag{26}$$

$$\frac{1}{\gamma(\gamma-1)M_o} p_t + M_o E_2 \hat{U}^2 \rho_t + 2 M_o E_2 \rho \hat{U} \hat{U}_t + \frac{2}{\gamma-1} E_1 \hat{U} p_x + [\frac{2}{\gamma-1} E_1 p + 3 M_o^2 E_3 \rho \hat{U}^2] \hat{U}_x + M_o^2 E_3 \hat{U}^3 \rho_x = - \frac{2M_o^2}{\kappa} q_o \tag{27}$$

Introducing the average velocity

$$U(x,t) = 2 E_1 \hat{U}(x,t)$$

and taking proper combinations of equations (25)-(27) we arrive at the following set of equations

$$U_t + M_o(2 J_2 - 1) U U_x + \frac{1}{\gamma M_o \rho} p_x + M_o (J_2 - 1) \frac{U^2}{\rho} \rho_x = \frac{2M_o \tau_o}{\kappa \rho} \tag{28}$$

$$p_t + [\gamma M_o p + \frac{\gamma(\gamma-1)}{2} M_o^3 \rho U^2 (3 J_3 + J_2 - 4 J_2^2)] U_x + M_o(\gamma - \gamma J_2 + J_2) U p_x + \gamma \frac{(\gamma-1)}{2} M_o^3 (J_3 + J_2 - 2 J_2^2) U^3 \rho_x = \frac{-2 \gamma(\gamma-1) M_o^3}{\kappa} (q_o + J_2 \tau_o U) \tag{29}$$

$$\rho_t + M_o \rho U_x + M_o U \rho_x = 0 \tag{30}$$

where

$$J_2 \equiv \frac{2E_2}{(2E_1)^2}$$

$$J_3 \equiv \frac{2E_3}{(2E_1)^3}$$

The above equations constitute a system of the form

$$\underset{\sim}{w}_t^{(b)} + C^{(b)} \underset{\sim}{w}_x^{(b)} = \underset{\sim}{f}^{(b)} \tag{31a}$$

or

$$\underset{\sim}{w}_t^{(b)} = A^{(b)} \underset{\sim}{w}_x^{(b)} + \underset{\sim}{f}^{(b)} \tag{31b}$$

where

$$\underset{\sim}{w}^{(b)} = \begin{bmatrix} U \\ p \\ \rho \end{bmatrix}$$

$$\underset{\sim}{f}^{(b)} = \begin{bmatrix} \dfrac{2 M_o \tau_o}{\kappa \rho} \\ \dfrac{-2\gamma(\gamma-1) M_o^3}{\kappa} (q_o + J_2 \tau_o U) \\ 0 \end{bmatrix}$$

$C^{(b)}$ is the matrix whose elements are the coefficients of the components of $\underset{\sim}{w}_x^{(b)}$ in equations (28)-(30), and

$$A^{(b)} = - C^{(b)}$$

The above equations never apply to the flow at the tube entrance ($\delta = 0$ at $x = 0$). We therefore need only to consider the tube exit. There the condition of constant pressure is satisfied

$$p(L, t) = 1 \tag{32}$$

2. The Near-Field

The near-field flow (see Figs. 1, 3) which surrounds the vehicle is of a very complex nature. In this region boundary layers extend from both the vehicle and the tunnel surfaces. A detailed theoretical analysis of the boundary layers in the annular region and the wake behind the vehicle is a complex task. Experimental investigations dealing with the tube-vehicle problem are mainly interested in estimating the drag experienced by bodies moving in tubes. This is done by measuring the body's velocity profile (in case of a body propelled by its own weight) or by other methods which do not involve a detailed study of the flow in the near-field. With no data available for the flow in this region, we make simplified but reasonable assumptions to model the flow there. The three sub-regions composing the near-field are discussed below.

a. The Nose Region

The nose region flow is that occurring between stations (1) and (2) in Fig. (3). Noting that this region extends for a small distance in the X-direction (see Appendix A) over which the velocity is a rapidly changing function of X, it is clear that the changes in flow variables with respect to time are negligible in comparison to corresponding changes with respect to the space coordinates, provided that no abrupt changes (e.g. impulsive motion) occur. In vehicle fixed coordinates, the pressure gradient on the nose surface is negative in the flow direction, indicating that no separation occurs. Also the friction effect over such a short distance is negligible. In light of the above arguments, it is reasonable to use a frictionless, compressible, quasi-steady

formulation (in vehicle fixed coordinates) to describe the flow in the nose region. We therefore relate the flow at stations (1) and (2) by the equations of continuity, the adiabatic energy equation and the isentropic relation. They are respectively

$$(V-U_1)\rho_1 = (V-U_2)\rho_2\,(1-\sigma) \tag{33a}$$

$$\frac{\gamma-1}{2} M_o^2 (V-U_1)^2 + \frac{p_1}{\rho_1} = \frac{\gamma-1}{2} M_o^2 (V-U_2)^2 + \frac{p_2}{\rho_2} \tag{33b}$$

$$p_1 \rho_1^{\gamma} = p_2 \rho_2^{\gamma} \tag{33c}$$

where $V \equiv V(t)$

$u_i \equiv u(x_i(t),\ t)$

$\rho_i \equiv \rho(x_i(t),\ t)$

$p_i \equiv p(x_i(t),\ t)$

$$\sigma = \frac{\text{vehicle cross sectional area}}{\text{tube cross sectional area}}$$

b. The Annular Region

This region extends between stations (2) and (3) as seen in Fig. (3). Although the flow here is of a complex nature, simplifications may be introduced when noting the following. In this region the annular gap between the vehicle and the tube is small compared to the tube diameter. The flow speed relative to the vehicle surface is in general larger than the flow speed in the far-field. The above factors, in addition to the fact that boundary layers extend from both the vehicle and tube surfaces, indicate that the time required for the effect of viscosity to be felt across the annular gap is small with respect to

the corresponding time in the case of far-field flow. We therefore do not consider an inviscid region (corresponding to the far-field inviscid core) in the annular region. Moreover, the flow in this region is represented by a one dimensional compressible model with friction, governed by the following equations of mass, momentum and energy.

$$\frac{\partial \rho}{\partial t} + M_o \frac{\partial}{\partial x}(\rho U) = 0 \tag{34}$$

$$\frac{\partial}{\partial t}(\rho U) + M_o \frac{\partial}{\partial x}(\rho U^2) + \frac{1}{\gamma M_o}\frac{\partial p}{\partial x} = R_{AM} \tag{35}$$

$$\frac{\partial}{\partial t}\left[\rho\left(\frac{1}{\gamma-1}\frac{p}{\rho} + M_o^2\frac{U^2}{2}\right)\right] + M_o\frac{\partial}{\partial x}\left[\rho U\left(\frac{1}{\gamma-1}\frac{p}{\rho} + M_o^2\frac{U^2}{2}\right)\right] - \frac{1}{\gamma}\frac{\partial p}{\partial t} = R_{AE} \tag{36}$$

where

$$R_{AM} \equiv -\frac{M_o f_{TA}\rho U|U|}{\kappa(1-\sigma)} + \frac{M_o}{\kappa} f_{vh}\frac{\sqrt{\sigma}}{1-\sigma}\rho(V-U)|V-U|$$

$$R_{AE} \equiv \frac{2M_o^3}{\kappa}\frac{1}{1-\sigma}(Q_{TA} + \sqrt{\sigma}\, Q_{vh}) + \frac{M_o^3}{\kappa} f_{vh}\frac{\sqrt{\sigma}}{1-\sigma}\rho(V-U)|V-U|V$$

Here f_{vh} and f_{TA} are the vehicle and tube friction factors in the annular region.

Proper combinations of equations (34)-(36) lead to a system of the form

$$\underset{\sim}{w}_t^{(c)} + C^{(c)}\,\underset{\sim}{w}_x^{(c)} = \underset{\sim}{f}^{(c)} \tag{37a}$$

or

$$\underset{\sim}{w}_t^{(c)} = A^{(c)}\,\underset{\sim}{w}_x^{(c)} + \underset{\sim}{f}^{(c)} \tag{37b}$$

where

$$\underset{\sim}{w}^{(c)} = \begin{bmatrix} U \\ p \\ \rho \end{bmatrix}$$

$$\underset{\sim}{f}^{(c)} = \begin{bmatrix} f_1^{(c)} \\ f_2^{(c)} \\ f_3^{(c)} \end{bmatrix} = \begin{bmatrix} R_{AM}/\rho \\ \gamma(\gamma-1)(R_{AE} - M_o^2 R_{AM} U) \\ 0 \end{bmatrix}$$

$$A^{(c)} \equiv -C^{(c)}$$

and

$$C^{(c)} = \begin{bmatrix} M_o U & \frac{1}{\gamma M_o \rho} & 0 \\ \gamma M_o p & M_o U & 0 \\ M_o \rho & 0 & M_o U \end{bmatrix}$$

Using the transformation

$$X = x - \int_0^t M_o \, V(t')dt'$$

$$T = t$$

equations (34)-(36) are rewritten in vehicle fixed coordinates.

$$\frac{\partial \rho}{\partial T} + M_o \frac{\partial}{\partial X} (\rho U_v) = 0 \tag{38}$$

$$\frac{\partial}{\partial T} (\rho U_v) + \rho \frac{\partial V}{\partial T} + M_o \frac{\partial}{\partial X} (\rho U_v^2) + \frac{1}{\gamma M_o} \frac{\partial p}{\partial X} = R_{AM} \tag{39}$$

$$\frac{\partial}{\partial T} \left(\frac{1}{\gamma(\gamma-1)} p + \frac{M_o^2}{2} \rho U_v^2 \right) + M_o^2 \rho U_v \frac{\partial V}{\partial T}$$

$$+ \frac{\partial}{\partial X} \left(\frac{M_o}{\gamma - 1} p U_v + \frac{M_o^3}{2} \rho U_v^3 \right) = R_{AE} - M_o^2 V R_{AM} \tag{40}$$

where $U_v = U-V$

is the flow velocity in vehicle fixed coordinates.

In previous studies the flow in the annular region was assumed to be quasi-steady in vehicle fixed coordinates. Such an assumption neglects the time derivatives in equations (38)-(40), reducing them to steady state equations in vehicle fixed coordinates.

$$\frac{d}{dX}(\rho U_v) = 0 \tag{41}$$

$$\frac{d}{dX}\left(M_o \rho U_v^2 + \frac{p}{\gamma M_o}\right) = R_{AM} \tag{42}$$

$$\frac{d}{dX}\left(\frac{M_o}{\gamma-1} p U_v + \frac{M_o^3}{2} \rho U_v^3\right) = R_{AE} - M_o^2 V R_{AM} \tag{43}$$

The argument given to justify the quasi-steady assumption for situations in which the vehicle length, $L_{vh} \ll L$, the tube length, is that the time required for the near-field to adjust to steady state after a pressure perturbation is much shorter than that required by the far-field. However, this argument is not a convincing one.

As will be explained later, the solution to our problem is obtained numerically. The far-field is divided into a net with spacings Δt and Δx in the t and x directions respectively (Δt is less than Δx but of the same order). Let us now consider two cases of vehicles accelerating in tubes. In the first, (case (a)) (Fig. (4b)) the vehicle length $L_{vh\,a} \ll \Delta x$ and $L_{vh\,a} \ll L$. In the second, (case (b)) (Fig. (4b)) the vehicle length $L_{vh\,b} \sim \Delta x$ and $L_{vh\,b} \ll L$. At the time interval $t_{n-1} < t < t_n$ the vehicles are assumed to be travelling with constant velocity V_{n-1}. At time t_n a velocity increment ΔV_n is assumed, so that the vehicles move with a velocity

$$V_n = V_{n-1} + \Delta V_n$$

in the time interval $t_n < t < t_{n+1}$. The velocity increment ΔV_n causes pressure waves to propagate through both the far- and near-fields. In case (a), at time t_{n+1} many pressure waves will have passed through the annular region, and the disturbance will have been weakened considerably. It is therefore reasonable to make the quasi-steady assumption. However, in case (b) at time t_{n+1} the pressure wave will have travelled approximately one length L_{vhb} through the annular region. In this case it is not justifiable to make the quasi-steady near-field assumption. A rough estimate to compare the unsteady terms (first two terms in eq. 39) to the frictional terms (right hand side of eq. 39) in eq. (39) may be obtained by integrating the equation over the vehicle's length. The rate of the variation of ρ is small with respect to the rate of velocity variations. We therefore neglect variations in density. This leads to the following expression for the ratio of the force required to accelerate the air in the annular region to the force required to overcome the wall friction.

$$\frac{\text{unsteady forces}}{\text{frictional forces}} = \frac{\dfrac{\partial U_v}{\partial T}}{\dfrac{M_o f}{\kappa(1-\sigma)}\left[-U|U| + \sqrt{\sigma}\,(V-U)|V-U|\right]}$$

Here f_{TA} and f_{vh} are assumed to be equal, and

$$f \equiv f_{TA} = f_{vh}$$

The above ratio may be rewritten as

$$\frac{\text{unsteady forces}}{\text{frictional forces}} = \frac{W^*}{V_o^{*2}} \frac{(1-\sigma)}{f} \frac{\partial U_v^*}{\partial T^*} \frac{1}{\left[-U|U| + \sqrt{\sigma}\,(V-U)|V-U|\right]}$$

from which we may conclude that an increase in the values of f and V_o^* lead to an increase in the frictional terms, while an increase in the vehicle's acceleration causes an increase in the unsteady terms. For V_o^* = 100 ft./sec., f = 0.02, σ = 0.65 and a vehicle acceleration of 5 ft/sec^2 the above ratio $\sim$ 0.1.

c. The Base Region

Although experiments investigating the flow in this region have not been conducted, we rely on the results of experiments having some aspects in common with this flow to construct a simplified model.

In vehicle fixed coordinates (Fig. 3) the flow goes through a sudden enlargement in cross sectional area at station (3). Unsteady flows in pipes with cross sectional area changes were investigated by Benson and his co-workers (Reference (17)). Though their geometrical configuration is different from that under consideration, their results are of interest.

Their experiments were conducted on flows in pipes of small diameters ($\sim$ 2"). They found that quasi-steady conditions may be assumed at the regions of sudden area change. In steady flow it was found that the location of the pressure recovery plane increases with the upstream pressure and velocity. For tube area ratios of 0.25 and 0.56 the recovery planes were

respectively in the neighborhood of 5 diameters and 3 diameters downstream of the enlargement area. This distance in the unsteady case was found to be 35 to 50 percent of the corresponding steady state case. Although the flow close to the enlargement area is three-dimensional and the one-dimensional equations do not accurately predict the pressure there, this region is not long (few tube diameters). Comparing their experimental results with theoretical results based on one-dimensional flow, Benson and his co-authors concluded that the region of three-dimensional flow (downstream of the enlargement) may be neglected when calculating the overall wave action, and for these calculations the plane of recovery may be fixed in the plane of the enlargement.

Other experiments of interest deal with the flow near the base for bodies of revolution in free air (References (18)-(21)). Measurements indicate that the pressure on the base of a body in free air is approximately constant. It is proportional to the dynamic pressure of the outside flow, and it depends on the body length, shape, and its surface conditions. Measurements of base pressure for different bodies indicate that the value of the base pressure coefficient (defined as the difference between base and ambient pressure divided by the dynamic pressure) is in the neighborhood of -0.2. In reference (20) Chevray studied the wake behind a six-to-one spheroid for Reynolds number equal to 2.75×10^6. His measurements indicate that beyond a distance

of 2D (where D is the maximum body diameter) downstream of the body the pressure varies negligibly with r. At 18D downstream of the body, the maximum velocity deficit in the wake was about 10 percent.

Though the above experimental results do not apply to the problem under consideration, enough similarities between the flows involved in the two cases lead us to rely on the above results for some of the assumptions we make for the base region under consideration. We define a base pressure coefficient

$$C_{pB} \equiv \frac{p_B - p_3}{\frac{1}{2}\rho(V-U_3)^2}$$

We assume that the flow is quasi-steady between stations (3) and (4) in vehicle fixed coordinates (see Fig. (3)). Moreover we assume that the length of the base region is small compared to the tube length. The flows at stations (3) and (4) are related through the equations of continuity, momentum and adiabatic energy. They are respectively

$$(1-\sigma)\rho_3 (V-U_3) = \rho_4(V-U_4) \tag{44}$$

$$\frac{p_4-p_3}{\gamma M_o^2} = \rho_3(V-U_3)^2 \left[1 + \sigma\left(\frac{C_{pB}}{2} - 1\right)\right] - \rho_4(V-U_4)^2 \tag{45}$$

$$\frac{\gamma-1}{2} M_o^2 (V-U_3)^2 + \frac{p_3}{\rho_3} = \frac{\gamma-1}{2} M_o^2 (V-U_4)^2 + \frac{p_4}{\rho_4} \tag{46}$$

d. Vehicle Drag

The aerodynamic resistance experienced by a vehicle travelling in a tube includes the skin friction drag which basically results

from the frictional forces between the fluid and the vehicle surface in the annular region. The pressure drag is the result of pressure forces on the vehicle (nose and base).

The average flow velocity U in the annular region is generally negative. Therefore the relative velocity between the flow and the vehicle surface is larger than its corresponding value for an unconfined vehicle. Consequently, the skin friction drag is generally greater for a vehicle when travelling in a tube than when travelling in free air. Moreover, we note that in the case of vehicles travelling in tubes, the frictional forces acting on the fluid in the annular region contribute to the pressure drag, as the pressure in this region causes a corresponding drop in the base pressure, and therefore a higher pressure drag.

3. The Contact Surface

Part of the flow passes through the near-field before it enters the far-field behind the vehicle (the fluid between the vehicle and the contact surface in Fig. 1). When in the near-field, friction acts on the flow. Therefore, after it becomes part of the far-field, the isentropic relations initially assumed to relate the pressure and density there do not apply. Moreover the flow passing through the wake becomes mixed and may no longer be described by the inviscid core model. The flow in the wake region is complex. However, representing it by the fully developed model is a better approximation than the inviscid core model. We therefore assume that a dividing surface exists in the rear far-field (referred to as the contact surface). It divides the fluid which passed through the near-field from

the rest of the rear far-field. It is assumed to be travelling with the average flow velocity, with equal pressure and average flow velocity on both its sides, but a change in density. The governing relations at the contact surface are therefore given by

$$\frac{dx_{ct}}{dt} = U_{ct}$$

$$U_{ct\,\ell} = U_{ct\,r} = U_{ct}$$

$$p_{ct\,\ell} = p_{ct\,r}$$

Where $(\ )_{ct}$ denotes conditions at the contact surface and $(\ )_{ct\,\ell}$, $(\ )_{ct\,r}$ respectively denote flow conditions upstream and downstream of the contact surface.

4. The Unsteady Flow Equations

The far-field unsteady flow equations (15a, 31a) and the near-field unsteady flow equations (37a) are all of the form

$$\underset{\sim}{w}_t + C\,\underset{\sim}{w}_x = \underset{\sim}{f}$$

where

$$\underset{\sim}{w} \equiv \begin{cases} \underset{\sim}{w}^{(a)} & \text{(far-field boundary layer growth period)} \\ \underset{\sim}{w}^{(b)} & \text{(far-field fully developed flow)} \\ \underset{\sim}{w}^{(c)} & \text{(near-field annular region)} \end{cases}$$

Similar definitions apply to C and $\underset{\sim}{f}$. In each of the above three cases matrix C has three real distinct eigen values, indicating that the equations we are dealing with are of hyperbolic type and may be transformed to characteristic coordinates. The characteristic

directions at a point are obtained by finding the eigen values of the matrix C. Solving the equation

$$|C - \lambda I| = 0$$

or

$$\lambda^3 + \lambda^2 \kappa_1 + \lambda \kappa_2 + \kappa_3 = 0$$

where κ_1, κ_2, κ_3 are the corresponding coefficients for the former equation, we get

$$\lambda_I = 2\sqrt{-\frac{\alpha}{3}} \cos \frac{\theta}{3} - \frac{\kappa_1}{3}$$

$$\lambda_{II} = -\sqrt{-\frac{\alpha}{3}} \cos \frac{\theta}{3} + \sqrt{-\alpha} \sin \frac{\theta}{3} - \frac{\kappa_1}{3}$$

$$\lambda_{III} = -\sqrt{-\frac{\alpha}{3}} \cos \frac{\theta}{3} - \sqrt{-\alpha} \sin \frac{\theta}{3} - \frac{\kappa_1}{3}$$

where

$$\theta = \tan^{-1} \left\{ \frac{\sqrt{-(\frac{\beta}{2})^2 - (\frac{\alpha}{3})^3}}{-\frac{\beta}{2}} \right\}$$

$$\alpha = \frac{1}{3} (3\kappa_2 - \kappa_1^2)$$

$$\beta = \frac{1}{27} (2\kappa_1^3 - 9\kappa_1\kappa_2 + 27\kappa_3)$$

λ_I, λ_{II}, λ_{III} respectively correspond to the right going, intermediate and left going characteristics. The corresponding eigen vectors are obtained by solving the equation

$$[C - \lambda_k]^T \underset{\sim}{\ell}_k = 0, \qquad k = I, II, III$$

where $[\ ]^T$ denotes the transpose of a matrix. The unsteady flow

equations may now be written in characteristic coordinates

$$\underset{\sim}{\ell}^{k}\,(\underset{\sim}{w})\cdot\left(\frac{d\underset{\sim}{w}}{dt}-\underset{\sim}{f}(\underset{\sim}{w})\right)=0 \qquad k = I,\ II,\ III \qquad (48a)$$

along the corresponding characteristic curves

$$\frac{dx}{dt}=\lambda_{k}(\underset{\sim}{w}) \qquad k = I,\ II,\ III \qquad (48b)$$

In the case of the one-dimensional unsteady equations used to describe the near-field flow in the annular region, simple expressions are obtained for the characteristic directions and for the flow equations along them. They are

$$\gamma M_{o}\sqrt{p\rho}\ \frac{dU}{dt}+\frac{dp}{dt}=\gamma M_{o}\sqrt{p\rho}\ f_{1}^{(c)}+f_{3}^{(c)}$$

along

$$\frac{dx}{dt}=\lambda_{I}=U M_{o}+\sqrt{\frac{p}{\rho}}$$

$$\frac{dp}{dt}-\frac{\gamma p}{\rho}\frac{d\rho}{dt}=f_{3}^{(c)}$$

along

$$\frac{dx}{dt}=\lambda_{II}=U M_{o}$$

$$-\gamma M_{o}\sqrt{p\rho}\ \frac{dU}{dt}+\frac{dp}{dt}=-\gamma M_{o}\sqrt{p\rho}\ f_{1}^{(c)}+f_{3}^{(c)}$$

along

$$\frac{dx}{dt}=\lambda_{III}=U M_{o}-\sqrt{\frac{p}{\rho}}$$

Similar expressions may be obtained for the far-field characteristic equations. However, the nonuniform velocity profile assumed there, leads to more complex equations. The same assumption

causes a slight change in the characteristic directions when compared to those of a uniform flow. If we assume the function $f(\eta)$ (previously used to define the velocity similarity profile) is of the form

$$f(\eta) = \eta^{\frac{1}{n}}$$

then for large n (n is of order 10 for flows under consideration) we find that

$$\lambda_I = M_o U + \sqrt{\frac{p}{\rho}} + O(\frac{1}{n^2})$$

$$\lambda_{II} = \begin{cases} M_o U [1 + O(\frac{1}{n})] & \text{(boundary layer growth period)} \\ M_o U[1 + O(\frac{1}{n^3})] & \text{(fully developed flow)} \end{cases}$$

$$\lambda_{III} = M_o U - \sqrt{\frac{p}{\rho}} + O(\frac{1}{n^2})$$

λ_I, λ_{III} correspond to the pressure waves travelling in the upstream and downstream directions, and λ_{II} corresponds to the fluid particle path.

B. Method of Solution

1. The Far-Field

The set of far-field equations we are dealing with is of the form

$$\underset{\sim}{w}_t = A \underset{\sim}{w}_x + \underset{\sim}{f} \tag{49}$$

and may be suitably solved using the Lax-Wendroff method which is of second order accuracy. The x-t diagram is divided into a net, with uniform spacings Δx, Δt in the x and t directions respectively. Solutions are obtained at the nodal points (x_j, t_{n+1}) (points marked x in Fig. 5) where

$$x_j = j \Delta x \qquad j \in \hat{J}_{n+1}$$

$$t_{n+1} = 2 \Delta x + n \Delta t \qquad n = 0, 1, \ldots, N.$$

The condition $j \in \hat{J}_{n+1}$ is satisfied only if the four nodal points (x_j, t_{n+1}), (x_{j-1}, t_n), (x_j, t_n) and (x_{j+1}, t_n) lie in the same far-field sub-region (forward far-field or rear far-field ahead of contact surface or rear far-field behind contact surface). $\underset{\sim}{w}(x_j, t_{n+1})$ which we denote by $\underset{\sim}{w}^{j, n+1}$ may be represented by Taylor's series in t, in terms of $w^{j, n}$ and its derivatives. Using this expansion (neglecting terms of order Δt^3) and the governing equation (49) leads to the

following representation of $\underset{\sim}{w}^{j,\,n+1}$ in terms of $\underset{\sim}{w}^{j,\,n}$ and its x-derivatives.

$$\underset{\sim}{w}^{j,\,n+1} = \underset{\sim}{w}^{j,\,n} + \Delta t\,[A\underset{\sim}{w}_x + \underset{\sim}{f}]^{j,\,n} + \frac{\Delta t^2}{2}\left\{A[A\underset{\sim}{w}_x + \underset{\sim}{f}]_x + A_t\,\underset{\sim}{w}_x + \underset{\sim}{f}_t\right\}^{j,\,n}$$

The vector $\underset{\sim}{f}_t$ and the m^{th} column of matrix A_t are evaluated by

$$\underset{\sim}{f}_t = \underset{\sim}{f}_{\underset{\sim}{w}}[A\underset{\sim}{w}_x + \underset{\sim}{f}]$$

$$(A_{*m})_t = (A_{*m})_{\underset{\sim}{w}}\,[A\underset{\sim}{w}_x + \underset{\sim}{f}]$$

where matrices $\underset{\sim}{f}_{\underset{\sim}{w}}$ and $(A_{*m})_{\underset{\sim}{w}}$ are respectively the Jacobians of $\underset{\sim}{f}$ and A_{*m} with respect to $\underset{\sim}{w}$. When performing numerical calculations, the x-derivatives are approximated by difference quotients. This gives

$$\underset{\sim}{w}^{j,\,n+1} = \underset{\sim}{v}_o + \Delta t\,\underset{\sim}{v}_1 + \frac{\Delta t^2}{2}\,\underset{\sim}{v}_2$$

where

$$\underset{\sim}{v}_o \equiv \underset{\sim}{w}^{j,\,n}$$

$$\underset{\sim}{v}_1 \equiv A^{j,\,n}\,\frac{\underset{\sim}{w}^{j+1,\,n} - \underset{\sim}{w}^{j-1,\,n}}{2\,\Delta x} + \underset{\sim}{f}^{j,\,n}$$

$$\underset{\sim}{v}_2 \equiv \underset{\sim}{v}_{21} + \underset{\sim}{v}_{22} + \underset{\sim}{v}_{23}$$

$$\underset{\sim}{v}_{21} \equiv A^{j,\,n}\left\{A^{j+\frac{1}{2},\,n}\,\frac{\underset{\sim}{w}^{j+1,\,n} - \underset{\sim}{w}^{j,\,n}}{\Delta x^2} - A^{j-\frac{1}{2},\,n}\,\frac{\underset{\sim}{w}^{j,\,n} - \underset{\sim}{w}^{j-1,\,n}}{\Delta x^2} + \frac{\underset{\sim}{f}^{j+\frac{1}{2},\,n} - \underset{\sim}{f}^{j-\frac{1}{2},\,n}}{\Delta x}\right\}$$

$$\underset{\sim}{v}_{22} \equiv A_t^{j,n} \frac{\underset{\sim}{w}^{j+1,n} - \underset{\sim}{w}^{j-1,n}}{2\Delta x}$$

$$\underset{\sim}{v}_{23} \equiv [\underset{\sim}{f}_{\underset{\sim}{w}}]^{j,n} \left\{ A^{j,n} \frac{\underset{\sim}{w}^{j+1,n} - \underset{\sim}{w}^{j-1,n}}{2\Delta x} + \underset{\sim}{f}^{j,n} \right\}$$

where the m^{th} column of matrix $A_t^{j,n}$ is given by

$$(A_{*m})_t^{j,n} = (A_{*m})_{\underset{\sim}{w}}^{j,n} \left[A^{j,n} \frac{\underset{\sim}{w}^{j+1,n} - \underset{\sim}{w}^{j-1,n}}{2\Delta x} + \underset{\sim}{f}^{j,n} \right]$$

$A^{j+\frac{1}{2},n}$ denotes $A(\frac{1}{2}\underset{\sim}{w}^{j,n} + \frac{1}{2}\underset{\sim}{w}^{j+1,n})$

$A^{j-\frac{1}{2},n}$ denotes $A(\frac{1}{2}\underset{\sim}{w}^{j-1,n} + \frac{1}{2}\underset{\sim}{w}^{j,n})$

etc.

In choosing the net spacings Δt and Δx, we are limited by the stability condition, which requires that $|\lambda| < \frac{\Delta x}{\Delta t}$ for each eigen value λ of A.

In Fig. (5) nodal points (x_j, t_{n+1}) marked □ fall close to the contact surface or to the near-field far-field interface. In such cases the information is not known at the appropriate nodal points in the previous time step. Therefore the solution is not obtainable through the use of the above finite difference method. The methods of characteristics are applied.

The Method of Characteristics:

The unsteady flow equations were written in characteristic form in equations (48). For the purpose of numerical calculations the equations are approximated by

$$\underset{\sim}{\ell}^k(\overline{\underset{\sim}{w}}) \cdot [\underset{\sim}{w}^{j,n+1} - \underset{\sim}{w}^k - (t_{n+1} - t_k)\underset{\sim}{f}(\overline{\underset{\sim}{w}})] = 0 \quad k = I, II, III \qquad (50a)$$

$$x_j - x_k = (t_{n+1} - t_k)\, \lambda_k(\bar{\underset{\sim}{w}}) \qquad k = I,\ II,\ III \tag{50b}$$

where

$$\bar{\underset{\sim}{w}} = \frac{\underset{\sim}{w}^{j,\,n+1} + \underset{\sim}{w}^{k}}{2}$$

and $\underset{\sim}{w}^{k}$ denotes the solution at the point (x_k, t_k) which is obtained by linear interpolation between points at which the solution is known (see Fig. 6a). Equations (50) reduce the problem of finding the solution $\underset{\sim}{w}^{j,\,n+1}$ at point (x_j, t_{n+1}) to solving a set of algebraic non-linear equations of the form

$$\underset{\sim}{G}(\underset{\sim}{W}) = 0$$

where

$$\underset{\sim}{W} \equiv \begin{bmatrix} \underset{\sim}{w}^{j,\,n+1} \\ x_I \\ x_{II} \\ x_{III} \end{bmatrix}$$

The above system is solved by iteration. Newton's method is used. A big advantage of this method is the fact that the convergence is of second order (i.e. the error in any iterate is proportional to the square of the previous error) provided the initial iterate $\underset{\sim}{W}^{(o)}$ is sufficiently close to the root $\underset{\sim}{W}$ of the equation

$$\underset{\sim}{G}(\underset{\sim}{W}) = 0$$

This method involves the calculation of the Jacobian $\underset{\sim}{G}_{\underset{\sim}{W}}$ of $\underset{\sim}{G}$ with respect to $\underset{\sim}{W}$, as the $\nu+1$ iterate is given by

$$\underset{\sim}{W}^{(\nu+1)} = \underset{\sim}{W}^{(\nu)} - [\underset{\sim}{G}_{\underset{\sim}{W}}(\underset{\sim}{W}^{(\nu)})]^{-1}\, \underset{\sim}{G}(\underset{\sim}{W}^{(\nu)})$$

We point out that the approximate equations (50a, 50b) are of second order accuracy. Therefore their use is consistent with using the Lax-Wendroff method which is of the same accuracy.

Solution at the Boundaries:

The solution at the nodal points falling on the boundaries x = 0 and x = L is obtainable by satisfying the boundary conditions in addition to the far-field characteristic equations (48), where k = III (see Fig. 6b) in the case of the boundary x = 0 and k = 2, 3 (see Fig. 6c) in the case of the boundary x = L. The characteristic equations are written in their approximate form (50). Combined with the appropriate boundary conditions a nonlinear system of algebraic equations is obtained

$$\underset{\sim}{G}(\underset{\sim}{W}) = 0$$

where

$$\underset{\sim}{W} \equiv \begin{bmatrix} \underset{\sim}{w}^{o,\,n+1} \\ x_{III} \end{bmatrix} \qquad \text{(at boundary } x = 0\text{)}$$

$$W \equiv \begin{bmatrix} \underset{\sim}{w}^{J,\,n+1} \\ x_{I} \\ x_{II} \end{bmatrix} \qquad \text{(at boundary } x = L\text{)}$$

and again each set is solved by iteration.

Solution at the Contact Surface:

To find the position of the contact surface and the flow variables on both its sides at time t_{n+1}, the conditions of pressure equality and the equality of average flow velocity on both its sides are satisfied.

In addition (see Fig. 6d) its position at time t_{n+1} is determined by

$$\frac{x_5(t_{n+1})-x_5(t_n)}{\Delta t} = \frac{U(x_5(t_{n+1}), t_{n+1}) + U(x_5(t_n), t_n)}{2}$$

and the far-field equations are satisfied along characteristics I^a, II^a behind it and II^b, III^b ahead of it. The above equations and conditions form a set of nonlinear algebraic equations. Solving them by iteration the position $x_5(t_{n+1})$ of the contact surface and the flow properties on both its sides at time t_{n+1} are determined.

Solution for Flow Caused by Initial Waves:

The two strips shown in Figs. (5) and (7) represent the flow at stations along the tube for a very short period after the arrival of the initial wave. In these regions $U \ll 1$. We let

$$a = 1 + M_o \bar{a}$$

where $\bar{a} \ll 1$. Then the governing equations for the first approximation are

$$\frac{2}{\gamma-1} \bar{a}_t + (1 + \beta_1)\hat{U}_x - \hat{U} \beta_1' \delta_x = 0$$

$$\hat{U}_t + \frac{2}{\gamma-1} \bar{a}_x = 0$$

$$\hat{U} \beta_1' \delta_t + \beta_1 \hat{U}_t = - \frac{2}{\kappa} M_o \tau_o$$

Recognizing that

$$\beta_1' \delta_x = \beta_{1_x} \qquad \text{and} \qquad \beta_1' \delta_t = \beta_{1_t}$$

We combine these equations to obtain

$$(U + \frac{2}{\gamma-1} \bar{a})_t + (U + \frac{2}{\gamma-1} \bar{a})_x = \frac{2}{\kappa} M_o \tau_o$$

$$\left(\frac{\beta_1}{1-\beta_1} U\right)_t = -\frac{2}{\kappa} M_o \tau_o$$

$$\left(U - \frac{2}{\gamma-1} \bar{a}\right)_t - \left(U - \frac{2}{\gamma-1} \bar{a}\right)_x = \frac{2}{\kappa} M_o \tau$$

or

$$\frac{d}{dt}\left(U + \frac{2}{\gamma-1} \bar{a}\right) = \frac{2}{\kappa} M_o \tau_o \quad \text{along} \quad \frac{dx}{dt} = 1 \tag{51}$$

$$\frac{d}{dt}\left(\frac{\beta_1}{1-\beta_1} U\right) = -\frac{2}{\kappa} M_o \tau_o \quad \text{along} \quad \frac{dx}{dt} = 0 \tag{52}$$

$$\frac{d}{dt}\left(U - \frac{2}{\gamma-1} \bar{a}\right) = \frac{2}{\kappa} M_o \tau_o \quad \text{along} \quad \frac{dx}{dt} = -1 \tag{53}$$

Consider points (a), (b) (Fig. 7) lying on a line $\frac{dx}{dt} = -1$ and points (b), (c) lying on a line $\frac{dx}{dt} = 1$. From equations (51) and (53) the solution at point (b) is approximated by

$$U_b = \frac{U_c}{2} + \frac{\bar{a}_c}{\gamma-1} + \frac{M_o}{\kappa}\left(\tau_{cb} \Delta t_{bc} + \tau_{ba} \Delta t_{ba}\right)$$

$$\bar{a}_b = \frac{\gamma-1}{4} U_c + \frac{\bar{a}_c}{2} + \frac{\gamma-1}{2} \frac{M_o}{\kappa}\left(\tau_{cb} \Delta t_{bc} - \tau_{ba} \Delta t_{ba}\right)$$

where

$$\tau_{ij} = \frac{\tau_i + \tau_j}{2}$$

$$\Delta t_{ij} = t_i - t_j$$

In the regions of initial waves, for typical values of our problem the last term in the above expressions for U_b and $\bar{a}_b$ is negligible with respect to the first two terms. Therefore the friction term is neglected when determining the flow properties. The one dimensional acoustic equations are used

$$\frac{d}{dt}\left(U + \frac{2}{\gamma-1}\,\bar{a}\right) = 0 \qquad \text{along } \frac{dx}{dt} = 1$$

$$\frac{d}{dt}\left(U - \frac{2}{\gamma-1}\,\bar{a}\right) = 0 \qquad \text{along } \frac{dx}{dt} = -1$$

Then the boundary layer thickness is determined using the equation

$$\left(\frac{\beta_1}{1-\beta_1}\,U\right)_t = -\frac{2}{\kappa}\,M_o\,\tau_o\,.$$

2. The Near-Field

The vehicle length is assumed to be of order Δx or less. Therefore to find the solution at points $(x_1(t_{n+1}),\ (x_2(t_{n+1}),\ t_{n+1})$, $(x_3(t_{n+1}), t_{n+1})$ and $(x_4(t_{n+1}), t_{n+1})$, the following equations are to be simultaneously satisfied. The nose equations (33), the base equations (44)-(46), the far-field equations along characteristics I^a, II^b, III^b (see Fig. 6e) and the near-field equations along characteristics (II^a, III^a, I^b). The characteristic equations are written in their approximate form (50) and again the problem is reduced to solving a set of nonlinear algebraic equations of the form

$$\underset{\sim}{G}(\underset{\sim}{W}) = 0$$

where $\underset{\sim}{W} =$

$$\begin{bmatrix} \underset{\sim}{w}(x_1(t_{n+1}), t_{n+1}) \\ \underset{\sim}{w}(x_2(t_{n+1}), t_{n+1}) \\ \underset{\sim}{w}(x_3(t_{n+1}), t_{n+1}) \\ \underset{\sim}{w}(x_4(t_{n+1}), t_{n+1}) \\ x_I^a \\ x_{II}^a \\ x_{III}^a \\ x_I^b \\ x_{II}^b \\ x_{III}^b \end{bmatrix}$$

This is done by iteration.

If the contact surface is close behind the vehicle, the near-field solution and the solution at the contact surface are found simultaneously (see Fig. 6f). For cases in which the near-field is treated as quasi-steady in vehicle fixed coordinates, the near-field unsteady equations are replaced by the steady equations (41)-(43), which are approximated by the use of finite quotients.

C. Numerical Calculations and Results

1. Choice of Parameter Values

A number of parameters are involved in the vehicle-tube problem. We discuss them below.

The Flow Velocity Profile:

Turbulent flows in rough pipes have a velocity profile which is less uniform than corresponding flows in smooth pipes. In reference (25) it is seen that the velocity distribution across a rough pipe is very well represented by a power formula, where the exponents are 1/4 or 1/5 at Reynolds number 10^6. Available experimental data for velocity profiles in tubes usually deal with incompressible steady flow. For our unsteady calculations we rely on such available data and study the effect of its variation on the solution of the problem. Therefore we assume that the flow similarity profile is represented by a power law.

$$\frac{u}{\hat{U}} = f(\eta) \equiv \eta^{\frac{1}{n}} \qquad \text{(Boundary layer growth period)}$$

$$\frac{u}{\hat{U}} = g(r) \equiv (1-r)^{\frac{1}{n}} \qquad \text{(Boundary layer fills tube cross section)}$$

Logarithmic profiles are often used to represent the velocity distribution across a tube cross section. However, the fact that it and the power profile are very close to each other and noting that the equations we are dealing with are obtained by integrating the flow equations across the tube, we expect that the effect of using a logarithmic profile instead of a power profile would be negligible.

Friction at the Tunnel Wall:

For turbulent flow in smooth pipes the friction factor

$$f = \frac{\tau_o}{\frac{1}{2} \rho U^2}$$

is a decreasing function of the Reynolds number. For rough pipes it is a function of the Reynolds number. However, at high Reynolds numbers (above 10^4) curves in reference (25) reveal that the variation becomes small. In our problem we are dealing with rough tunnels and as the flow Reynolds number is higher than 10^4 except for a negligible period, the tunnel friction factor is assumed to be constant for a specific example. The effect of its variation on the problem solution is studied in different examples. We may point here that the friction factor was found to be about 50% larger in unsteady flow in smooth pipes than its corresponding value for steady flow (Ref. 17).

Other Parameters:

In the examples below the vehicle is assumed to begin its motion from rest at x = 0.3. It is assumed to accelerate at a constant value of 5 ft/sec^2 until it reaches a final speed, after which it travels

at constant velocity. The parameter values given below are a representation of vehicle-tube systems and unless otherwise specified they are used in the calculations.

Tube length	= 10,000 ft
Vehicle length	= 300 ft
Vehicle radius	= 6 ft
Blockage ratio	= 0.65
Tube friction factor	= 0.02
Vehicle friction factor	= 0.02
Base pressure coefficient	= -0.15
Vehicle acceleration	= 5 ft/sec^2
Vehicle final speed	= 100 ft/sec
Initial vehical position	x = 0.3
n (for flow velocity profile)	= 6

Heat transfer through the tunnel wall is neglected (tunnel wall is assumed to be insulated).

2. Results

a. General Observations and Discussion

The travelling time of the vehicle in the tube is divided into three distinct periods. Period (A) is that in which the vehicle accelerates. During this period the vehicle must provide the force required to accelerate the far-field air column in addition to the force required to overcome the frictional forces experienced by the far-field air. These forces appear as a drag force acting on the vehicle. During this period a large pressure drop is observed along the near-field.

As the vehicle reaches its final velocity the aerodynamic forces acting on it are reduced, as the aerodynamic drag becomes essentially the force required to overcome the frictional forces experienced by the far-field flow. The drag component resulting from accelerating the air disappears. Period (B) is that period beginning when the vehicle reaches its final velocity. In this period a transition occurs from the conditions required to accelerate the far-field air and overcome the frictional forces to new conditions only required to overcome the far-field frictional forces. Period (C) follows period (B). In this period the flow conditions approach steady state conditions. However, steady state is never reached. In (C) the variations occurring in the values of drag and other properties is small with respect to the variations occurring in periods (A) and (B).

Fig. (10) shows the variation of pressure with time at the forward and rear far-field, near-field interfaces ($x_1(t)$ and $x_4(t)$) and the forward and rear ends of the annular region ($x_2(t)$ and $x_3(t)$). Initially the pressure at all the above stations has its undisturbed value p_o. As the vehicle accelerates (period A) the pressure values at the two forward stations ($x_1(t)$ and $x_2(t)$) increase with time while the corresponding values at the rear stations ($x_3(t)$ and $x_2(t)$) decrease with time. The gap between the pressure values at the forward and rear stations continues to increase until the acceleration period comes to an end. The flow velocity in the annular region is negative (Fig. (12)). Its magnitude increases with time (relative to both the tunnel and the vehicle) during the acceleration period. Therefore the pressure drop due to friction in the annular region increases during the

period (A) as observed above. At the end of this period the magnitude of the flow velocity in the annular region decreases slightly (period B), then it approaches a constant value (period C). A corresponding slight pressure drop is observed between the annular region ends (B), after which differences in pressure at the near-field stations approach constant values (period C).

As the vehicle approaches the forward tunnel end the lengths of the air columns ahead of it and behind it respectively decrease and increase with time. This causes a corresponding increase and decrease in the pressure drop in the rear and forward far-fields respectively. Consequently, a continuous drop occurs in the near-field pressure as the vehicle approaches the tube end. This is observed more clearly in Fig. (11) which shows the pressure variation along the tunnel for different times. (The steeper pressure gradient at $t^* = 20$ secs. is due to the additional inertial forces during the acceleration period.)

In Fig. (10) it is seen that the largest contribution to the pressure drop in the near-field occurs in the annular region. As will be seen later this causes a major part of the drag experienced by the vehicle. Fig. (12) which depicts the velocity variation with time at the four near-field stations reveals that the flow in the tunnel ahead and behind the vehicle moves with a sizeable velocity (~ 0.5 of the vehicle velocity). The friction forces experienced by the air column in the tube must be overcome by the vehicle which is effectively pushing this column and therefore appears as additional drag. The negative flow velocity in the annular region is also of sizeable magnitude

($\sim$ 0.5 of the vehicle velocity). This causes a large relative velocity between the vehicle and the air surrounding it, increasing the skin friction drag on the vehicle.

The effect of the above observations on the drag experienced by vehicles travelling in tubes becomes clear by examining the drag coefficient curves of Fig. (13). For C_{D_o} the maximum vehicle velocity V_o^* is used as the normalizing velocity

$$C_{D_o} = \frac{\text{Drag}}{(\frac{1}{2}\rho_o^* V_o^{*2}) \times (\text{vehicle c.s. area})}$$

For C_D the instantaneous vehicle velocity V^* is used as the normalizing velocity

$$C_D = \frac{\text{Drag}}{(\frac{1}{2}\rho_o^* V^{*2}) \times (\text{vehicle c.s. area})}$$

During the acceleration regime the drag increases monotonically (curve for C_{D_o}). It reaches its maximum value at the maximum velocity, then it decreases gradually and approaches a constant value. The drag coefficient C_D is seen to decrease monotonically with time throughout the vehicle's journey. As the unsteady effects diminish it is seen that the value of the drag coefficient is close to 15. This is a large value when compared to the corresponding C_D value of approximately 2 for the vehicle when travelling in free air.

It was mentioned above that although steady state conditions are approached in period (C) they are never reached. This is clear from Fig. (13) which shows a slight continuous decrease in drag throughout period (C), and from Fig. (12) which shows a slight continuous increase in flow velocity throughout period (C). (Note the increase in flow velocity reduces the pressure drop along the annular

region and therefore causes a corresponding reduction in the vehicle drag). The reason that steady state conditions are not reachable is due to the friction forces acting on the far-field flow. It is well known that the velocity of steady state flows in pipes with friction increase continuously as the end of the pipe is approached. So even if we assume that the far-field is in steady flow, the fact that the vehicle moves along the far field indicates that flow properties at the vehicle will continuously change.

The drag forces D^* acting on a vehicle travelling in a tube are divided into a skin friction drag D_F^* and a pressure drag D_p^*. The pressure drag D_p^* is further divided into three components. For the flow conditions resulting from the vehicle's motion in the tube, D_{pa}^* is the pressure drag which would result if there were no friction forces in the annular region (i.e. if there were no pressure drop along the vehicle length). D_{pb}^* and D_{pc}^* are the drag components resulting from the pressure drop in the annular region due to the frictional forces on the tunnel wall and the vehicle surface respectively. For a vehicle travelling in a tube the total drag experienced

$$D^* = D_F^* + D_p^*$$

where $$D_p^* = D_{pa}^* + D_{pb}^* + D_{pc}^*$$

However, for a vehicle travelling in free air the corresponding drag

$$\bar{D}^* = \bar{D}_F^* + \bar{D}_p^*$$

where $$\bar{D}_p^* = \bar{D}_{pa}^*$$

Therefore when a vehicle travels in a tube two additional components D^*_{pb} and D^*_{pc} are added to the drag components D^*_F and D^*_{pa}. Moreover a comparison of D^*_F and D^*_{pa} to $\bar{D}^*_F$ and $\bar{D}^*_{pa}$ reveals that each of the former two is greater than its corresponding component experienced in free air. D^*_F is expected to be higher than $\bar{D}^*_F$ because the flow velocity in the annular region is negative. Therefore, the relative velocity between the vehicle and the surrounding flow is greater for a vehicle travelling in a tube than the corresponding case of travel in free air. Consequently the frictional forces are greater for the first case than the second, and

$$D^*_F > \bar{D}^*_F$$

When comparing D^*_{pa} and $\bar{D}^*_{pa}$ we note that the base pressure in both the confined and unconfined cases is respectively given by

$$p^*_B = p^*_2 + \tfrac{1}{2} C_{pB} \rho^*_2 (V^* - U^*_2)^2$$

and

$$\bar{p}^*_B = \bar{p}^*_2 + \tfrac{1}{2} C_{pB} \rho^*_2 V^{*2}$$

recognizing that

$$U^*_2 < 0$$

$$C_{pB} < 0$$

$$p^*_2 < p^*_1$$

$$\bar{p}^*_2 = \bar{p}^*_1 = p^*_0$$

leads to the conclusion that

$$p^*_B < \bar{p}^*_B$$

and therefore

$$D^*_{pa} > \bar{D}^*_{pa}$$

Fig. (14) shows the contribution of each of the components discussed above to the total drag of the vehicle. It is seen that the pressure drag contribution to the total drag is larger than the skin friction drag contribution. It is also seen that the pressure drop in the annular region due to the vehicle friction composes a major part of the pressure drag.

b. Effect of the Parameters on the Solution

In this section solutions for different parameter values are obtained. The effect of varying the parameter values on the solution is discussed. In each case only one parameter is allowed to vary; the rest retain the values given above. In Figs. (15)-(22) the effect of changing the parameter values on the drag coefficient is shown. Tables (1)-(3) respectively show the effect of parameter changes on the flow pressure, velocity and the relative values of the drag components at the beginning of the period (C). In general it was observed that this period begins at a time close to 30 seconds after the vehicle begins its motion. Therefore unless otherwise specified the values in the tables are those for $t^* = 30$ seconds. Calculations made for obtaining the curves of Fig. (17) assumed a quasi-steady near-field assumption. All other Figs. were calculated taking the unsteady wave effect into account in the near-field calculations. The difference between both cases is discussed later.

Blockage Ratio:

The blockage ratio has a strong effect on the flow properties and the drag (Fig. 15). An increase in blockage ratio results in an increase in the magnitudes of both the far-field and the near-field flow velocities. The increased far-field flow velocity requires larger forces to be exerted by the vehicle, both to accelerate the air and overcome the frictional forces. This appears as a drag increase. The large (in magnitude) annular velocity accompanied by the small annular cross sectional area results in large pressure drops which contribute greatly to the pressure drag D_p^*.

The blockage ratio value strongly affects the value of the total drag experienced by the vehicle and the relative values of the drag components to the total drag. The rise in the annular region pressure drop for large values of σ increases the ratio of the pressure drag components due to annular pressure drop (D_{pb}^* and D_{pc}^*) to the total drag. This is increased from 41.1% for a blockage ratio of 0.45 to 76.1% for $\sigma = 0.8$. However, the skin friction drag component D_F^* is affected in a reverse manner ($D_F^*/D^* = 45.5\%$ for $\sigma = 0.45$ and $D_F^*/D^* = 16.7\%$ for $\sigma = 0.8$). As the blockage ratio decreases the contributions of D_{pb}^* and D_{pc}^* continue to decrease and they vanish completely as $\sigma \to 0$. As expected a large blockage ratio severely increases the total drag. (For $\sigma = 0.45$ and $\sigma = 0.8$ the maximum values for C_{D_o} respectively are ~ 10 and 35).

Vehicle Length:

An increase in the vehicle length causes a corresponding increase in the resistance experienced by the air flow in the annular region.

The effect of this is to reduce the magnitude of the flow velocity there, and consequently increase the far-field flow. The reduced near-field flow tends to decrease the pressure gradient in the annular region, and therefore the pressure drop. However, the increased vehicle length has the reverse effect. It tends to increase this pressure drop because of the increased area of the frictional surface. The latter effect is the dominant and it causes an increase in the contribution of both the drag components D_F^* and D_{pc}^*. The total additional drag experienced by a long vehicle as compared to a short one is essentially the force required to overcome the increased frictional forces acting on the higher far-field velocity. Fig. (16) compares the drag coefficient C_{D_o} for different vehicle lengths. As seen, the maximum value of C_{D_o} increases from 15 to 26 for an increase of vehicle length from 150 ft. to 600 ft. Table (3) shows that the base drag ratio to total drag is increased as the vehicle length is reduced.

Tube Length:

The resistance experienced by the far-field flow increases with the tube length. Therefore the far-field velocity decreases as the tube length increases. Consequently the magnitude of the flow velocity in the annular region increases with the tube length. This produces an increase in the annular region pressure drop and consequently a larger drag is experienced by the vehicle.

Fig. (17) shows the drag coefficient curves for three different tube lengths of 5, 000 ft., 10, 000 ft. and 20, 000 ft. For the first two tubes the vehicle begins its motion at x = 0. 3. For the longest tube

the motion starts at x = 0.15. (Since the initial vehicle position for each of the two longer tubes is $x^* = 3,000$ ft., this choice allows us to compare the effect of the position of the forward tube end on the solution.) As expected the curves indicate the increase in drag with tube length. It is interesting to compare the wave effect in the three cases. All three curves coincide for approximately the initial three seconds of motion. Until that time the solution is the same as that for an infinite tube, since the initial waves reflected from the tube ends have not yet reached the vehicle in any of the three cases. At approximately $t^* = 3$ secs. the compression wave reflected from the rear tube end arrives at the vehicle for the 5,000 ft. tube case. This causes a reduction in the slope of the drag curve compared to the corresponding slopes for the two longer tubes. At $t^* \sim 7$ seconds the expansion wave reflected from the forward tube end arrives at the vehicle. This causes an additional reduction in the slope of the drag curve. The curves corresponding to the longer tubes coincide until $t^* \sim 14$ secs. Until that time the solution is the same as that for a semi-infinite tube, since the initial compression wave reflected as an expansion wave from the far tube end has not yet reached the vehicle. At $t^* \sim 14$ secs. this wave reaches the vehicle in the medium length tube. Only then does a difference occur between the slopes of the curves corresponding to the two long tubes. The reflected wave has a stronger effect for the 5,000 ft. tube than for the 10,000 ft. tube. This is due to the attenuating effect of friction on the wave strength. The third curve (20,000 ft. tube) has a different profile from the first two. This is due to the fact that the reflected

expansion wave arrives at the vehicle after the end of the acceleration period. Therefore, at the end of acceleration the flow properties at the vehicle behave as if the tube is semi-infinite. And the argument previously used for the drag reduction at the end of period (A) applies here no longer. Although the rate of drag increase is reduced at the end of period (A), a continuous rise in the drag is observed. This is due to the fact that a vehicle in a semi-infinite tube must continuously supply the force required to push a fluid column continuously increasing in length with time. Therefore, although the drag force due to accelerating the far-field air column vanishes at the end of the accelerating period, a force is required to overcome the frictional forces on a continuously increasing frictional surface area. This causes the continuous increase in drag until the reflected expansion wave reaches the vehicle.

For a semi-infinite tube we expect the solution to behave in the following manner. Initially as the vehicle accelerates, compression and expansion waves respectively propagating ahead of the vehicle and behind it, cause the air in the tube to flow and a pressure gradient occurs. After the vehicle reaches a steady velocity the growing column of air flow in the far-field results in larger frictional forces. This tends to produce a rise in the far-field pressure drop along the tube. An equal pressure drop occurs in the near-field (see Fig. 11). However, for this to happen an increased flow velocity (in magnitude) must occur in the near-field. This implies a reduced velocity in the far-field, and consequently a reduced pressure gradient there. This continues until the near-field pressure drop

reaches its maximum value which occurs as the far-field velocity approaches zero. As this happens the pressure gradient along the far-field approaches zero. The far-field pressure upstream of the vehicle approaches the ambient pressure, while the pressure downstream of the vehicle approaches a constant value exceeding the ambient pressure by the pressure jump along the near-field. For the case of zero far-field flow the value of C_{D_o} (for our example) is approximately 70. (This is calculated assuming incompressible flow).

Vehicle Skin Friction Factor:

An increase in the vehicle roughness (skin friction) causes a corresponding increase in the resistance experienced by the air flow in the annular region. The magnitude of the flow velocity there is reduced while an increase occurs in the far-field velocity. Also an increase in both the near-field pressure drop and the drag forces occurs. These are the same observations made for increasing the vehicle length. Tables (1)-(3) and Figs. (16), (18) reveal the strong similarity between the effect of vehicle length and the vehicle skin friction on the solution. We note that an increase in the value of either is equivalent to an increase in the total skin friction force acting on the vehicle surface, and therefore the similarity in their effects.

Tube Skin Friction Factor:

Increasing the tube roughness (friction factor) has the same qualitative effects on the pressures, velocities and drag as those produced by an increase in tube length. Fig. (19) gives the drag

coefficient curves for three different values of f_T. It is interesting to note that as the value of f_T is increased the two periods (B) and (C) become less distinct from each other. The reason for that is that for large values of f_T the major part of the vehicle drag during the acceleration period is due to the frictional forces acting on the far-field flow and not to accelerating that flow. Therefore, when the acceleration comes to an end no substantial reduction occurs in the drag.

Base Pressure Coefficient:

From Fig. (20) and Tables (1)-(3) we see that varying the value of the base pressure coefficient C_{pB} from -0.075 to -0.30 causes only small corresponding variation in the solution. For the vehicle length considered (300 ft.) only about 10% of the total drag is due to the nose-base effect. The major portion of the drag is due to annular frictional forces. However, the contribution of the nose-base effect increases as the vehicle length is decreased (20% for 150 ft. long vehicle).

Maximum Vehicle Velocity:

In our examples we assumed that the vehicle travels at a constant acceleration (5 ft./sec^2) during period (A). The initial increase in slope of the curves for U_1 and U_4 ($t^* < 10$ secs) in Fig. (12) indicates that the far-field flows with an increasing acceleration initially. For the rest of period (A) the acceleration becomes nearly constant. This is approximately 3 ft/sec^2. During the acceleration period, for $V_o^* = 75$ ft/sec, 100 ft/sec, 150 ft/sec., the respective values for $U_1^*(t^*)/V^*(t^*)$ vary between 0.27, 0.32,

0.39 at the middle of this period to 0.39, 0.45, 0.50 at the end of it. The far-field velocity continues to increase during period (B) and as shown in Table (2), U_1 reaches the values 0.46, 0.48, 0.51 at the end of that period for the above given values of V_o^*. The velocities U_1, U_2, U_3, U_4 at the end of period (B) (see Table 2) do not vary appreciably with changing the maximum vehicle velocity. Therefore, the velocities U_1^*, U_2^*, U_3^*, U_4^* increase in magnitude with the vehicle's final velocity. Correspondingly the pressure drop in the annular region and the total drag increase as the final vehicle speed is increased.

Fig. (21a) compares the drag coefficient C_{D_o} for different values of V_o^*. It is seen that the lower values for $C_{D_o max}$ (the maximum value of C_{D_o}) correspond to the higher final vehicle velocities. This may be explained in the following manner. Let us consider the flow for times large enough so that we may assume that the flow acceleration in the tube is constant ($= S\,\theta^*$) where θ^* is the vehicle's acceleration and S is a constant. The flow in the far-field is approximated by an incompressible flow with velocity

$$U_F^* = C_1^* + S\,\theta^*\,t^*$$

where C_1^* is a constant. During the acceleration period, the drag experienced by the vehicle is proportional to the forces required to accelerate the far-field flow in addition to the frictional forces acting on that flow. The former force is proportional to $\frac{d\,U_F^*}{dt^*}$ and the latter is proportional to U_F^{*2}. We therefore conclude that

$$C_{D_o} \propto \left(\frac{C_1^*}{V_o^*} + \frac{S\theta^* t^*}{V_o^*} \right)^2 + C_2 \frac{S\theta^* L^*}{V_o^{*2}}$$

and

$$C_{D_o max} \propto \left(\frac{C_1^*}{V_o^*} + S \right)^2 + C_2 \frac{S\theta^* L^*}{V_o^{*2}}$$

where C_2 is a constant. Therefore higher values of $C_{D_o max}$ correspond to lower values of V_o^*.

Comparing the slopes of the C_{D_o} curves in period (C) we find that it increases in absolute value as V_o^* increases. This is due to the higher far-field flow velocities (and therefore Mach number) corresponding to the higher V_o^* values, and therefore the greater effect of compressibility which leads to the increased slope. In Fig. (21b) in all three cases, the drag is normalized by the intermediate final speed (100 ft/sec). This figure allows us to obtain a better idea about the effect of the velocity on the drag.

It is of interest here to point out the scaling laws and the dimensionless similarity parameters related to the train-tube problem. Let us assume that a vehicle travels in a tube of length L^*. Its acceleration is given by θ^* and its final speed is V_o^*. We now consider a small-scale model which is geometrically similar to the above full-scale tube-vehicle system. We assume that the friction coefficients for the model surfaces are equal to the corresponding full-scale coefficients. We are at liberty to choose the model tube length L_m^* (and thus the model size) and the final vehicle velocity of the model $V_{o\,m}^*$. For both the solutions of the model and the full-scale system to be similar, the value of the model's

vehicle acceleration θ_m^* in the period (A) must be chosen such that the similarity parameter $\left(\frac{L_m^* \theta_m^*}{V_{o\,m}^{*2}}\right)$ and $\left(\frac{L^* \theta^*}{V_o^{*2}}\right)$

Moreover, the scaling of the time follows the relation

$$t_s = t_m^* \frac{V_{o\,m}^*}{L_m^*} = t^* \frac{V_o^*}{L^*}$$

In addition to the above (in order to achieve the same compressibility effect) the equality of Mach numbers must be satisfied

$$M_o = \frac{V_o^*}{a_o^*} = \frac{V_{o\,m}^*}{a_{o\,m}^*}$$

where $(\ )_m$ indicates model properties. If the above scaling laws are satisfied, the curves for $C_{D_o m}$ vs. t_s and C_{D_o} vs. t_s coincide. Here

$$C_{D_o m} \equiv \frac{D_m^*}{\frac{1}{2} \rho_{o\,m}^* V_{o\,m}^* \times (\text{model vehicle c.s. area})}$$

In investigating various aspects related to the problem of vehicles travelling in tubes, experiments are conducted using small-scale equipment. In order that the information obtained from such experiments be useful and applicable to full-scale systems, the above (scaling) conditions must be satisfied. The equality of the Reynolds number was not mentioned here, since we assumed that the surface friction coefficients are equal in both the model and full-scale systems. This can be approximately achieved by a proper choice of the model surface roughness. Otherwise the model's Reynolds number must be controlled by such methods as pressurization and the employment of gases other than air. To achieve

the equality of Mach numbers, a small-scale model may be used in air with the same V_o^* value ($V_{o\,m}^* = V_o^*$). However, the model acceleration is required to exceed the corresponding full-scale acceleration. If the model is operated at lower velocities, a working gas other than air must be properly chosen. We may add that for cases where the compressibility effects are not of significant importance (e.g. low vehicle velocities), the condition of Mach number equality may be neglected.

Far-Field Velocity Profile:

It is seen from Fig. (22) that the velocity profile has a negligible effect on the solution. The velocity profiles were of the form

$$\frac{u^*}{\hat{U}^*} = f(\eta) = \eta^{\frac{1}{n}}, \qquad n = 4,\ 6,\ 10$$

For the case n = 4 the boundary layer began to fill the tube at approximately 17 seconds from the beginning of motion. For the case n = 10 the corresponding time was approximately 12 seconds. It is therefore also concluded that the difference between the solution using a potential core formulation or just assuming the flow is fully developed to begin with is negligible.

c. Comparison of Different Flow Models

Except for the tube length comparison, all the above examples were calculated using an unsteady near-field formulation. At the initial instants of the motion ($\sim$ 2 seconds) the flow in the annular region is assumed to be inviscid and the friction effect there is neglected. After this period the full equations are solved taking account of both the friction and wave effect.

The Quasi-Steady Near Field Assumption:

Fig. (23) compares the unsteady near-field solution to the quasi-steady near-field solution for a vehicle 600 ft. long. It is seen that both solutions give almost identical results except for the initial moments of the motion where the frictional forces in the near-field are weak and the wave effect is dominant. This leads to the conclusion that except for a small initial period the frictional effects in the annular region are much stronger than the wave effects, and therefore the latter may be neglected (quasi-steady near-field assumption). It is also clear that the initial difference in the resulting solution does not affect the solution at later times.

The Slug Theory:

This theory assumes a one-dimensional incompressible uniform flow formulation for both the far-field and the near-field. This formulation leads to an ordinary differential equation solvable numerically.

Fig. (24a) compares our solutions to that obtained by the slug theory for parameters of standard values. The overestimation of

drag predicted by the slug theory during period (A) is due to the instantaneous and abrupt changes that take place in the far-field (infinite sound speed). For example, the whole far-field air column is abruptly accelerated unlike the compressible solution in which the accelerated column increases its length gradually. The underestimation predicted in period (B) is also due to the lack of waves. In period (C) the slug theory predicts a constant value for the drag (i.e. steady state is actually achieved). This is due to the assumed incompressibility of the flow. The importance of compressibility increases with U^*/a_o^*, f_T, L^*, $\frac{\partial(U^*/a_o^*)}{\partial t^*}$. An increase in the wave effect occurs as the latter two quantities increase. For low values of the above quantities, it is adequate to use the slug theory. The quantities U^*/a_o^* and $\frac{\partial(U^*/a_o^*)}{\partial t^*}$ are related to the parameters discussed above. For example, increasing the value of V_o^* increases the flow Mach number, while an increase in σ, L_{vh}^*, f_{vh} results in a corresponding increase in both (U^*/a_o^*) and $\frac{\partial(U^*/a_o^*)}{\partial t^*}$. Fig. (24b) is an example for the increased disagreement between the compressible flow solution and the incompressible slug model in the case of a long tube (20, 000 ft.).

III. THE PROBLEM OF A VENTED TUNNEL

A. Formulation of the Problem

Vents are usually found in train tunnels. The vent effectively reduces the tunnel length and thus the aerodynamic resistance experienced by the train is reduced. We consider here a tunnel with one vent along its length. The flow through the vent depends on its position relative to the vehicle. When the vent is ahead of the vehicle the vent pressure (inside the tube) is higher than the ambient pressure p_o. This pressure difference results in an outflow through the vent, which continues until the train approaches the vent. As the vent becomes in the annular region, a gradual reduction in its pressure occurs. The flow in the vent is reversed after its pressure becomes equal to ambient, as the lower pressure results in an inflow through the vent.

Experiments were conducted at DSI (Reference 6) to study steady flow in vented tubes. From this investigation coefficients and constants found to be appropriate for describing vent flow were defined. In the following equations subscript (a) denotes flow conditions upstream of the vent and subscript (b) denotes conditions downstream of the vent.

$$\frac{p_a - p_o}{\frac{1}{2}\rho_a U_{vt}^2 M_o^2 \gamma} = \begin{cases} \dfrac{C_{\Delta pso}}{K_o^2} & U_{vt} > 0 \qquad (54a) \\ -\dfrac{C_{\Delta psi}}{K_i^2} & U_{vt} < 0 \qquad (54b) \end{cases}$$

where

$$U_{vt} = \begin{cases} \dfrac{U_a - U_b}{\sigma_{vt}} & \text{(vent in far-field)} \qquad (55a) \\ \dfrac{U_a - U_b}{\sigma_{vt}}(1-\sigma) & \text{(vent in annular region)} \qquad (55b) \end{cases}$$

σ_{vt} ≡ vent cross sectional area divided by tunnel cross sectional area

The constants

$K_o = 1.05$

$K_i = 0.965$

The values of the coefficients $C_{\Delta pso}$ and $C_{\Delta psi}$ depend on the geometry at the vent shaft. For existing subway vent shafts, their values vary between 5.0 and 15.0.

The experiments showed that for inflow and outflow through the vent, there is respectively a pressure drop and rise between stations (a) and (b). This agrees qualitatively with pressure changes predicted by Bernoulli's equation for the case of inviscid flow. The magnitude of the difference between the pressures at stations (a) and (b) was found to be equivalent to the pressure drop over a few tunnel diameters and is neglected here. We therefore assume that

$$p_a = p_b \tag{56}$$

The flow at the vent is quite complicated and the inviscid core and boundary layer formulation does not apply there. Moreover, the results obtained in Part (II) indicate that the flow velocity profile has a negligible effect on the solution and that the inviscid core and boundary layer formulation may be replaced by a fully developed flow formulation from the beginning of the motion with no noticeable error resulting. Therefore, in order to study the effect of the vent we shall assume that the flow is fully developed and uniform at any cross section. We also use the relation

$$\rho_a = \rho_b \tag{57}$$

The quasi-steady near-field assumption is used for calculations in this section.

B. Method of Solution

The same methods of solution used in the problem of an unvented tube are used here. The only additional feature here is the solution at the vent itself. The vent flow is related to the flow in the tube through the far-field equations along characteristics I, II, III (see Fig. 8). The characteristic equations are written in their approximate form (50) and when combined with the above equations governing the vent flow, the problem for finding the flow variables at the vent is reduced to solving an algebraic system of equations

$$\underset{\sim}{G}(\underset{\sim}{W}) = 0$$

where

$$\underset{\sim}{W} = \begin{bmatrix} \underset{\sim}{w}(x_a, t_{n+1}) \\ \underset{\sim}{w}(x_b, t_{n+1}) \\ x_I \\ x_{II} \\ x_{III} \end{bmatrix}$$

This is solved by iteration.

If the vehicle is close to the vent as shown in Fig. (8) at time t_2, then the vent and near-field equations are solved simultaneously. At time t_3 the vent is in the near-field and therefore the vent flow is related to the far-field indirectly through the far-field equations along the characteristic curves leading to the vehicle as shown in the figure.

C. Numerical Calculations and Results

1. Choice of Parameter Values

To demonstrate the vent effect on vehicles travelling in tubes a numerical example is given. Except for the value of n, the values of the parameters are the same as those given on page (40). (The flow is assumed to be uniform here. Therefore $n \to \infty$). In addition the following vent parameters are assumed

Vent position $x_{vt} = 0.6$

$\sigma_{vt} = 0.75$

$C_{\Delta psi} = 7$

$C_{\Delta pso} = 7$

2. Results and Discussion

Figs. (25)-(27) show the variation of the pressure, flow velocity and the drag coefficient with time for the case of a vehicle travelling in a vented tube. Before the vehicle reaches the vent, the above properties change with time in a similar pattern to that observed for an unvented tube. However, a reduction in both the annular region pressure drop and the drag experienced by the vehicle occurs due to the vent. The pressure at the vent is greater than the ambient pressure. Therefore an outflow occurs through the vent and the flow velocity U_b after (downstream) the vent is less than the flow velocity U_a before (upstream) the vent. As the vehicle passes the vent a change in the flow properties occurs. The relatively slow flow ahead of the vent is suddenly compressed causing a compression wave to travel down the tube. This is reflected as an expansion wave at the forward tube end. While the vent is in the annular region, a

continuous drop in its pressure occurs. At some point this pressure becomes equal to ambient. Then as it continues to decrease, the vent flow is reversed and the velocity downstream of the vent exceeds that upstream. The pressure at the vehicle's forward end continues to increase until the reflected expansion wave reaches the vehicle. After that the normal pattern for the variation of pressure with time in an unvented tube is observed here.

Fig. (27) shows the variation of the drag coefficient with time. In addition to the initial drag increase which is due to the acceleration of the air in the tube, a sudden increase in drag as the vehicle's forward end passes the vent is observed. As the vent comes into the annular region, its venting effect is gradually reduced until its pressure becomes equal to ambient. At that point there is zero vent flow and the maximum drag is experienced. As the vehicle continues its motion by the vent, the pressure drop at the vent produces an inflow and the venting effect is felt again. This causes a reduction in the drag until the rear end of the vehicle passes the vent. An increase in drag is then observed. This is the same increase which would occur if the tube were semi-infinite. The fact that the tube is of finite length is not felt until the reflected expansion wave reaches the vehicle and causes a drop in its drag.

In Fig. (28) the drag coefficient for a vehicle travelling in a vented tube is compared with the corresponding drag coefficient for a vehicle travelling in an unvented tube. The vent effect is seen to reduce the drag to 78% before the vent is reached and to 70% after the vent is passed. However, at the vent itself the drag exceeds that of

an unvented tube. The reason for the increased reduction in drag after the vent is passed is that for our example the tube length after the vent is less than its length before the vent. Therefore, the tube's effective length is reduced after the vehicle passes the vent.

In the same figure a comparison is made between the present solution and that obtained by the slug theory. In addition to the observations previously made about the slug theory solution in the case of an unvented tube, this theory predicts an extra large drag as the vehicle passes the vent. There is also an abrupt decrease in drag after the vent is passed. Both of these observations are due to neglecting the wave effect in the slug theory.

IV. THE PROBLEM OF A VEHICLE ENTERING A TUNNEL AT FINITE SPEED

A. Formulation of the Problem

A vehicle approaching a tunnel causes a slight disturbance to its air just before the nose enters the tunnel. As the nose enters the flow is continuously compressed until the nose is completely in the tunnel. As shown in Appendix (A) the influence of the nose is not expected to be felt in the tunnel until it becomes very close. The nose itself is short and the time required for it to complete its entry is short. The manner in which the air is compressed in this short initial period (~ 0.2 seconds) depends on the geometry of the nose. However we have not been considering such details in this study, and recognizing that the change of pressure with respect to the undisturbed pressure is small (~ 0.1) we can conclude that replacing the continuous compression wave by a shock wave would give negligible error (the entropy increase for a weak shock wave is of the third order with respect to its strength).

Determining the Inititial Shock Strength

The initial shock strength is determined when the vehicle nose is completely inside the tube and station (2) (the beginning of the annular region) is at the tube entrance (see Fig. 9b). The equations governing the flow properties behind the shock wave are

$$U_z = \frac{2}{\gamma+1} \frac{c_s}{M_o}\left(1 - \frac{1}{c_s^2}\right) \tag{58}$$

$$p_z = \frac{1}{\gamma+1}(2\gamma\, c_s^2 - \gamma + 1) \tag{59}$$

$$\rho_z = \frac{1}{1 - \frac{U_z}{c_s} M_o} \tag{60}$$

where c_s is the dimensionless shock speed

$$c_s = \frac{c_s^*}{a_o^*}$$

and variables with subscript z indicate properties immediately behind the shock wave. The shock wave is assumed to be close to the vehicle and flow properties behind the shock are matched to those at station (1).

$$U_z = U_1 \qquad p_z = p_1 \qquad \rho_z = \rho_1$$

Conditions at station (1) are governed by the nose region relations (equations 33a, 33b, 33c) in addition to the condition

$$p_2 = 1 \tag{61}$$

The above shock relations and the nose region equations combined with condition (61) are solved for the initial properties behind the shock, the initial shock speed and the flow properties at station (2).

Interaction Between the Shock Wave and the Characteristics:

As the shock propagates down the tube with a speed less than that of the characteristics behind it, an interaction between the shock and the characteristics is expected. This produces changes in the shock strength and consequently its velocity. The new shock strength is found by determining the pressure on the characteristic curve at the point of its intersection with the shock. The new shock velocity is calculated from equation (59).

The Near-Field:

As the vehicle proceeds into the tunnel equations (37) governing the flow in the annular region are applied between stations (2) and the tunnel entrance. After the whole vehicle completely enters the tunnel, the base region equations (44)-(46) are applied in addition to the nose and annular region equations.

The Far-Field:

The far-field flow is governed by the same far-field equations derived for the problem of a vehicle accelerating in an unvented tube.

B. Method of Solution

The same methods of solution used in the problem of an unvented tube are used here. The only additional feature here is the solution as the vehicle enters the tube. Fig. (9a) at time t_1 shows the near-field and far-field characteristics along which the corresponding flow equations are solved in combination with the equations governing the flow in the nose region. At time t_2 in the same figure the vehicle is completely inside the tube and the characteristic curves are also shown in this case.

C. Numerical Calculations and Results

In the numerical examples of this section a vehicle is assumed to be travelling at a constant speed V_o^*. It enters the tunnel at time $t^* = 0$. Unless otherwise specified the same geometrical parameters given on page (40) are assumed here.

Results and Discussion:

Fig. (29) shows the pressure variation with time at the four stations $x_1(t)$, $x_2(t)$, $x_3(t)$ and $x_4(t)$. The initial pressure rise ahead of the nose is due to the shock wave. As the vehicle proceeds into the tunnel a continuous increase in the pressure at the two forward stations $x_1(t)$ and $x_2(t)$ is observed. This is due to the increasing length of the annular region and therefore the increase in the pressure drop along it. As the base enters the tube, the annular pressure drop continues to increase, however at a lower rate than the initial period. This increase is due to the semi-infinite tube length effect which results in a velocity drop in the tube and an increase in the magnitude of the velocity in the annular region. The pressure ahead of the vehicle continues to increase until the expansion wave reflected from the tube's forward end arrives at the vehicle. Then the pressure drops and a pattern similar to that of period (C) in the problem of a vehicle accelerating in an unvented tube is observed here.

In Fig. (30) the pressure distribution is shown along the tube at different times. At $t^* = 4$ secs. and $t^* = 8$ secs. the shock wave is propagating towards the tube's forward end. It is clear that its strength is not noticeably affected as it propagates down the tube. The curve for $t^* = 12$ secs. shows the pressure distribution in the tube, as the reflected expansion wave propagates towards the vehicle.

The drag variation follows a similar pattern to the pressure variation ahead of the vehicle. In Fig. (32) an initial large drag is

observed due to the initial compression of the air at the tube's entrance. The drag increases at a high rate until the vehicle is completely in the tube. After that the drag continues to increase at a lower rate, until the reflected expansion wave arrives at the vehicle, reducing the drag to the values observed in the final period (C) of a vehicle accelerating in an unvented tube.

In Fig. (32) a comparison is made between the solution for the entry problem and the slug theory solution for the same case. The latter solution does not include the shock wave which is part of the compressible solution. The vehicle is assumed to accelerate all the air column in the tube instantaneously as it enters the tube. This causes the sharp increase in drag predicted by the slug theory. Unlike the compressible solution, the fact that the tube is of finite length is felt instantaneously. Therefore a sharp drop in the drag is observed immediately after the vehicle completes its entry into the tube.

Solutions obtained in this section assume nonsteady near-field flow. They were compared to the solution assuming the near-field to be quasi-steady and no noticeable difference was found.

Effect of the Parameters on the Solution:

Tables (4) and (5) show the effect of changing the values of the parameters on the pressure and the drag.

Blockage Ratio:

Increasing the blockage ratio has two effects which contribute to increasing the value of the maximum drag experienced by the vehicle. The initial shock wave strength increases with the blockage

ratio, indicating a corresponding increase in the initial drag. Moreover, the large pressure drop in the annular region of a high blockage ratio vehicle causes the rate of drag variation to increase with blockage ratio during the initial unsteady periods $t^* < t_j^*$ (see Fig. 29). Therefore, the value of the drag before the vehicle is affected by the expansion wave is much larger for high blockage ratio vehicles as compared to low blockage ratio vehicles.

Vehicle Length:

The length of the vehicle does not affect the value of the shock strength. However, the initial period $0 < t^* < t_i^*$ (see Fig. 29) in which the drag increases at a very steep rate is prolonged and thus contributing to a large maximum drag value at $t^* = t_j^*$.

Tube Length:

The length of the tube does not affect the initial drag value or the value at $t^* = t_i^*$ (in the examples given here). However, an increase in the tube length causes an increase in the value of the time t_j^* at which the reflected expansion wave arrives at the vehicle. Therefore, the increased length of this period in which the drag increases at a positive rate results in a corresponding increase in the maximum drag value.

Other Parameters:

The drag increases with the vehicle skin friction factor as a result of the increase in the annular region pressure drop. An increase in the tube skin friction coefficient also causes an increase in drag, as the flow in the tube experiences higher resistance which must be overcome by the vehicle. The value of the base

friction coefficient is seen to affect the drag slightly. An increased velocity results in a stronger shock wave and a higher drag. However, the value of the drag coefficient C_{D_o} drops as the velocity increases.

V. CONCLUSIONS

Vehicles travelling in tunnels experience drag forces which are much higher than those experienced in free air. The major drag component results from the annular region pressure drop which is primarily due to the frictional forces on the vehicle surface. The nose-base contribution to the drag is small. However, it increases in importance as the vehicle length decreases. The blockage ratio, vehicle length, tube length, tunnel and vehicle skin friction and the vehicle velocity affect the drag experienced by the vehicle strongly. For vehicles of lengths considered here ($\sim$ 300 ft.) the drag is a weak function of the base pressure coefficient. The flow velocity profile in the far-field has a negligible effect on the solution.

For vehicles accelerating from rest, the wave action in the near-field is strong only for a small period of the initial motion ($\sim$ 2 seconds). As the vehicle velocity increases, a flow with negative velocity of large magnitude relative to the vehicle causes a large pressure drop in the annular region due to the large frictional forces there. The frictional effects in the annular region become dominant and the wave effects become negligible.

The wave effects in the far-field are more important than in the near-field. The effect of compressibility in the far-field flow increases with the quantities U^*/a_o^*, f_T, L^*, $\dfrac{\partial(U^*/a_o^*)}{\partial t^*}$.

The effect of including the boundary layer and potential core formulation on the solution is negligible. Therefore, a fully developed flow formulation since the beginning of motion may be assumed.

Except for the period in which the vehicle passes a vent and a following period whose duration depends on the length of the tube portion downstream of the vent, the flow properties at the vehicle and the drag experienced by it follow a similar pattern to that of an unvented tube. However, their values indicate a decrease in the tube effective length, resulting in a reduction of drag. At the vent itself the vehicle suddenly experiences a large drag when it meets the slow moving air in the forward section of the tube.

The slug theory overestimates the sharp drag increase experienced at the vent and underestimates the drag in the period immediately following. This is due to the infinite speed of sound assumed in that theory.

The solution for the problem of a vehicle entering in a tube at finite speed can be divided into three distinct periods. In the first period a sudden increase in the vehicle's drag is observed due to the propagation of a shock wave down the tube as the nose enters the tube. This is followed by an increase in drag at a high rate until the vehicle is completely in the tube. In the second period the drag continues to increase at a lower rate. The drag increase here is due to the semi-infinite tube length effect. In the third period the reflected expansion wave reaches the vehicle producing a drag reduction. Then a pattern similar to that of the final period of a vehicle accelerating in an unvented tube is observed here.

The slug theory predicts an overestimated value for the drag in the initial period. This suddenly drops giving an underestimated value in the second period. The slug theory in the third period gives a closer estimate to the true drag.

REFERENCES

1. Goodman, T. R., Lehman, A. F., "Static Aerodynamic Force Measurements of Bodies in Tubes," Technical Report No. 68-45, Oceanics Inc., Plainview, N. Y., April 1968.

2. Gouse, Jr. S. W., Nwude, Jr., "Aerodynamic Drag on Vehicles in Enclosed Guideways," Report No. DSR 76108-1, Department of Mechanical Engineering, Massachusetts Institute of Technology, Cambridge, Massachusetts, December 1966.

3. Gouse, Jr. S. W., Noyes, Jr. B. S., Swarden, M., "Aerodynamic Drag on a Body Travelling in a Tube," Report No. DSR 76108-3, Department of Mechanical Engineering, Massachusetts Institute of Technology, Cambridge, Mass., October 1967.

4. Hoppe, R. G., Gouse, Jr. S. W., "Fluid Dynamic Drag on Vehicles Travelling Through Tubes," Report No. CMU 1-59076-1, Department of Mechanical Engineering, Carnegie-Mellon University, Pittsburgh, Pennsylvania, August 1969.

5. "Subway Aerodynamic and Thermodynamic Test (SAT) Facility Single-Track Aerodynamic Data," Technical Report No. UMTA-DC-MTD-7-72-15, Developmental Sciences, Inc., Aerospace Technology Division, City of Industry, California, May 1972.

6. "Vent and Station Test (VST) Facility Vent Shaft Testing," Technical Report No. UMTA-DC-MTD-7-71-21, Developmental Sciences, Inc., Aerospace Technology Division, City of Industry, California, August 1971.

7. "Data Acquisition for Vehicles in Confined Spaces (VICS-70) Facility," Technical Report No. UMTA-DC-MTD-7-71-8, California Institute of Technology, Pasadena, California, June 1971.

8. "Experimental Aerodynamic Characteristics of Vehicles in Confined Spaces," Technical Report No. UMTA-DC-MTD-7-72-13, California Institute of Technology, Pasadena, California, December 1972.

9. Sajben, M., "Fluid Mechanics of Train-Tunnel Systems in Unsteady Motion," AIAA Paper No. 70-141.

10. "Aerodynamic Analysis of Vehicles in Tubes," TRW Systems Group, Washington Operations, Washington, D. C., April 1968, NTIS No. PB 176-796.

11. Hammitt, A., Hersh, A., Murthy, K., Peterson, J., Bliss, D., "Drag of Vehicles Travelling in Tubes," AIAA Paper No. 68-160.

12. Hammitt, A. G., "Aerodynamics of Tube Vehicle Systems," High Speed Ground Transportation Journal, Vol. IV, No. 3, September 1970, pp. 363-377.

13. Hammitt, A. G., "Aerodynamic Analysis of Tube Vehicle Systems," AIAA Journal, Vol. 10, No. 3, March 1972, pp. 282-290.

14. "Preliminary Wave Analysis of Unsteady Subway Vehicle Aerodynamics," Technical Report No. UMTA-DC-MTD-7-71-33, California Institute of Technology, Pasadena, California, October 1971.

15. Strom, C. R., "Tube Vehicle Aerodynamic Drag Prediction Using Experimental Data in Conjunction with a MITRE Analysis," MITRE Technical Report No. MTD-1690, The MITRE Corporation, Westgate Research Park, McLean, Va., March 1971.

16. Strom, C. R., "An Analytical Procedure for Calculating the Aerodynamic Performance of Vehicles Travelling in Tunnels," MITRE Technical Report No. MTR-6299, The MITRE Corporation, Westgate Research Park, McLean, Va., December 1972.

17. Benson, B. S., Garg, R. D., Woods, W. A., "Unsteady Flow in Pipes with Gradual or Sudden Area Changes," Institute of Mechanical Engineers. Proceedings, 1963-64, Vol. 178, Pt. 3 I(iii), Paper 9.

18. Mair, W. A., "The Effect of a Rear-Mounted Disc on the Drag of a Blunt-Based Body of Revolution," The Aeronautical Quarterly, Vol. 16, 1965.

19. Hoerner, S. F., "Base Drag and Thick Trailing Edges," Journal of the Aeronautical Sciences, Vol. 17, 1950.

20. Chevray, R., "The Turbulent Wake of a Body of Revolution," Journal of Basic Engineering (ASME Transactions, Series D), Vol. 90, 1968.

21. McErlean, D. P., Przirembel, C. E. G., "The Turbulent Near Wake of an Axisymmetric Body at Subsonic Speeds," AIAA Paper No. 70-797.

22. Courant, R., Hilbert, D., Methods of Mathematical Physics, Vol. II, Interscience Publishers, 1962.

23. Richtmyer, R. D., Morton, K. W., Difference Methods for Initial-Value Problems, Interscience Publishers, Second Edition, 1967.

24. Isaacson, E., Keller, H. B., Analysis of Numerical Methods, John Wiley and Sons, Inc., 1966.

25. Schlichting, H., Boundary-Layer Theory, McGraw-Hill Co., Inc., Sixth Edition, 1968.

26. Shapiro, A. H., The Dynamics and Thermodynamics of Compressible Fluid Flow, Ronald Press, 1954.

TABLE 1

Pressure Values at the Beginning of Period (C)†

Perturbed Parameter	Value of Perturbed Parameter	P_1	P_2	P_3	P_4
None		1.0368	1.0255	0.9676	0.9725
σ	0.45	1.0102	1.0032	0.9850	0.9894
σ	0.80	1.0946	1.0812	0.9359	0.9392
L^*_{vh}	150 ft.	1.0261	1.0116	0.9723	0.9784
L^*_{vh}	600 ft.	1.0510	1.0427	0.9624	0.9661
L^* ††	5,000 ft.	1.0183	1.0101	0.9721	0.9755
L^* †††	20,000 ft.	1.0798	1.0639	0.9733	0.9803
f_{vh}	0.01	1.0283	1.0146	0.9718	0.9776
f_{vh}	0.04	1.0495	1.0410	0.9611	0.9649
f_T	0.01	1.0215	1.0131	0.9748	0.9784
f_T	0.04	1.0615	1.0476	0.9569	0.9630
C_{pB}	-0.075	1.0366	1.0252	0.9670	0.9726
C_{pB}	-0.300	1.0371	1.0260	0.9687	0.9722
V^*_o ††	75 ft/sec	1.0220	1.0153	0.9821	0.9849
V^*_o †††	150 ft/sec	1.0626	1.0394	0.9133	0.9239
$\frac{1}{n}$ (velocity	1/4	1.0368	1.0255	0.9676	0.9724
profile power)	1/10	1.0368	1.0255	0.9676	0.9725

† Values correspond to $t^* = 30$ sec. in general

†† Values correspond to $t^* = 25$ sec.

††† Values correspond to $t^* = 40$ sec.

TABLE 2

Flow Velocity Values at the Beginning of Period (C)†

Perturbed Parameter	Value of Perturbed Parameter	U_1	U_2	U_3	U_4
None		0.4801	-0.4970	-0.5868	0.4455
σ	0.45	0.2711	-0.3318	-0.3573	0.2552
σ	0.80	0.6964	-0.5313	-0.7652	0.6465
L^*_{vh}	150 ft.	0.4096	-0.7042	-0.7715	0.3811
L^*_{vh}	600 ft.	0.5558	-0.2763	-0.3882	0.5147
L^* ††	5,000 ft.	0.5552	-0.2783	-0.3273	0.5359
L^* †††	20,000 ft.	0.3943	-0.7489	-0.9048	0.3347
f_{vh}	0.01	0.4263	-0.6550	-0.7263	0.3969
f_{vh}	0.04	0.5490	-0.2961	-0.4058	0.5085
f_T	0.01	0.5464	-0.3037	-0.3571	0.5255
f_T	0.04	0.4288	-0.6474	-0.7968	0.3723
C_{pB}	-0.075	0.4790	-0.5003	-0.5908	0.4444
C_{pB}	-0.300	0.4824	-0.4904	-0.5788	0.4475
V_o^* ††	75 ft/sec	0.4649	-0.5360	-0.5908	0.4437
V_o^* †††	150 ft/sec	0.5106	-0.4206	-0.6126	0.4375
$\frac{1}{n}$ (velocity	1/4	0.4800	-0.4973	-0.5871	0.4454
profile power)	1/10	0.4802	-0.4968	-0.5866	0.4455

†, ††, ††† have the same meaning as in Table 1.

TABLE 3

Ratio of the Drag Components to the Total Drag

at the Beginning of Period (C)†

Perturbed Parameter	Value of Perturbed Parameter	D_F^*/D^*	D_{pa}^*/D^*	D_{pb}^*/D^*	D_{pc}^*/D^*
None		0.278	0.111	0.078	0.533
σ	0.45	0.455	0.134	0.033	0.378
σ	0.80	0.167	0.072	0.094	0.667
L_{vh}^*	150 ft.	0.239	0.195	0.100	0.466
L_{vh}^*	600 ft.	0.310	0.067	0.033	0.590
L^* ††	5,000 ft.	0.289	0.117	0.039	0.555
L^* †††	20,000 ft.	0.267	0.111	0.111	0.515
f_{vh}	0.01	0.224	0.176	0.100	0.500
f_{vh}	0.04	0.320	0.060	0.040	0.580
f_T	0.01	0.300	0.114	0.041	0.545
f_T	0.04	0.244	0.094	0.106	0.556
C_{pB}	-0.075	0.255	0.100	0.078	0.539
C_{pB}	-0.300	0.278	0.128	0.072	0.522
V_o^* ††	75 ft/sec	0.278	0.111	0.078	0.533
V_o^* †††	150 ft/sec	0.278	0.100	0.078	0.544
$\frac{1}{n}$ (velocity	1/4	0.278	0.111	0.078	0.533
profile power)	1/10	0.278	0.111	0.078	0.533

†, ††, ††† have the same meaning as in Table 1.

TABLE 4

Pressure Values for the Entry Problem †

Perturbed Parameter	Value of Perturbed Parameter	$p(x_1(0), 0)$	$p(x_1(t_i), t_i)$	$p(x_1(t_j), t_j)$
None		1.026	1.069	1.087
σ	0.45	1.011	1.027	1.029
σ	0.80	1.052	1.119	1.183
L^*_{vh}	150 ft.	1.026	1.054	1.065
L^*_{vh}	600 ft.	1.026	1.090	1.112
L^*	5,000 ft.	1.026	1.069	1.077
L^*	20,000 ft.	1.026	1.069	1.101
f_{vh}	0.01	1.026	1.058	1.071
f_{vh}	0.04	1.026	1.083	1.111
f_T	0.01	1.026	1.065	1.075
f_T	0.04	1.026	1.078	1.109
C_{pB}	-0.075	1.026	1.069	1.087
C_{pB}	-0.300	1.026	1.069	1.088
V^*_o	75 ft/sec	1.016	1.046	1.054
V^*_o	150 ft/sec	1.053	1.123	1.178

† Refer to Fig. (29) for notation.

TABLE 5

Drag Coefficient Values for the Entry Problem†

Perturbed Parameter	Value of Perturbed Parameter	$C_{D_o}(0)$	$C_{D_o}(t_i)$	$C_{D_o}(t_j)$
None		5.664	18.319	23.769
σ	0.45	3.425	9.960	10.636
σ	0.80	9.933	26.464	42.881
L^*_{vh}	150 ft.	4.664	13.897	17.457
L^*_{vh}	600 ft.	7.664	24.235	31.017
L^*	5,000 ft.	5.664	18.319	20.597
L^*	20,000 ft.	5.664	18.319	27.787
f_{vh}	0.01	4.664	14.623	18.187
f_{vh}	0.04	7.664	22.711	31.660
f_T	0.01	5.664	17.475	20.728
f_T	0.04	5.664	19.680	28.683
C_{pB}	-0.075	5.589	18.257	23.642
C_{pB}	-0.300	5.814	18.322	24.010
V^*_o	75 ft/sec	5.935	21.232	25.367
V^*_o	150 ft/sec	5.274	14.596	22.317

† Refer to Fig. (29) for notation.

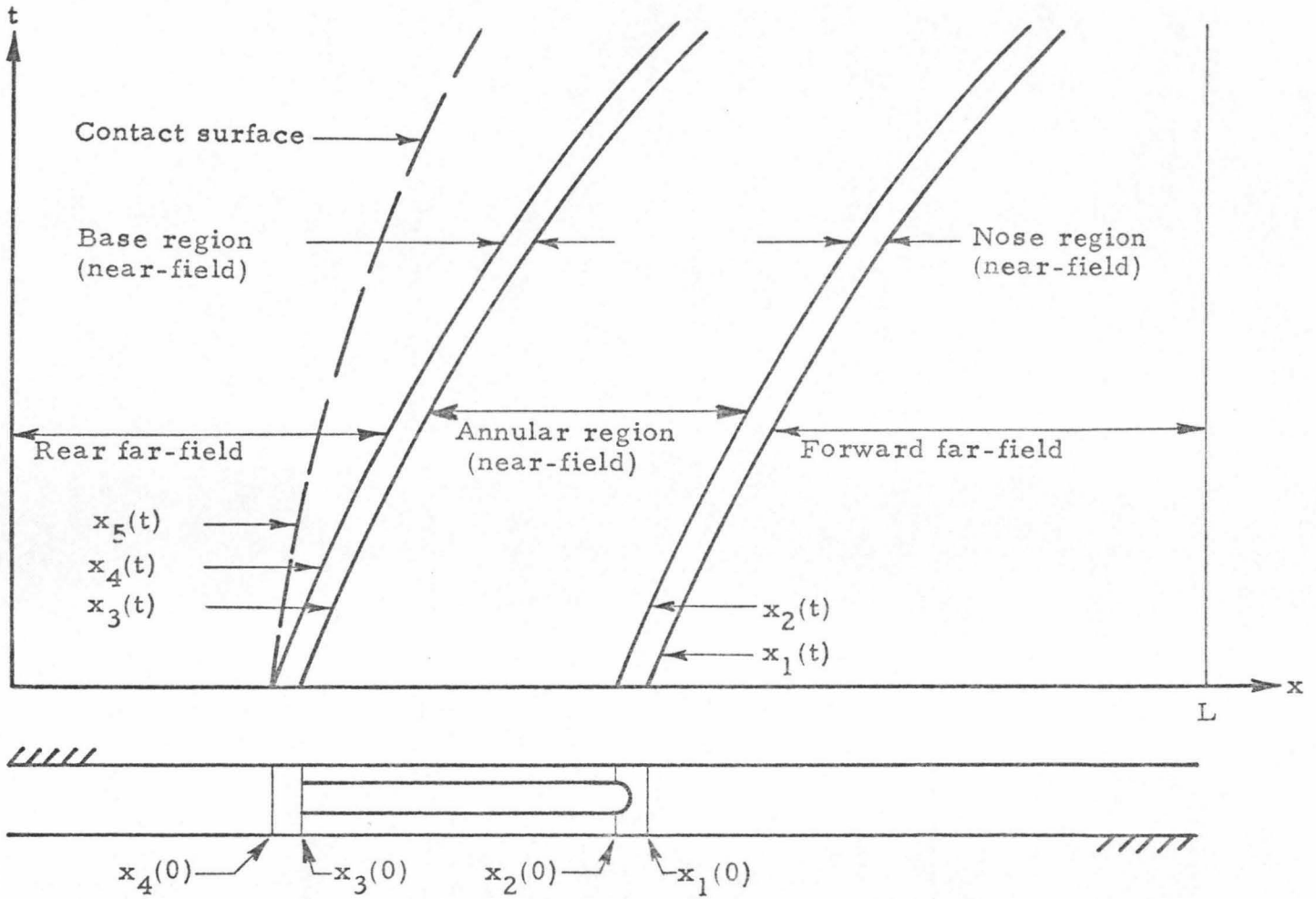

Fig. 1 x-t Diagram for a Vehicle Travelling in a Tube

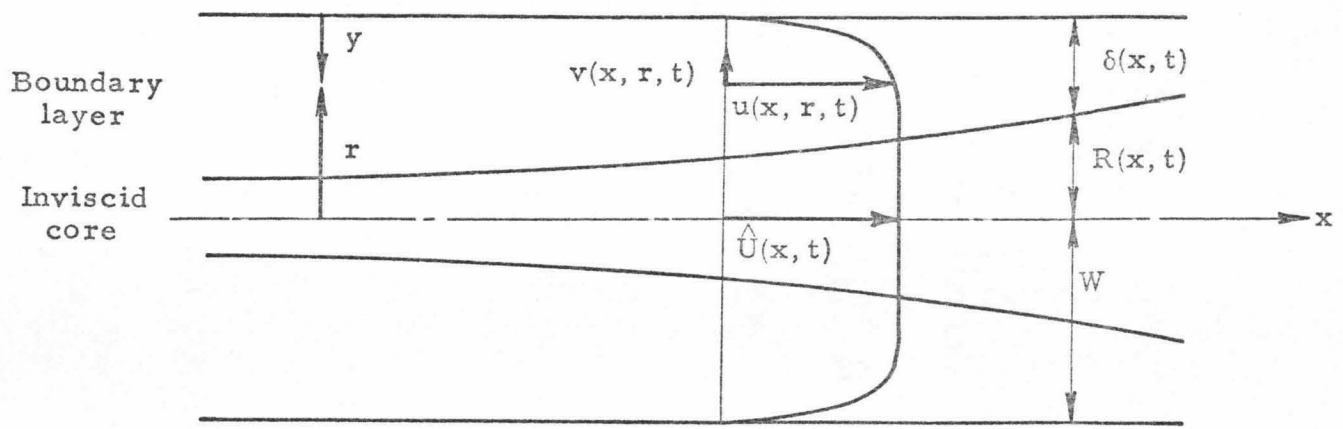

Fig. 2 Sketch of the Far-Field Inviscid Core and the Boundary Layer

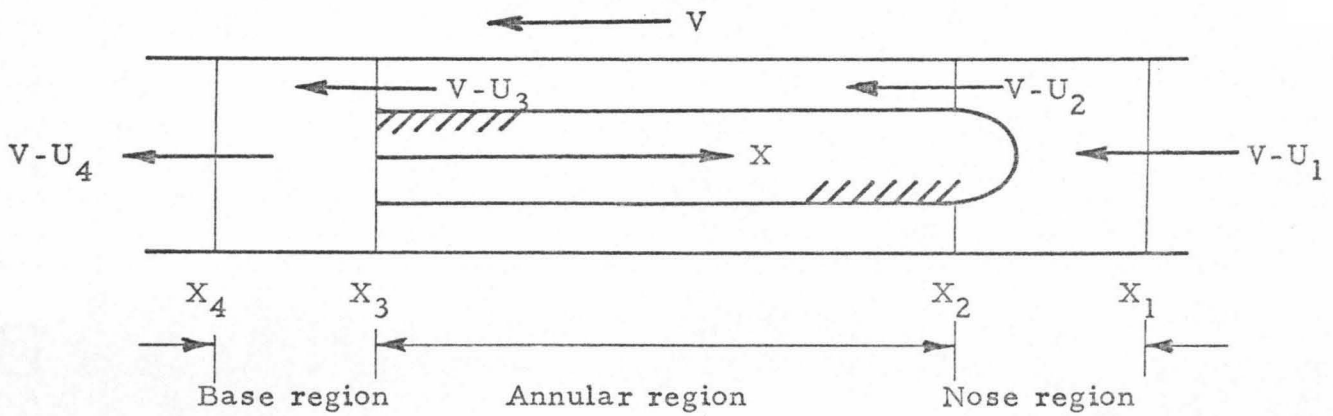

Fig. 3 Sketch of the Near-Field Flow in Vehicle Fixed Coordinates

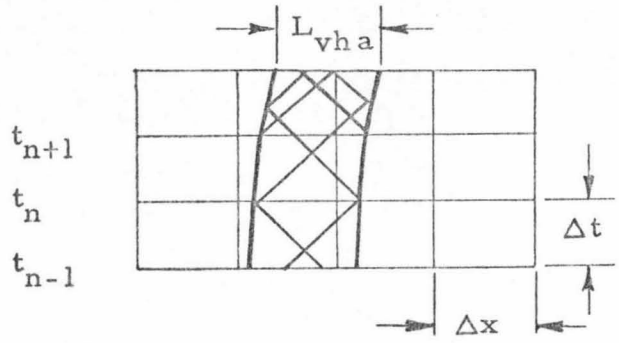

Fig. 4a

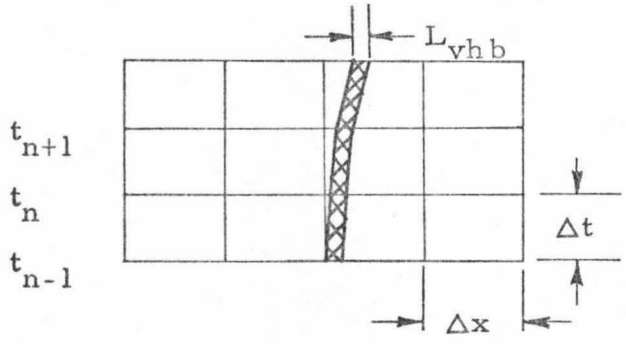

Fig. 4b

Fig. 4 Sketch of the Effect of the Vehicle Length on the Quasi-Steady Near-Field Assumption

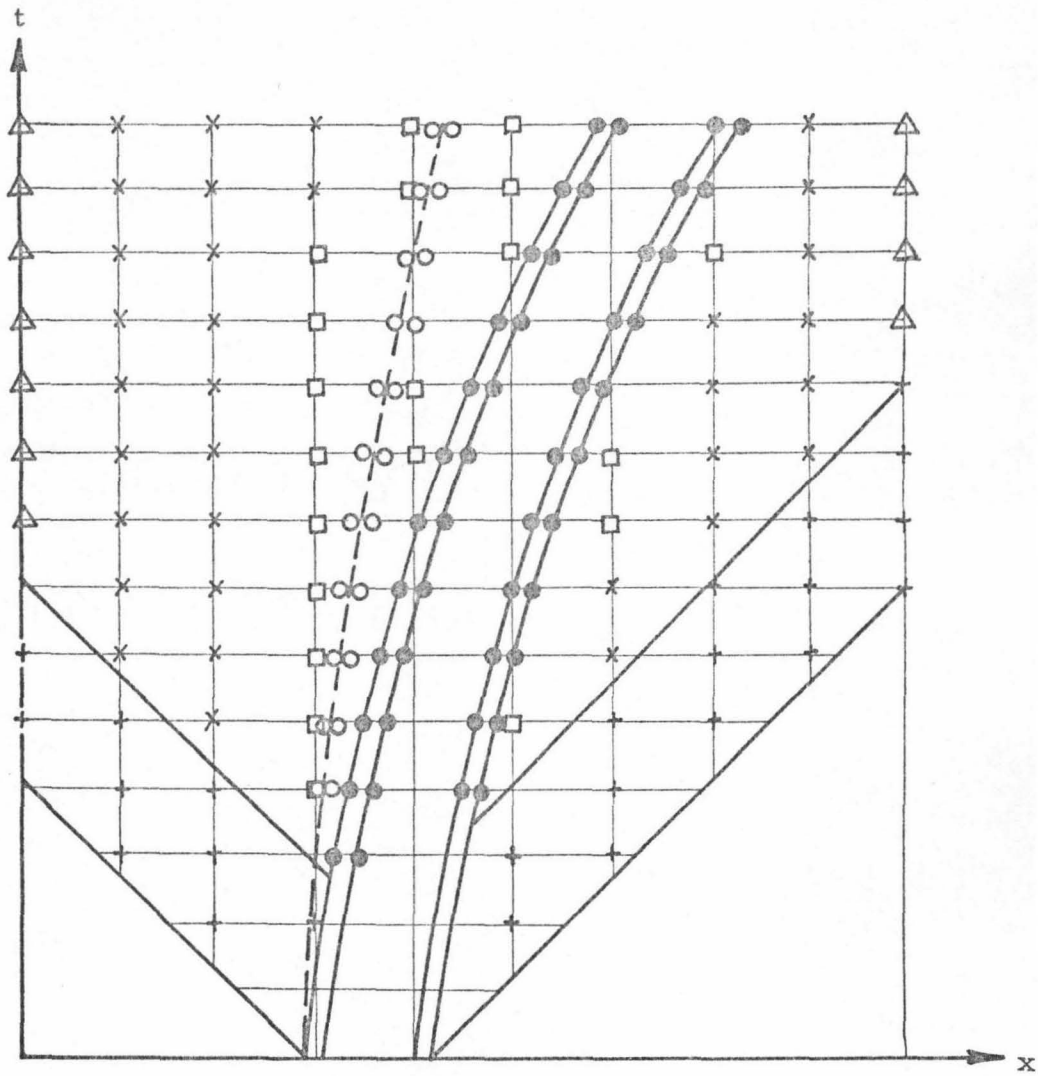

Fig. 5 Methods of Solution

\+ Linearized solution

□ Solution by characteristics

x Lax-Wendroff method

△ Boundary conditions and characteristic equations

● Near-field equations and characteristic equations

o Contact surface relations and characteristic equations

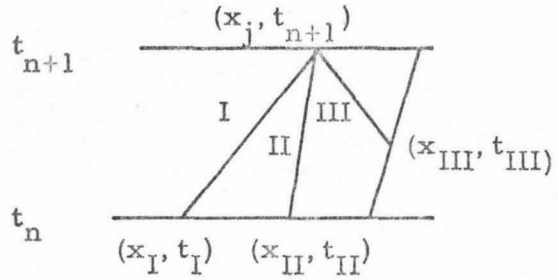

Fig. 6a

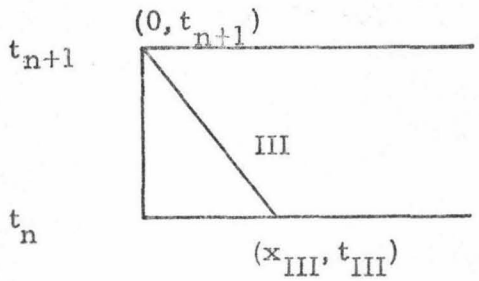

Fig. 6b

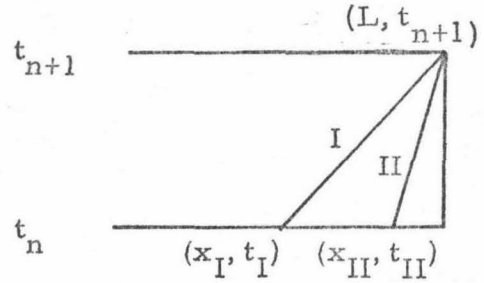

Fig. 6c

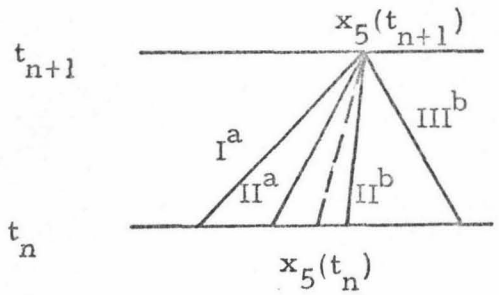

Fig. 6d

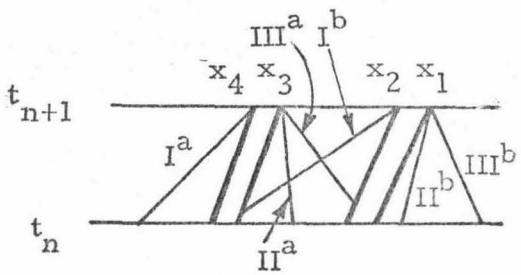

Fig. 6e

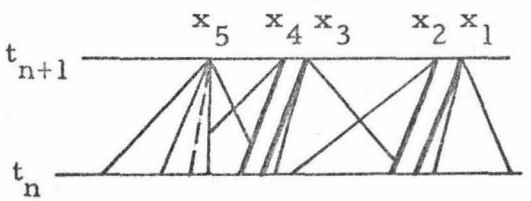

Fig. 6f

Fig. 6 The Characteristic Curves

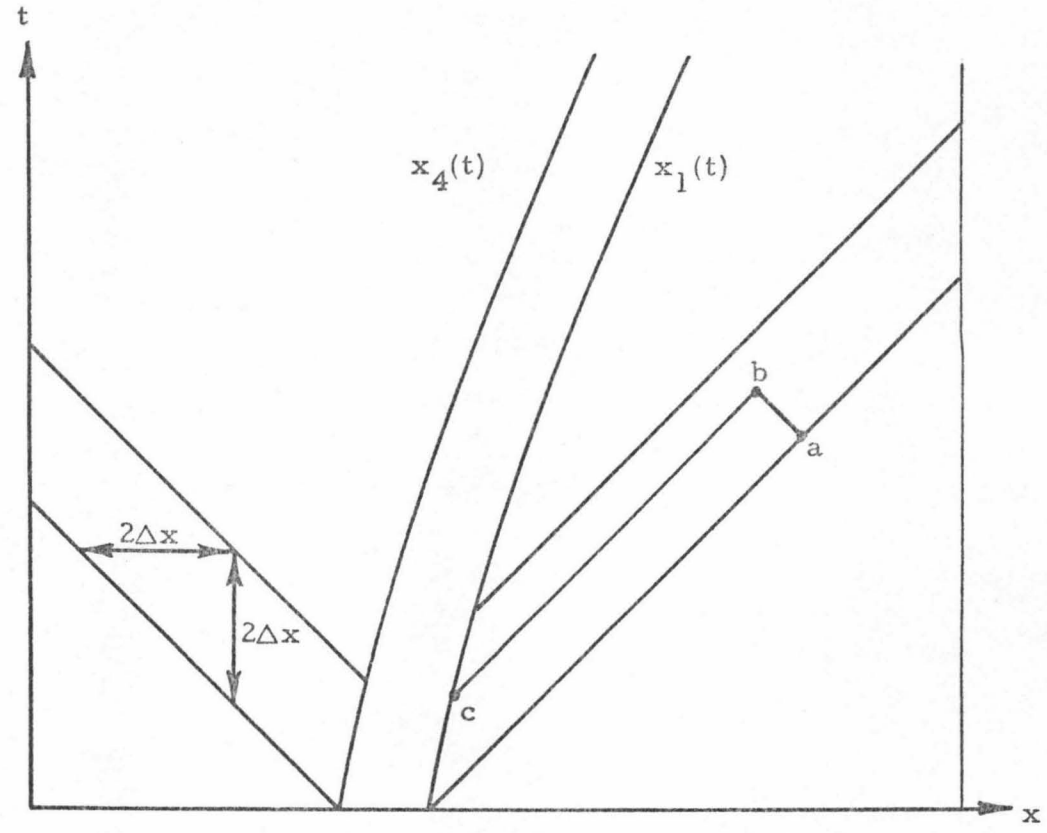

Fig. 7 The Initial Wave Region

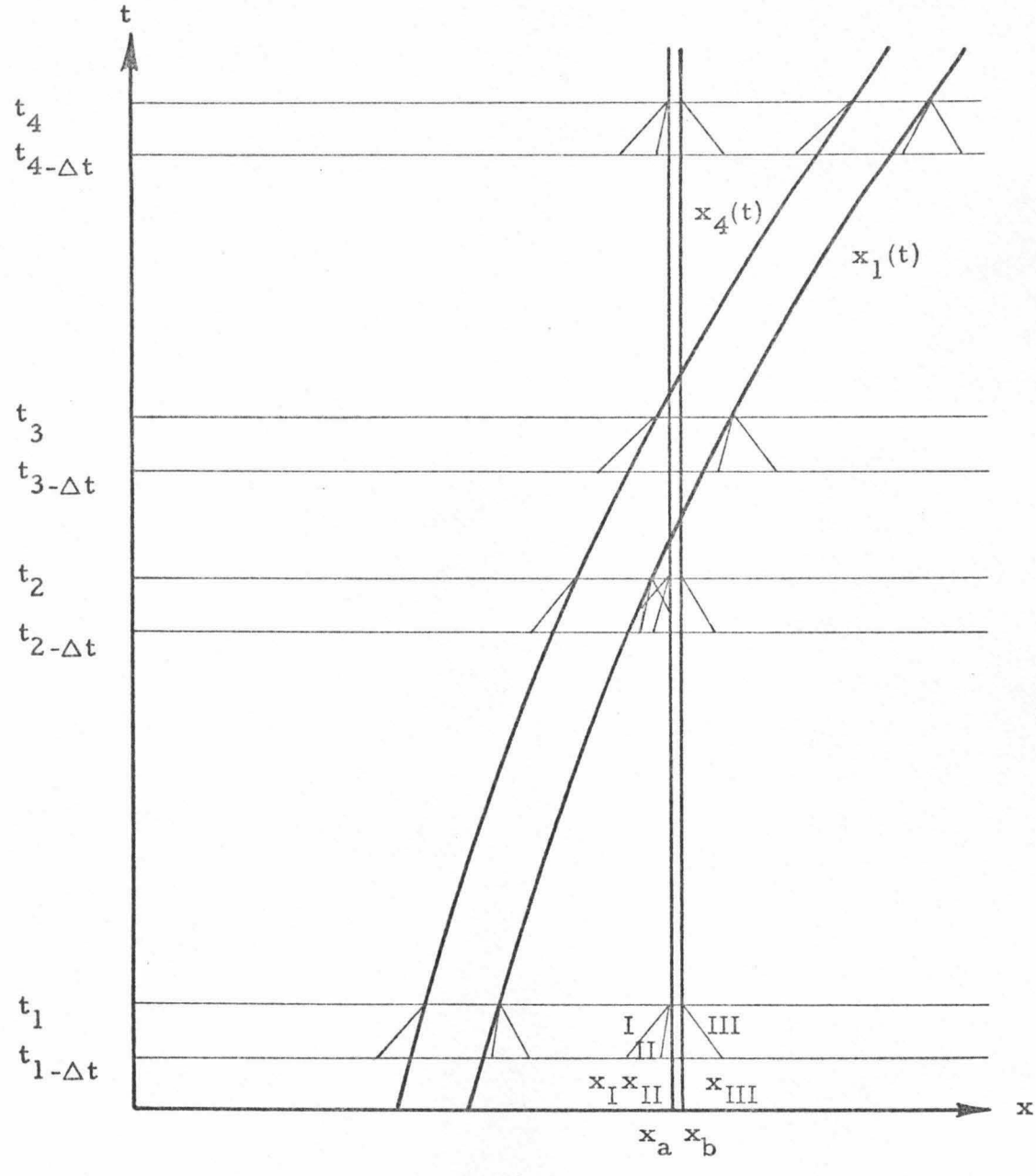

Fig. 8 x-t Diagram for a Vehicle Travelling in a Vented Tube

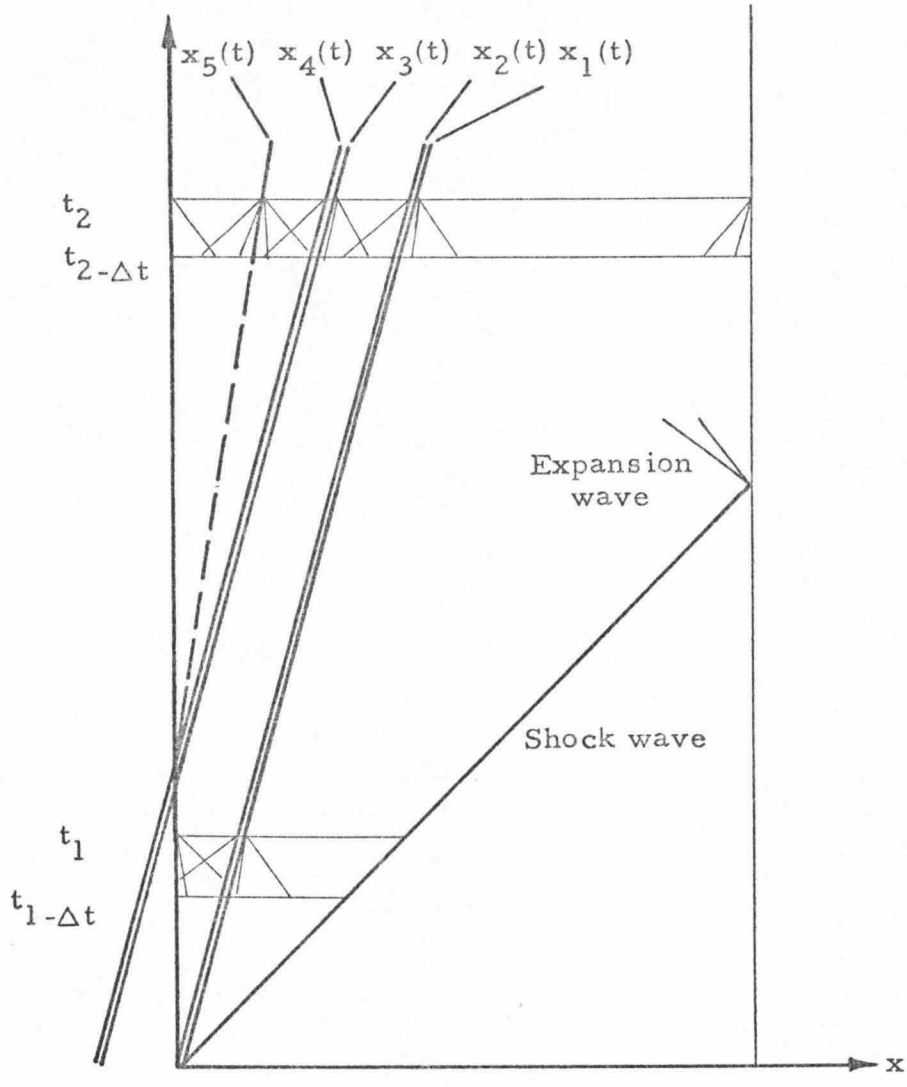

Fig. 9a x-t Diagram for a Vehicle Entering a Tube

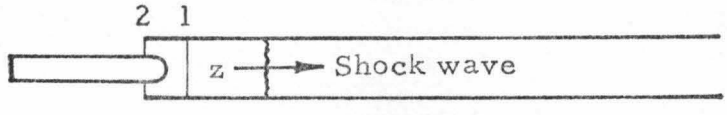

Fig. 9b The Position for Determining the Initial Shock Wave Strength

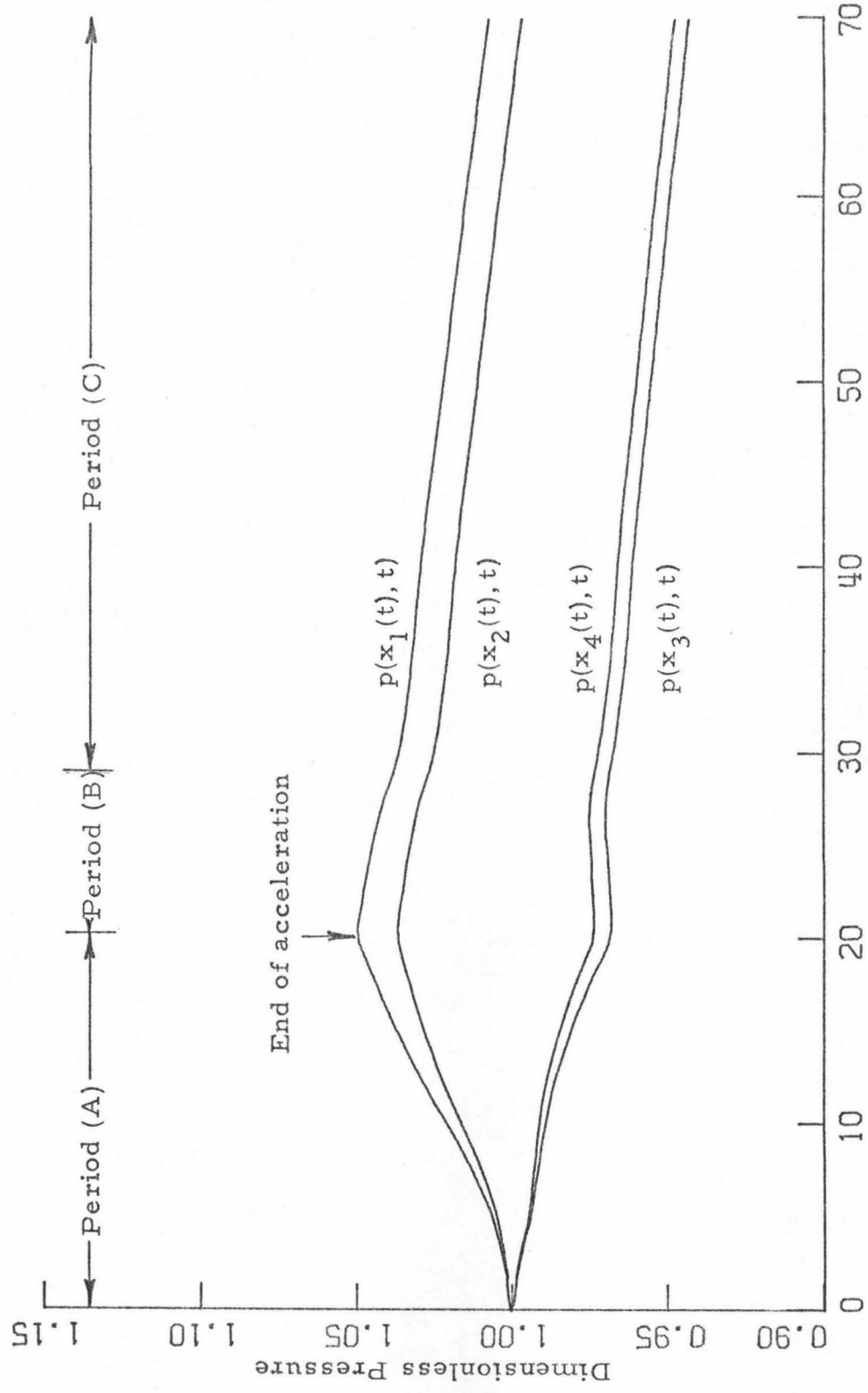

Fig. 10 The Pressure Variation with Time

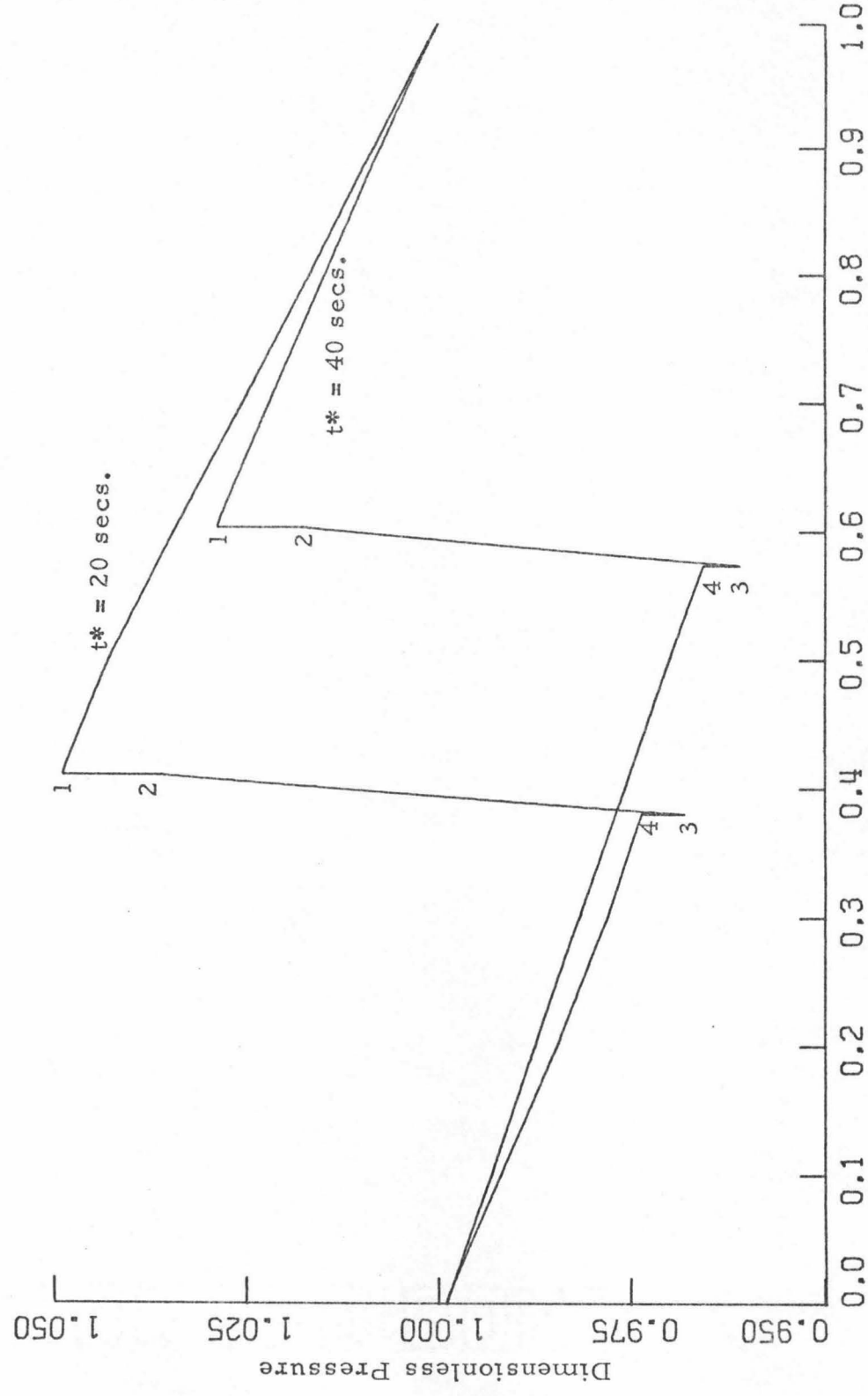

Fig. 11 The Pressure Variation along the Tube

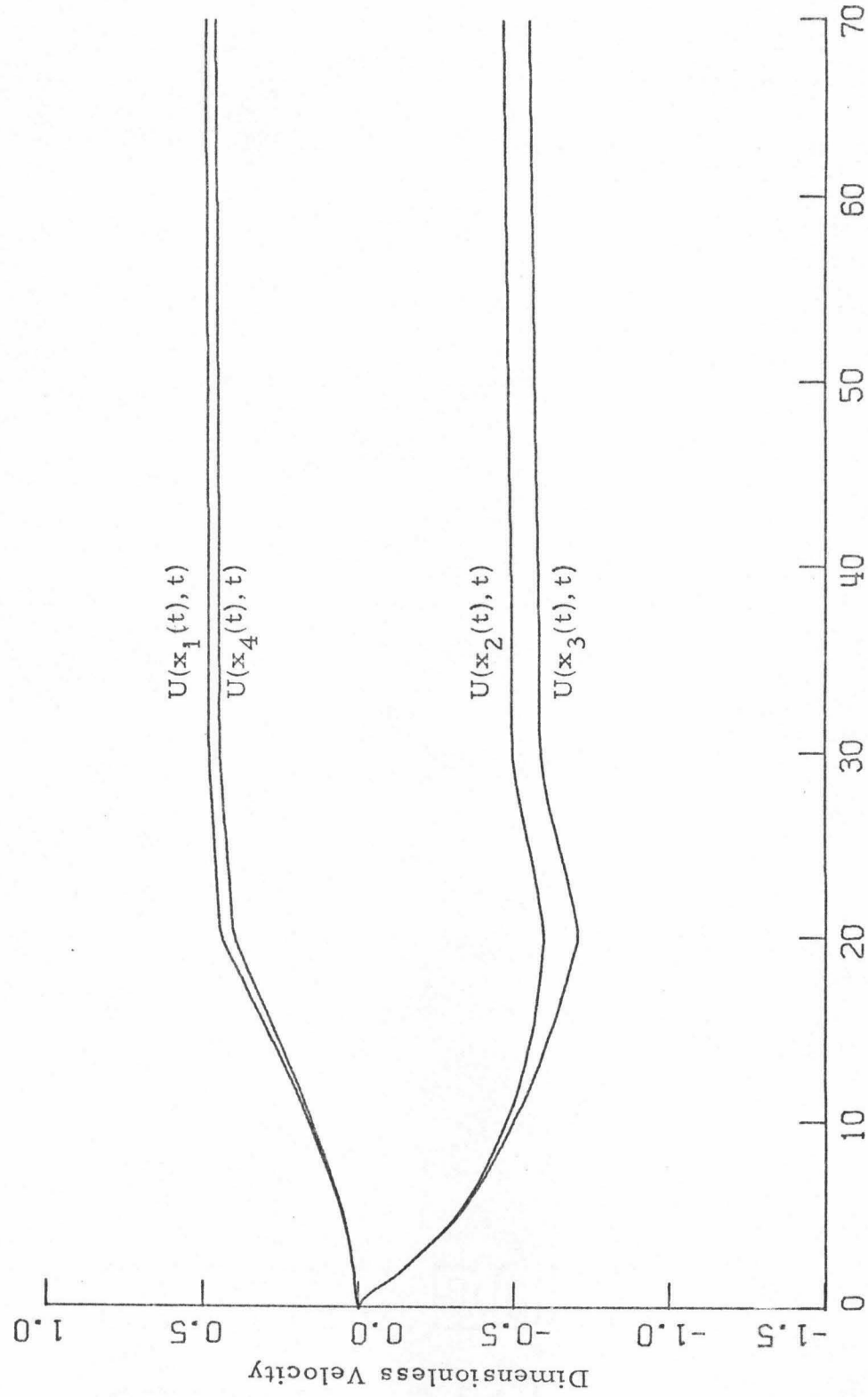

Fig. 12 The Flow Velocity Variation with Time

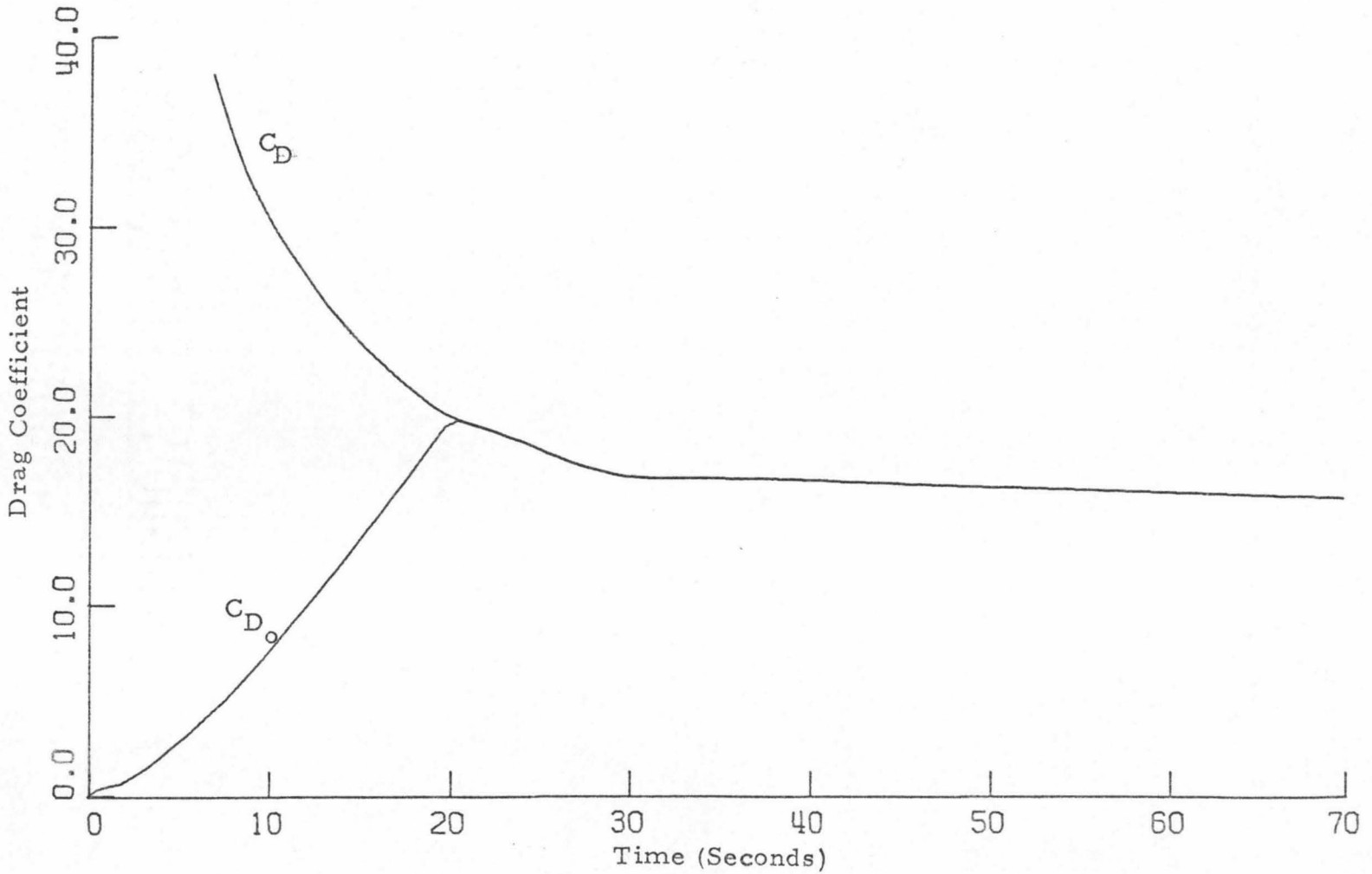

Fig. 13 The Drag Coefficient Variation with Time

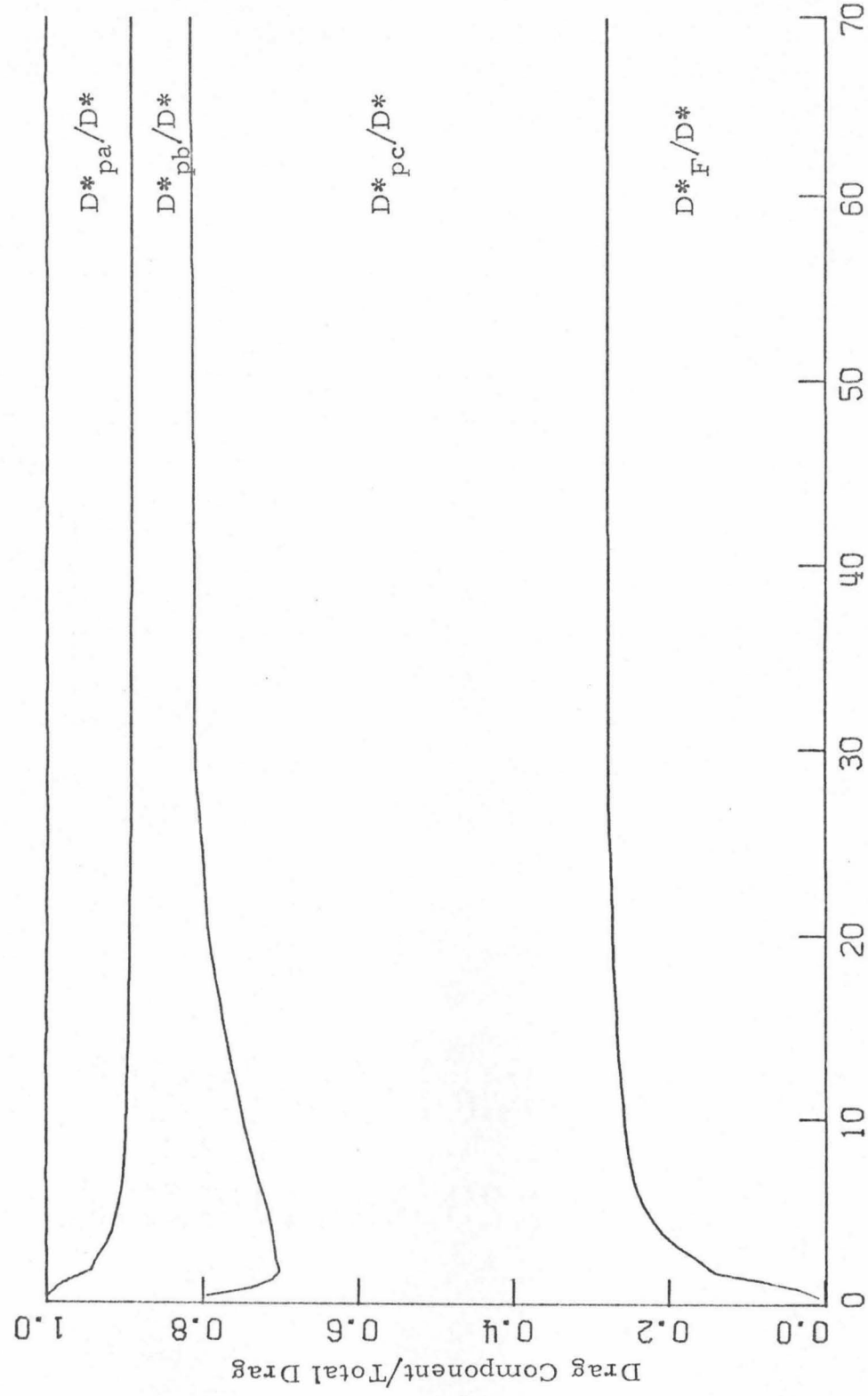

Fig. 14 The Drag Components

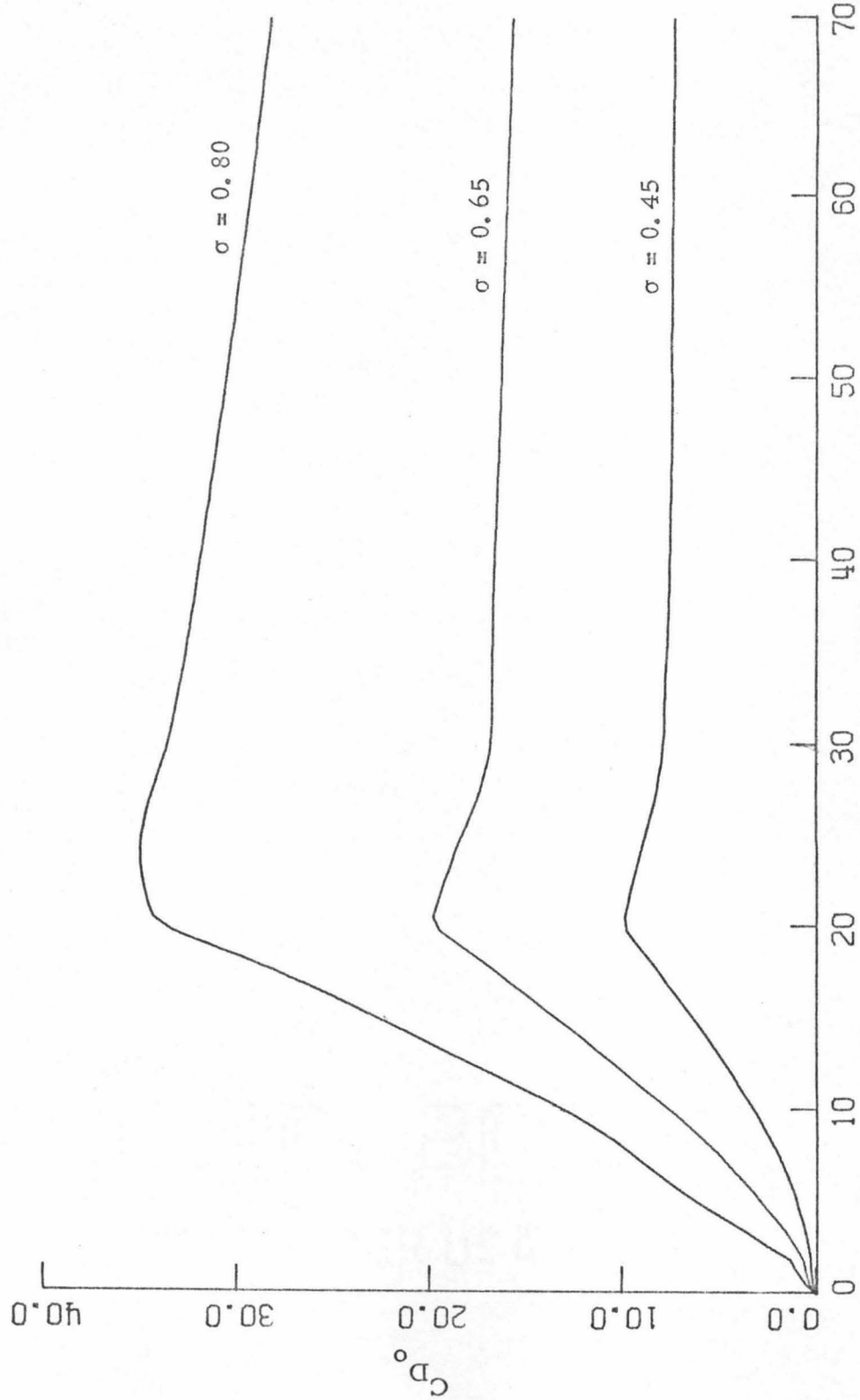

Fig. 15 The Effect of the Blockage Ratio on the Drag Coefficient

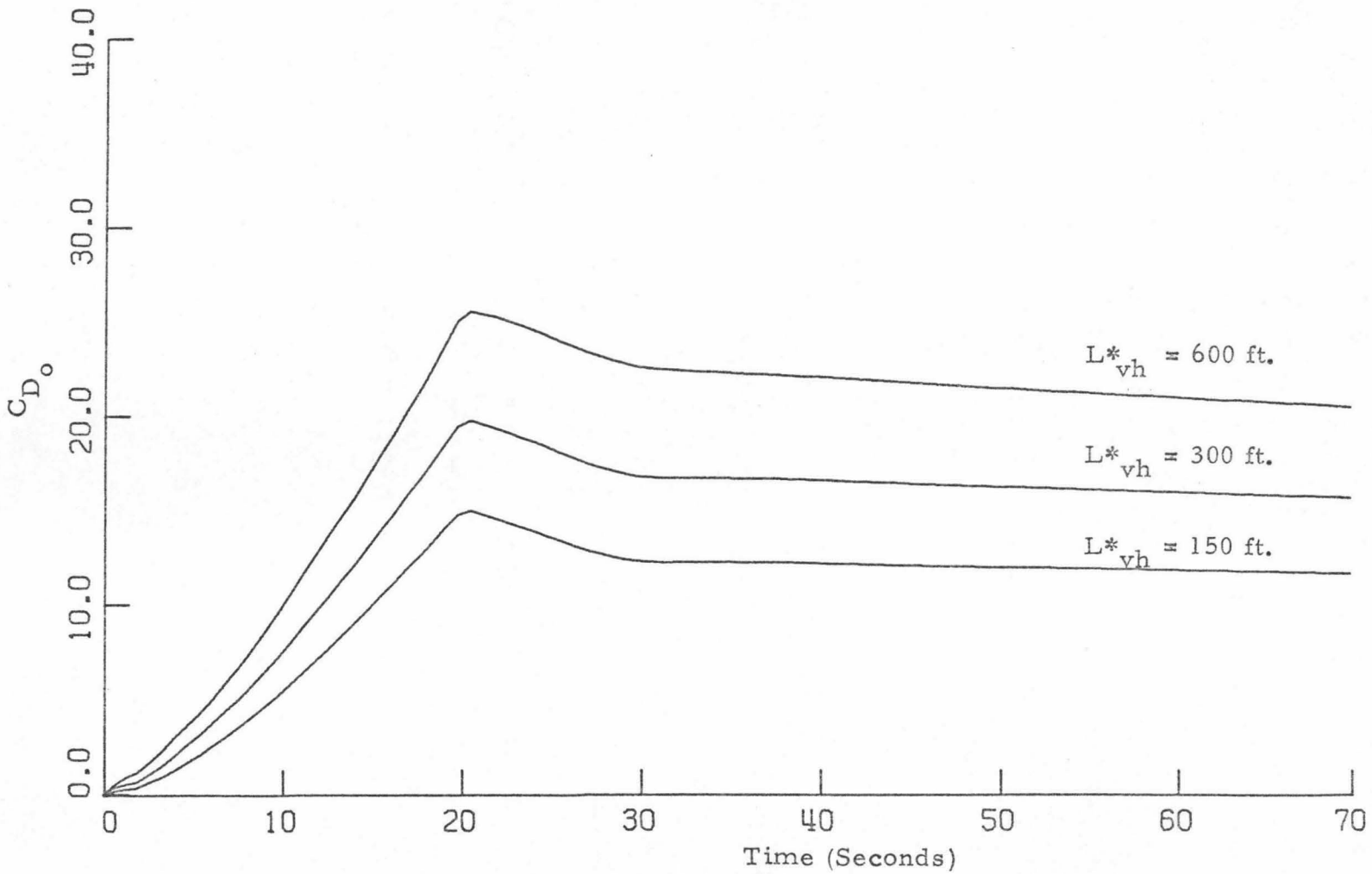

Fig. 16 The Effect of the Vehicle Length on the Drag Coefficient

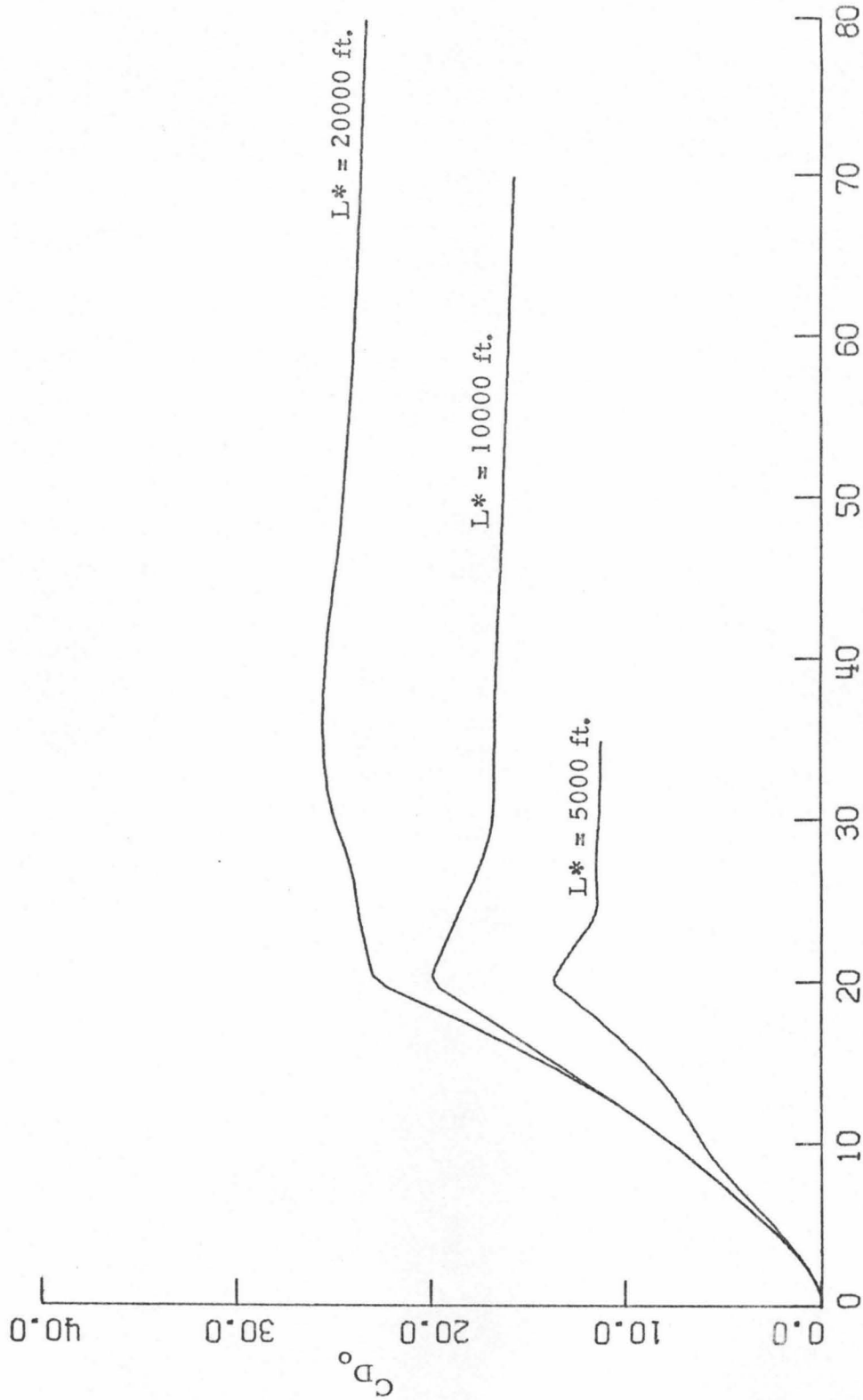

Fig. 17 The Effect of the Tube Length on the Drag Coefficient

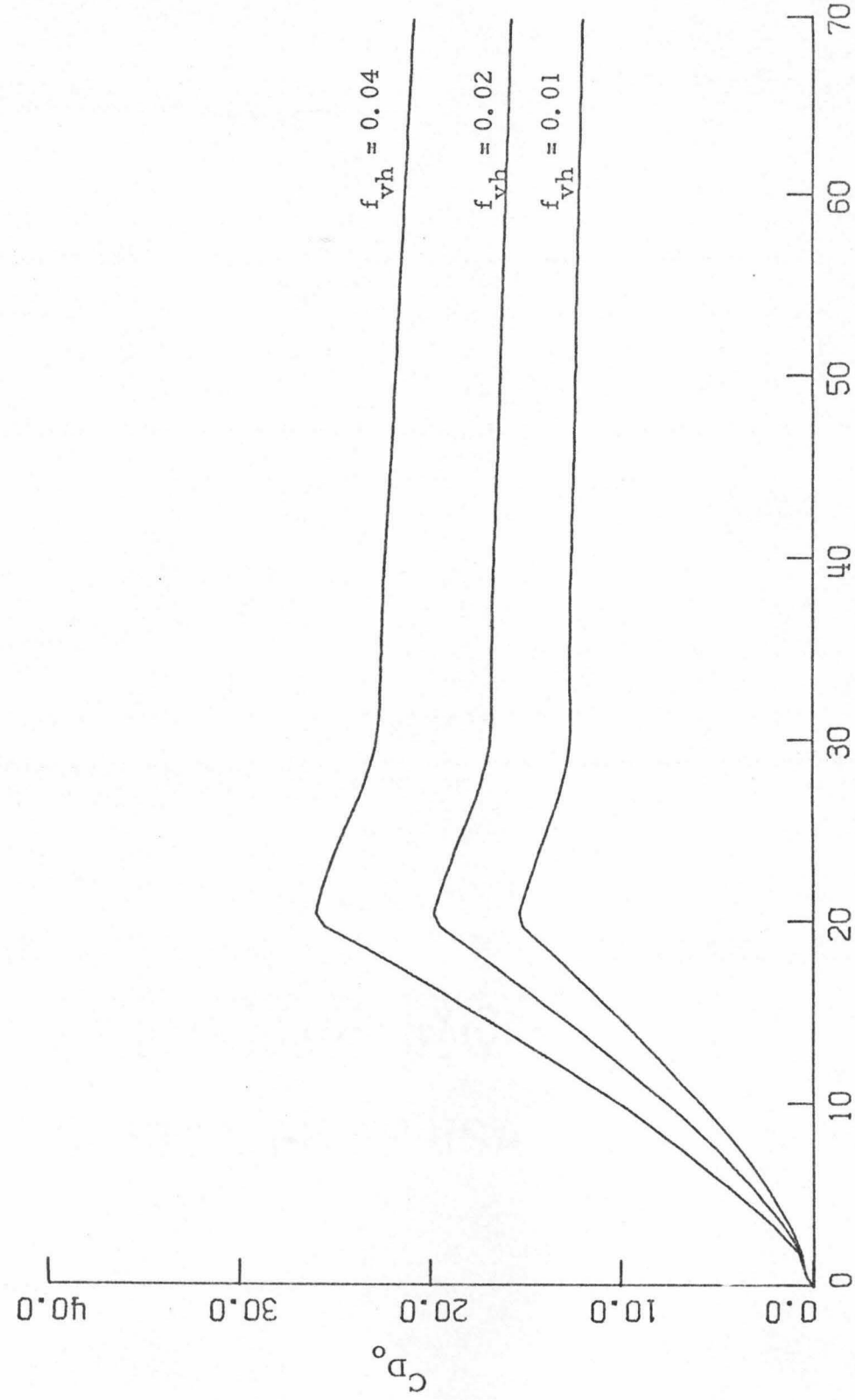

Fig. 18 The Effect of the Vehicle Skin Friction Factor on the Drag Coefficient

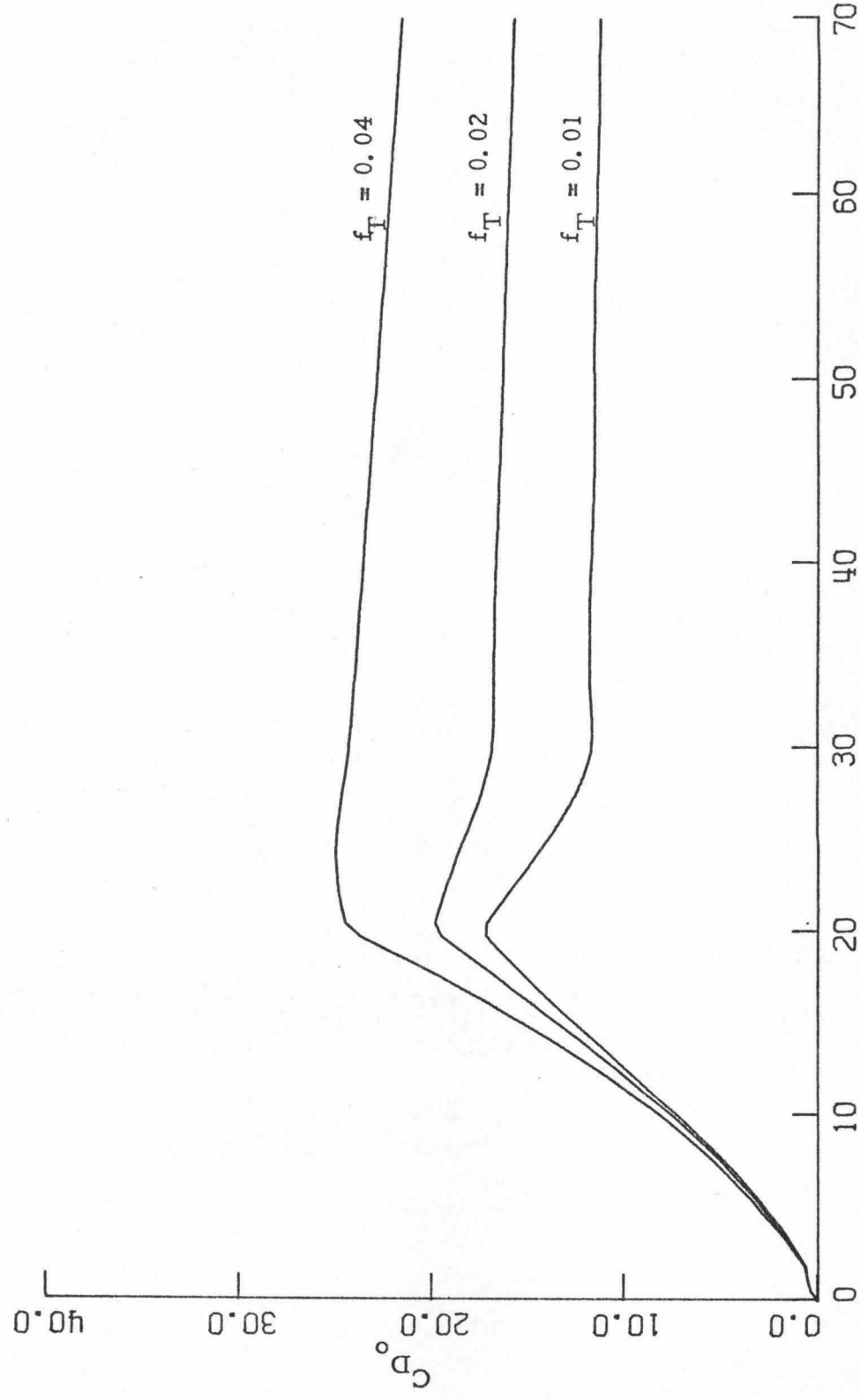

Fig. 19 The Effect of the Tube Skin Friction Factor on the Drag Coefficient

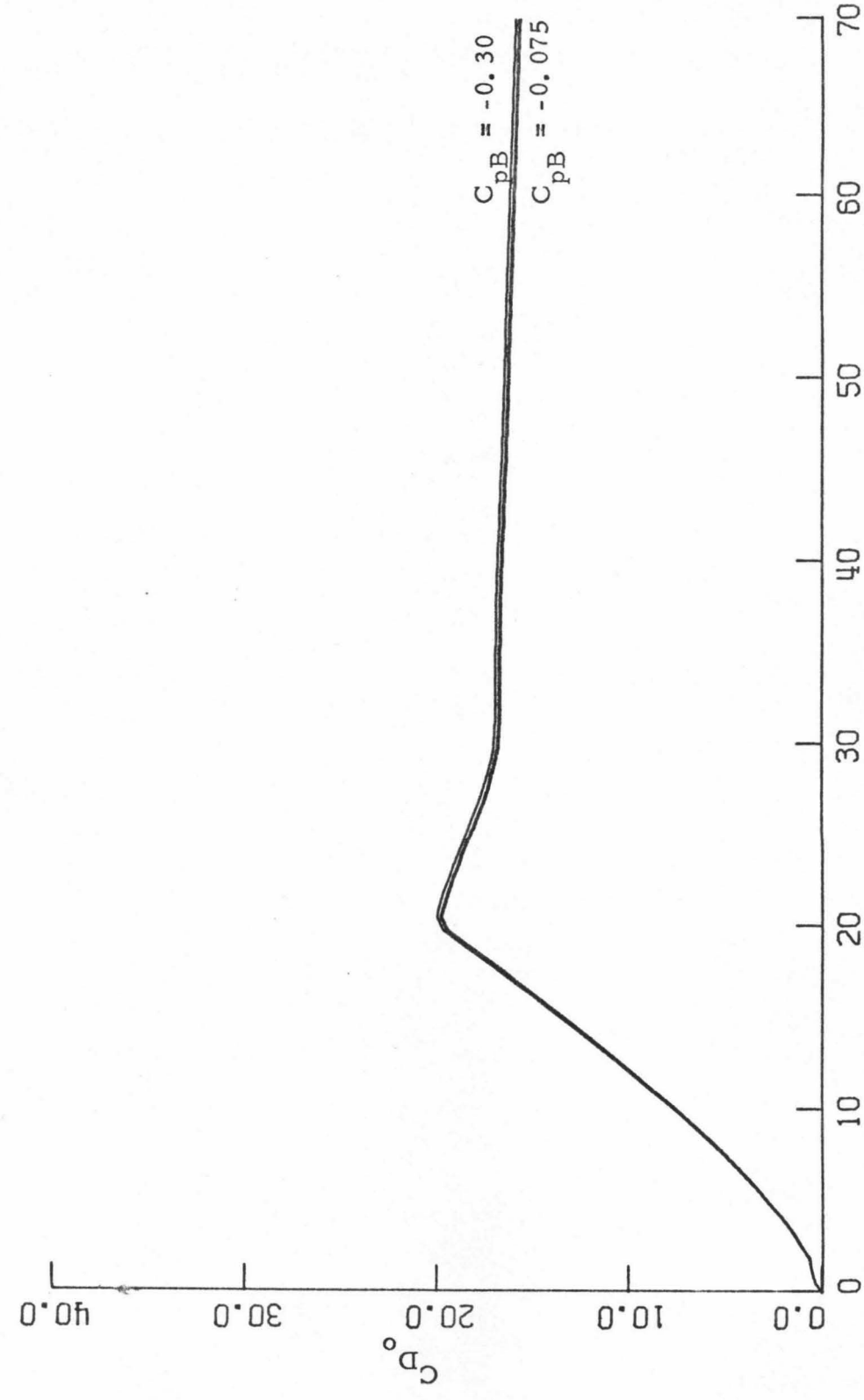

Fig. 20 The Effect of the Base Pressure Coefficient on the Drag Coefficient

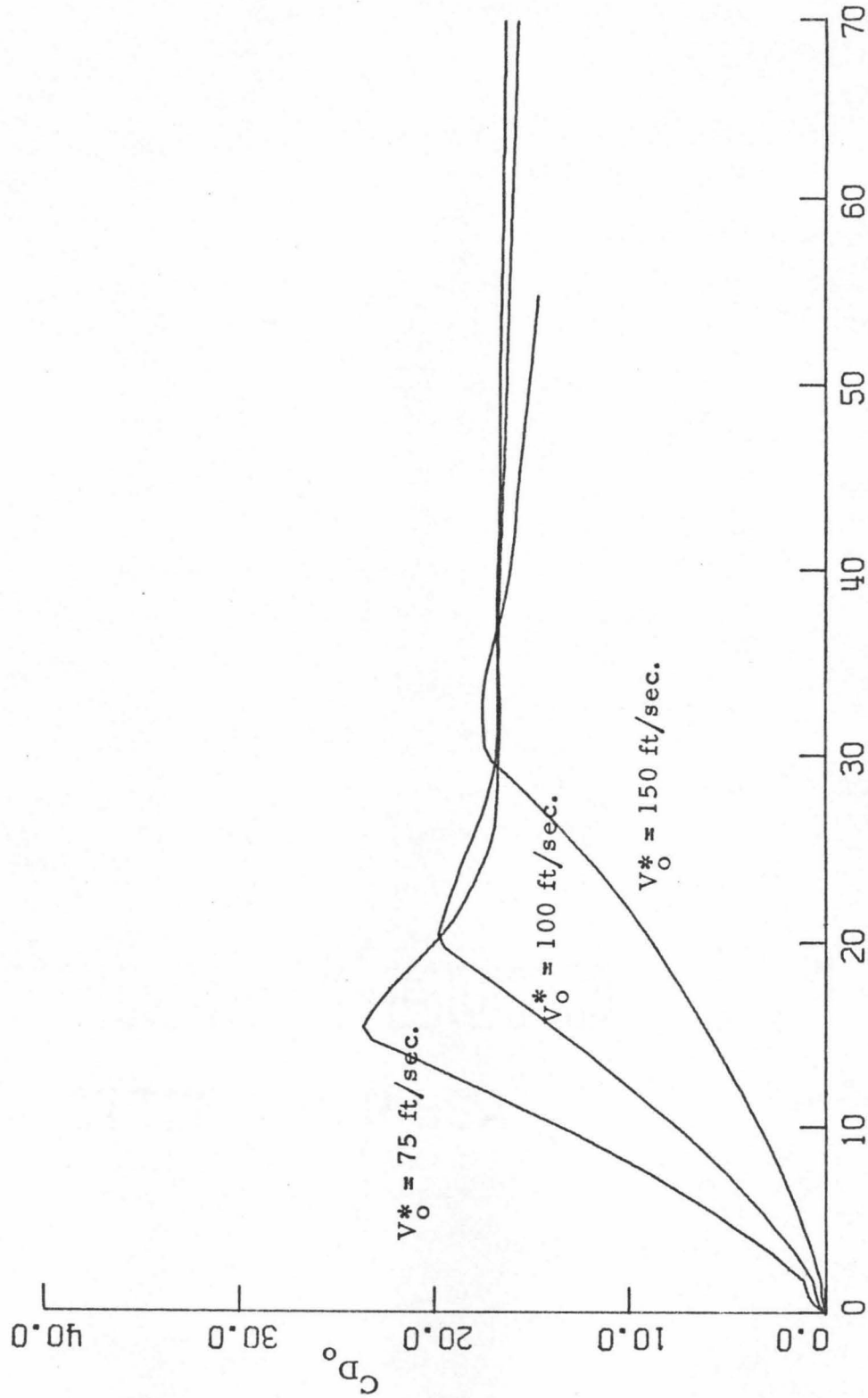

Fig. 21a The Effect of the Maximum Vehicle Velocity on the Drag Coefficient

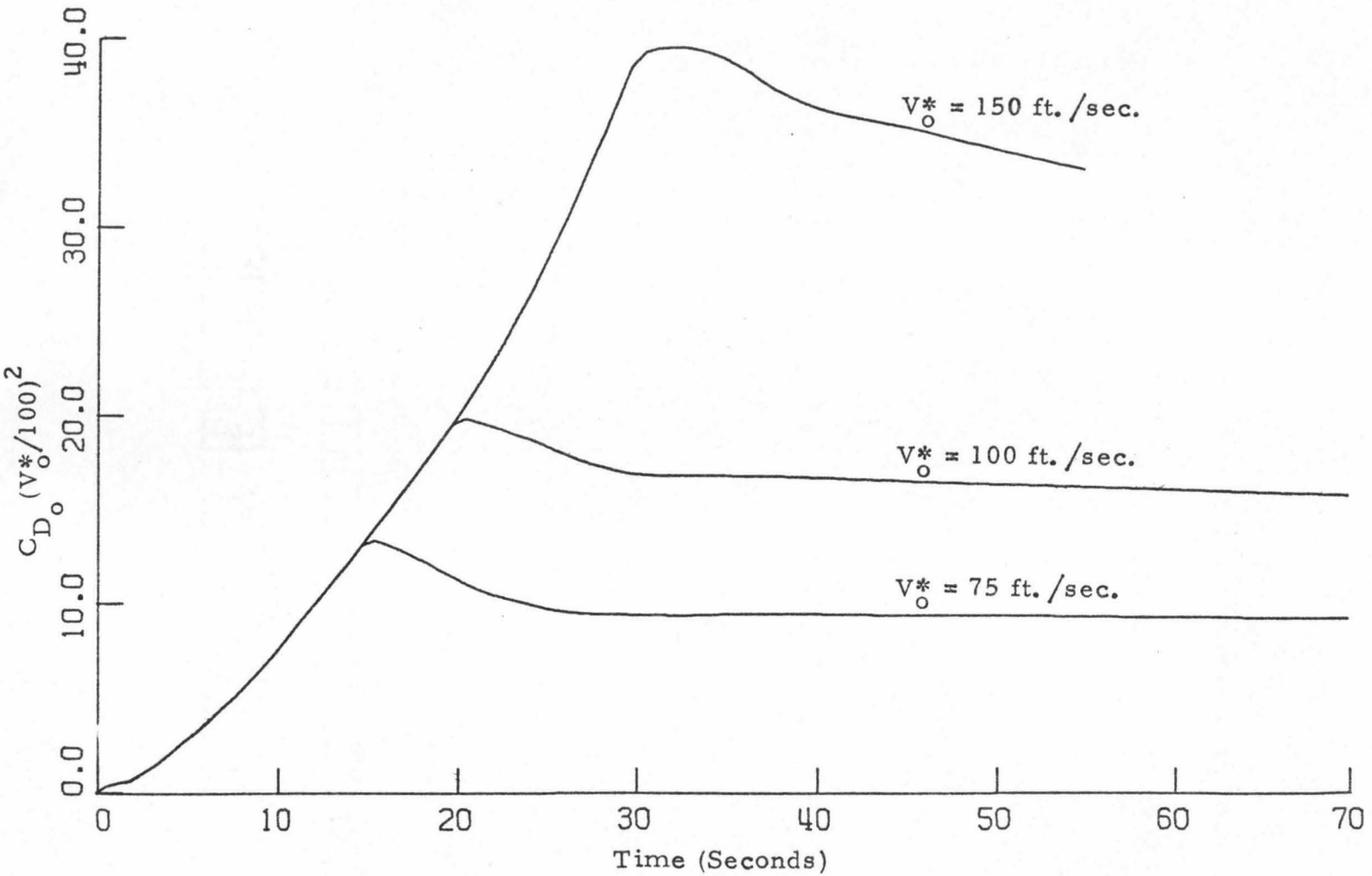

Fig. 21b The Effect of the Maximum Vehicle Velocity on the Modified Drag Coefficient

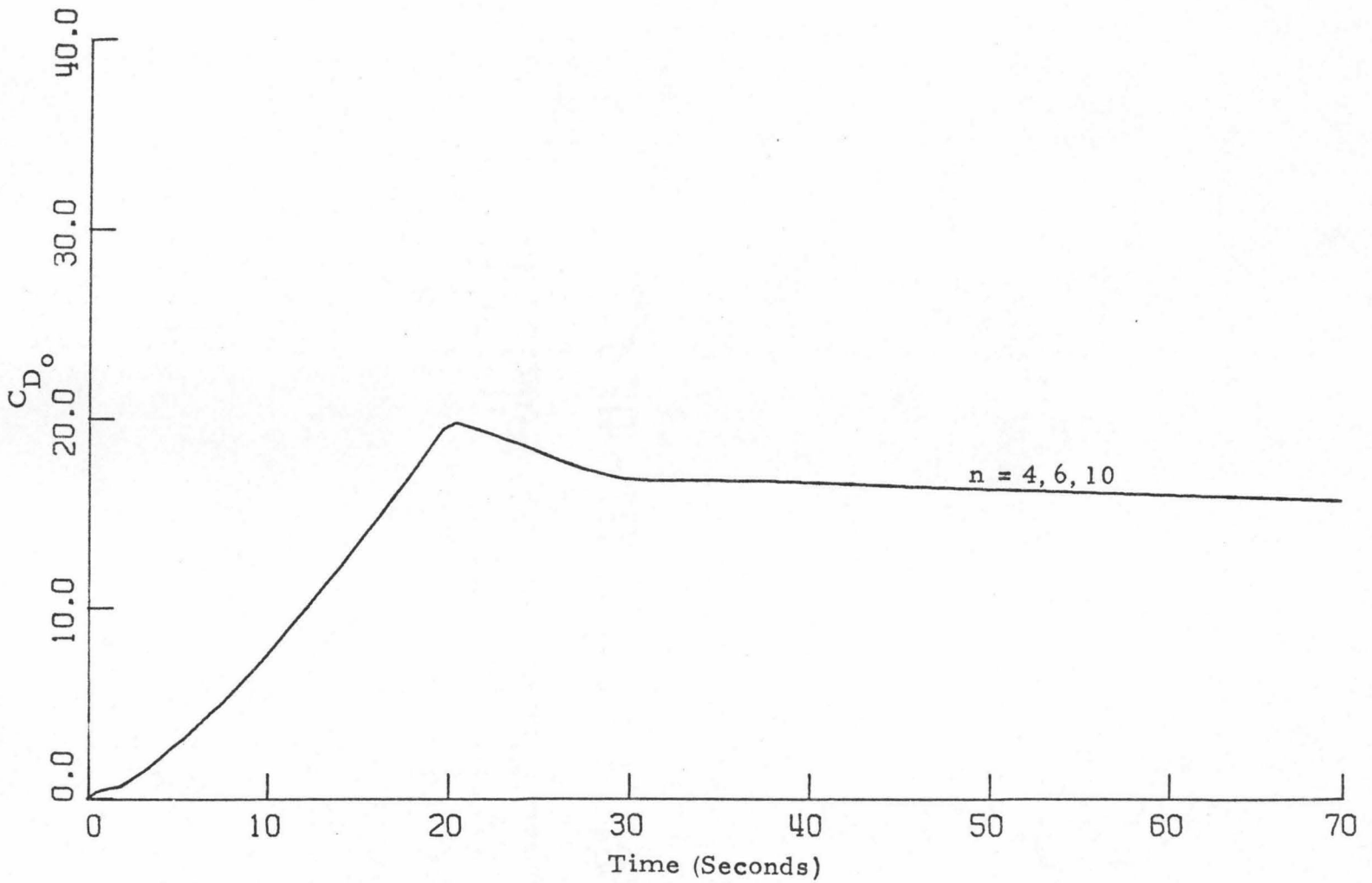

Fig. 22 The Effect of the Far-Field Velocity Profile on the Drag Coefficient

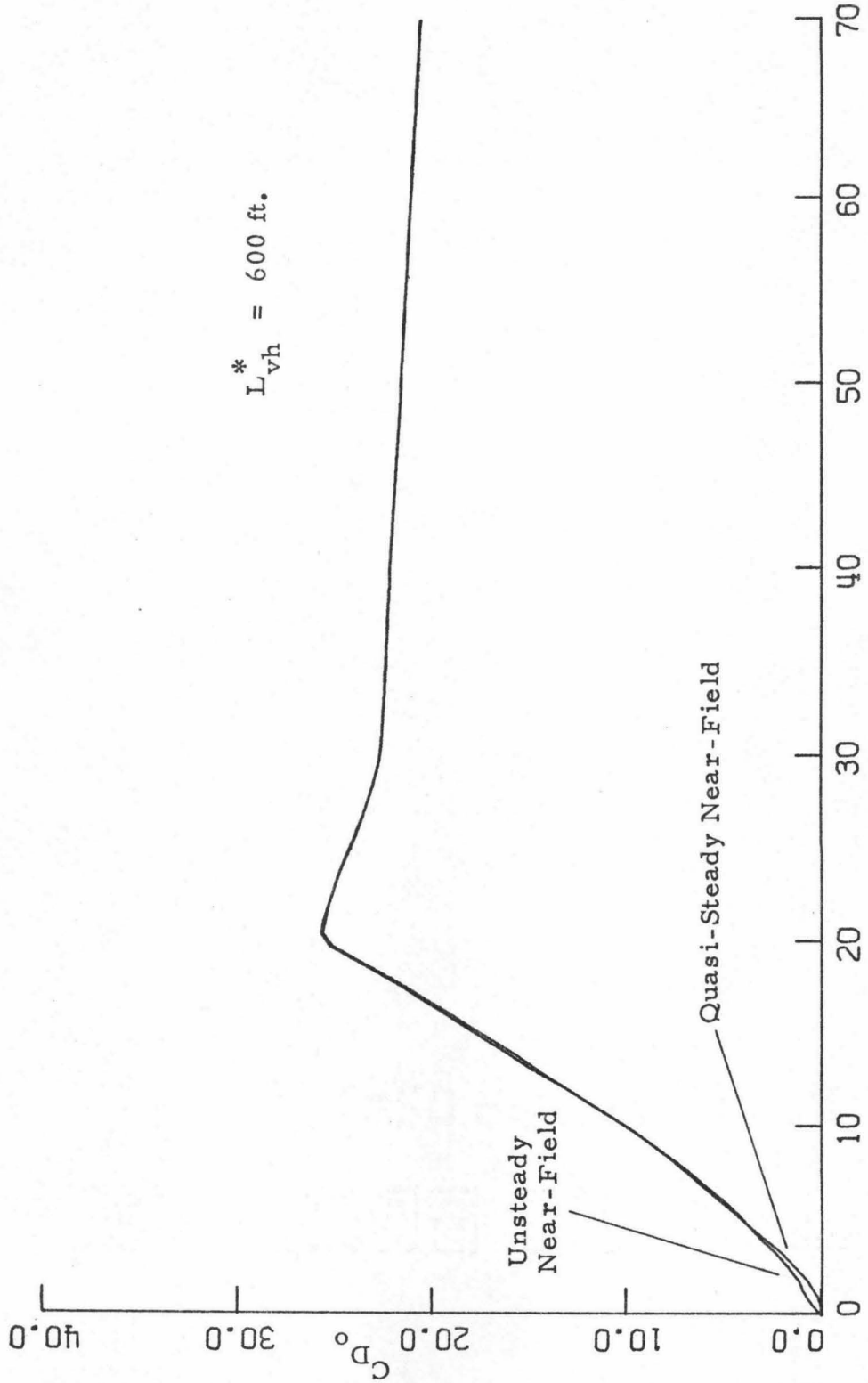

Fig. 23 The Effect of the Quasi-Steady Near-Field Assumption on the Solution

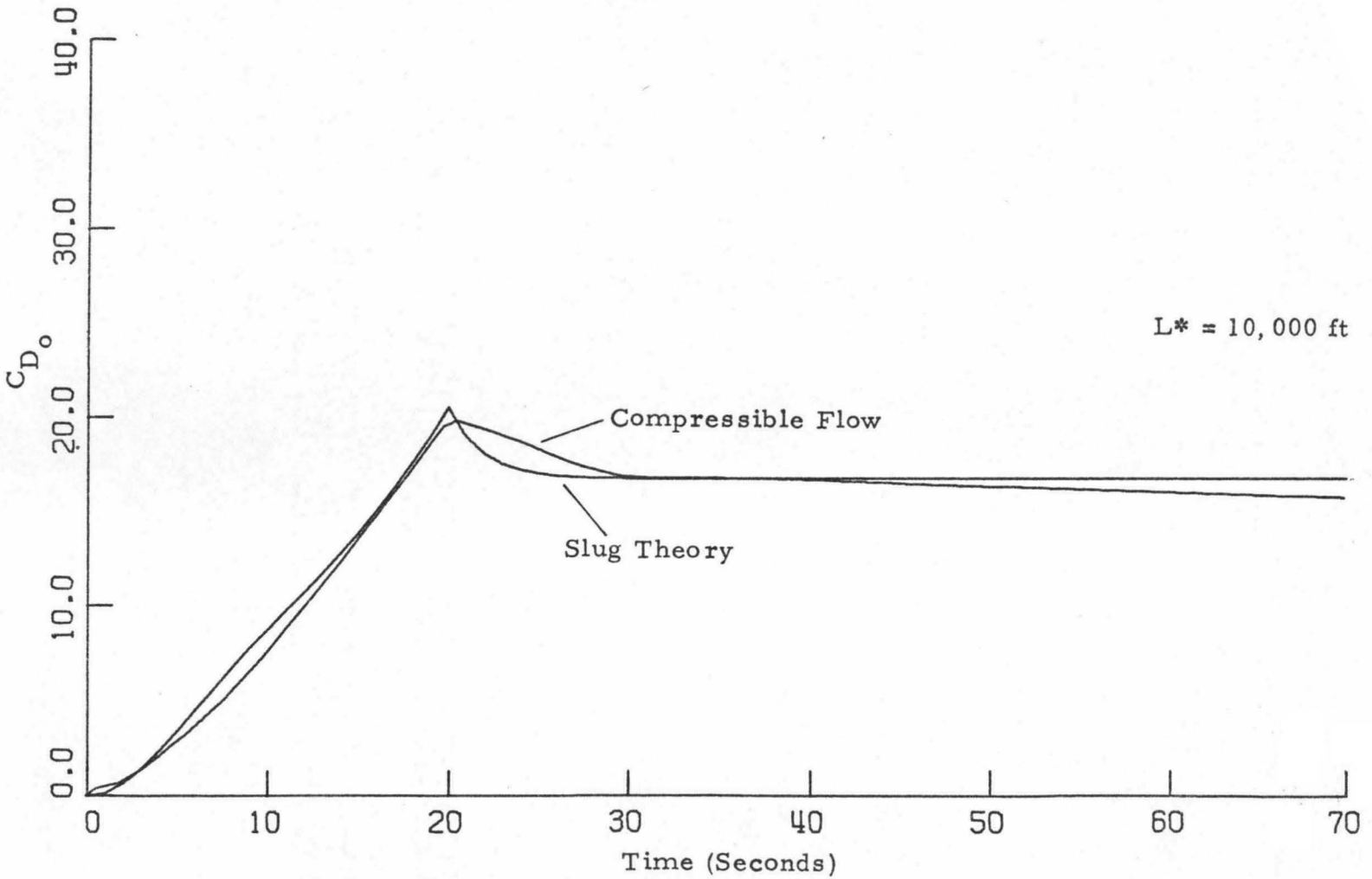

Fig. 24a Comparison of the Solution to the Slug Theory

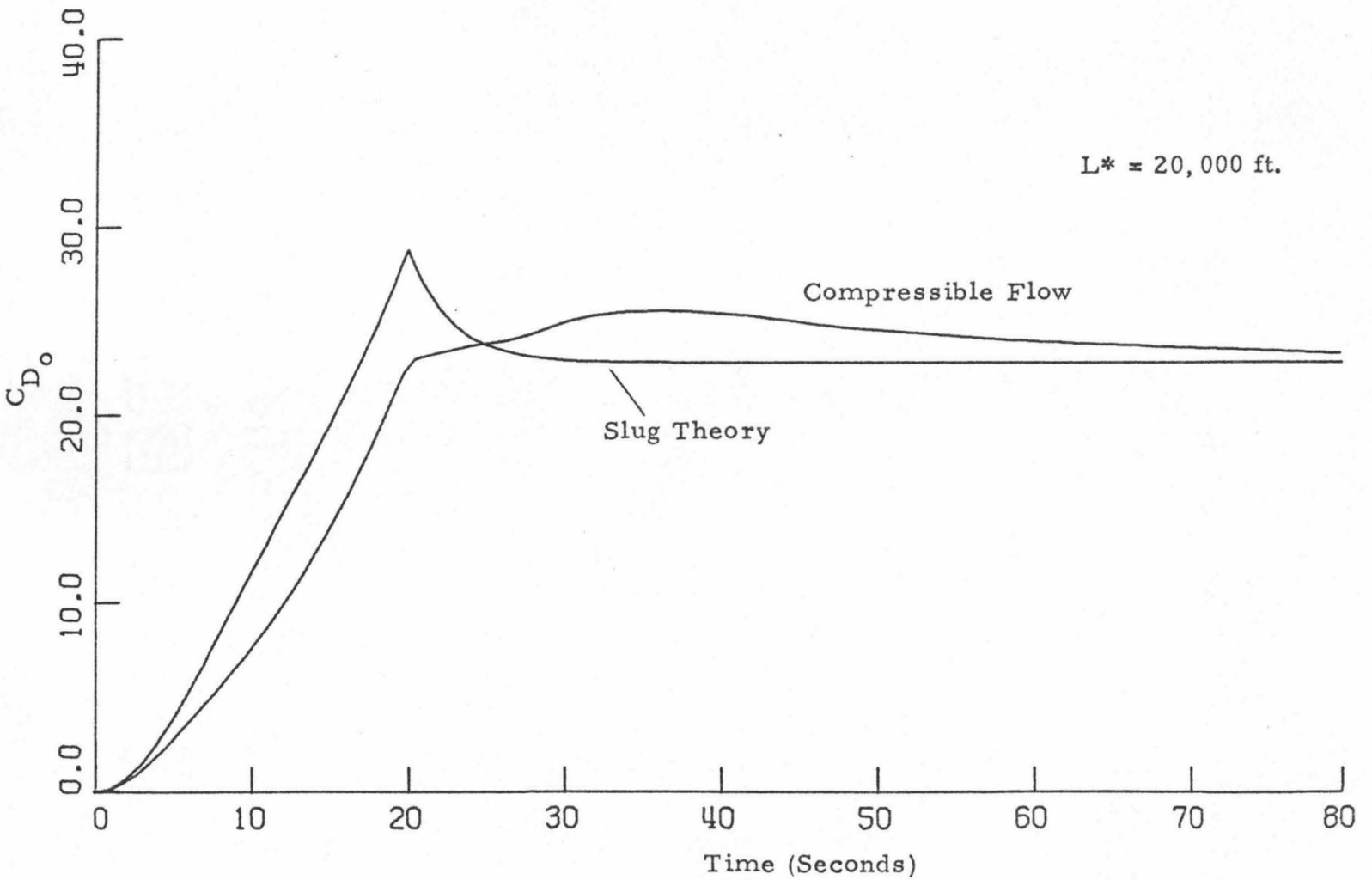

Fig. 24b Comparison of the Solution to the Slug Theory

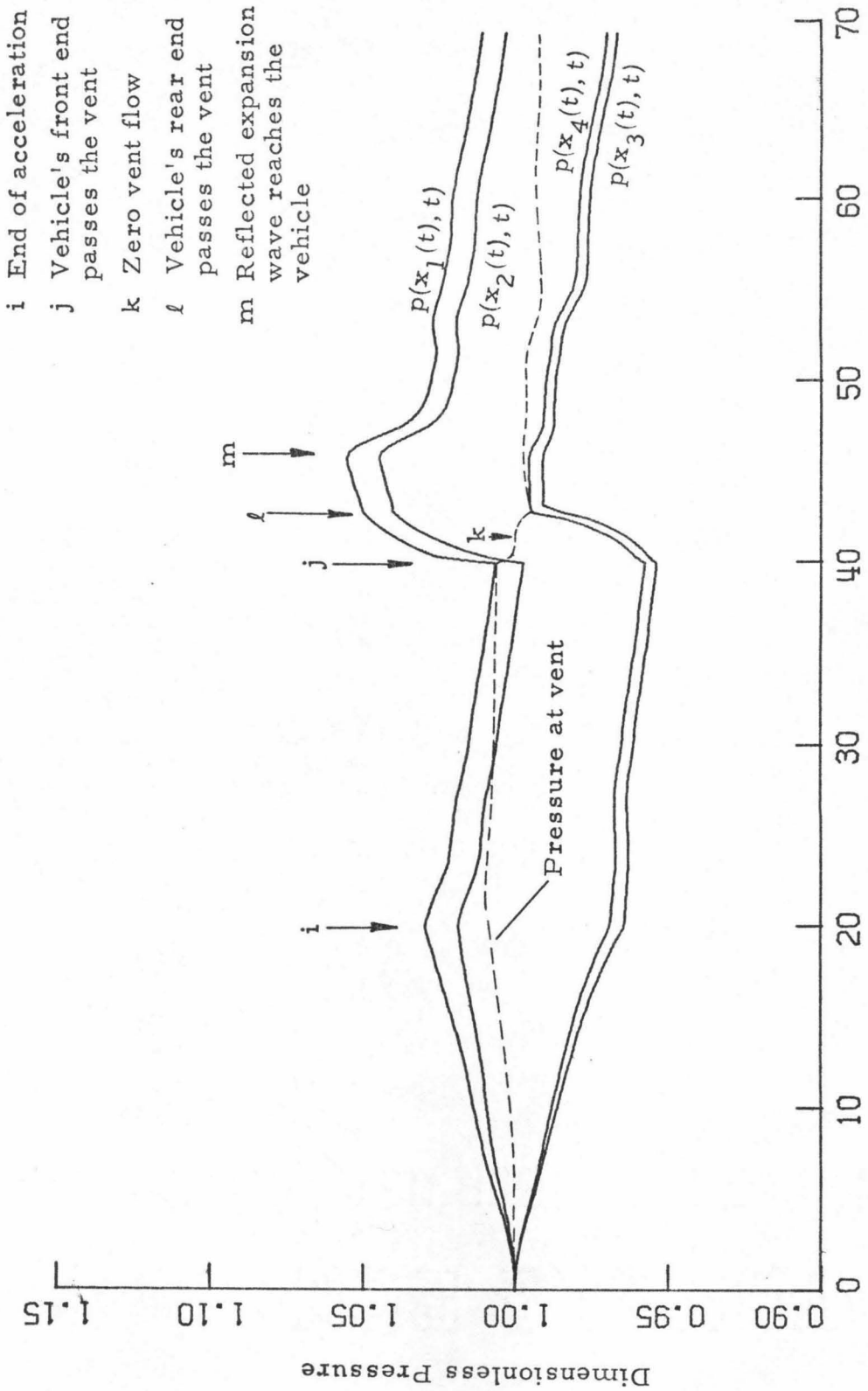

Fig. 25 The Pressure Variation with Time for the Case of a Vented Tube

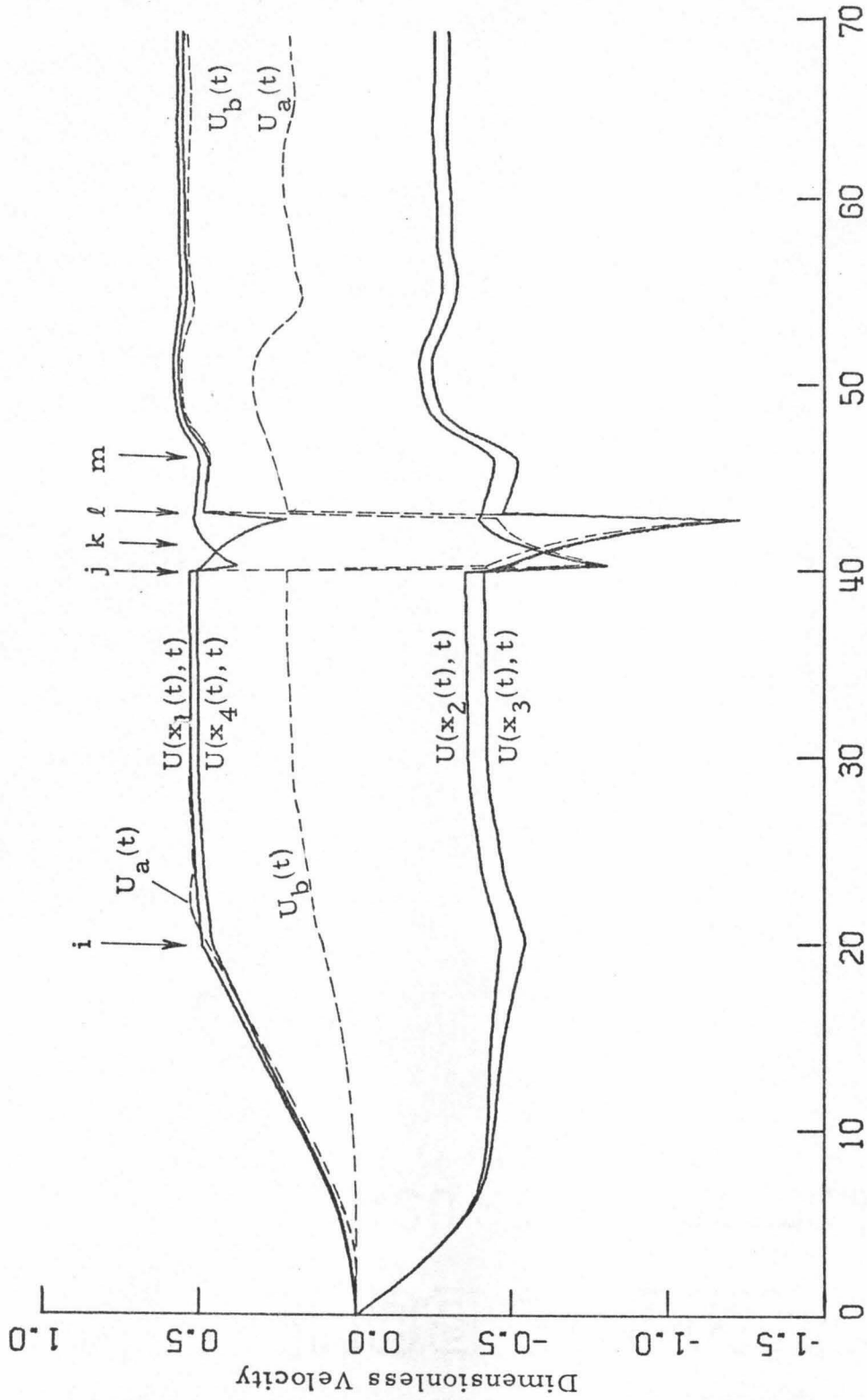

Fig. 26 The Flow Velocity Variation with Time for the Case of a Vented Tube

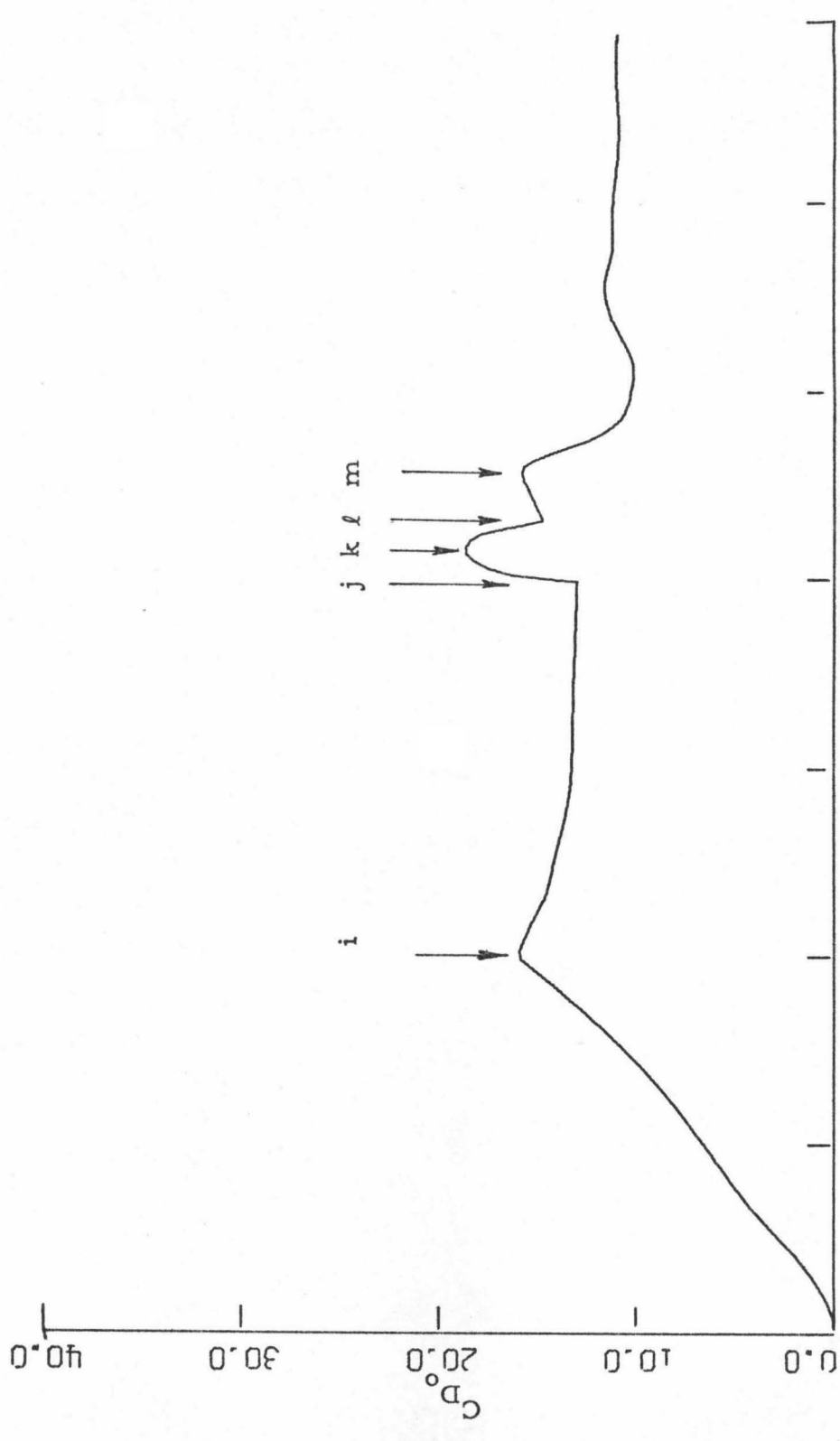

Fig. 27 The Drag Coefficient Variation with Time for the Case of a Vented Tube

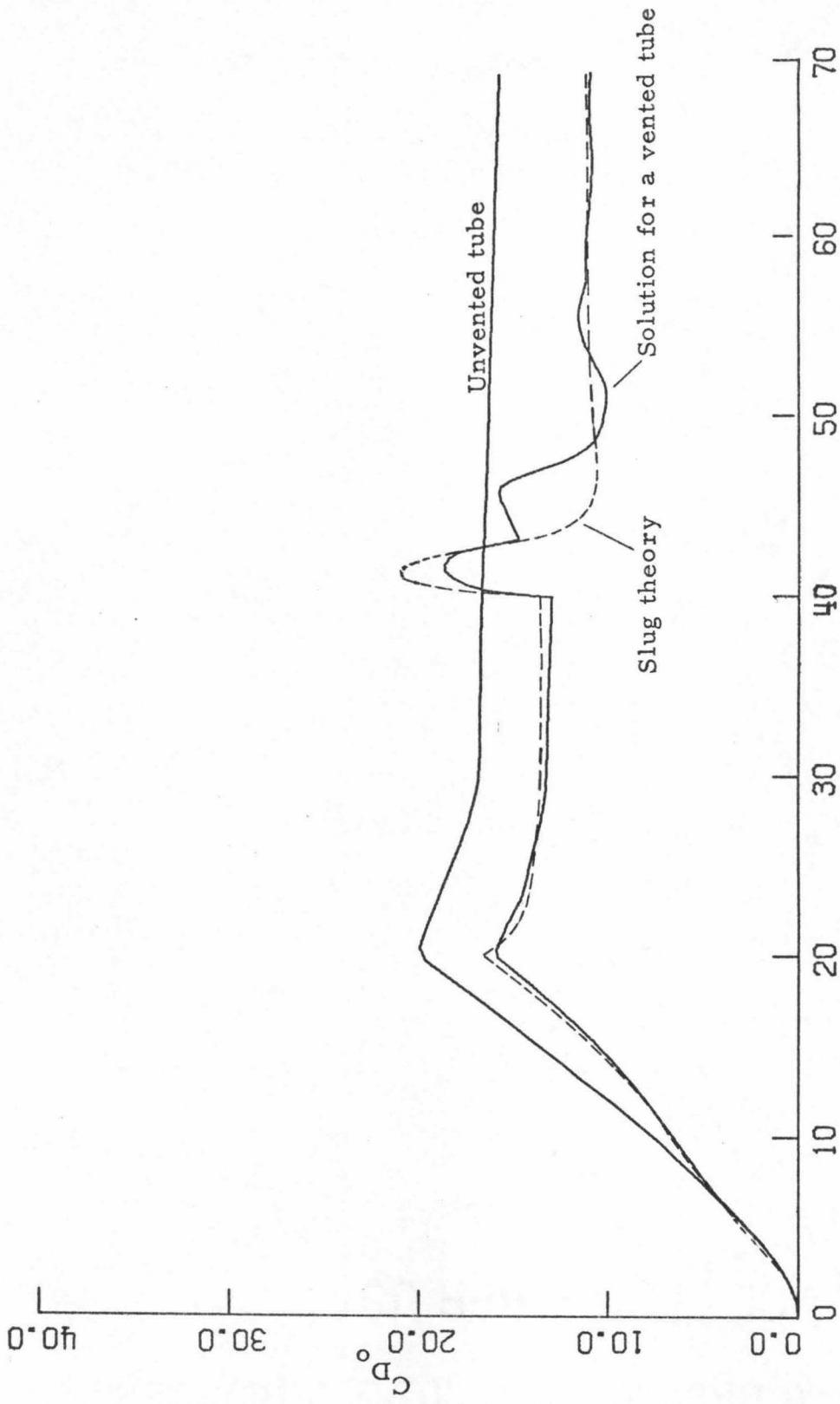

Fig. 28 Comparison of Drag Coefficients

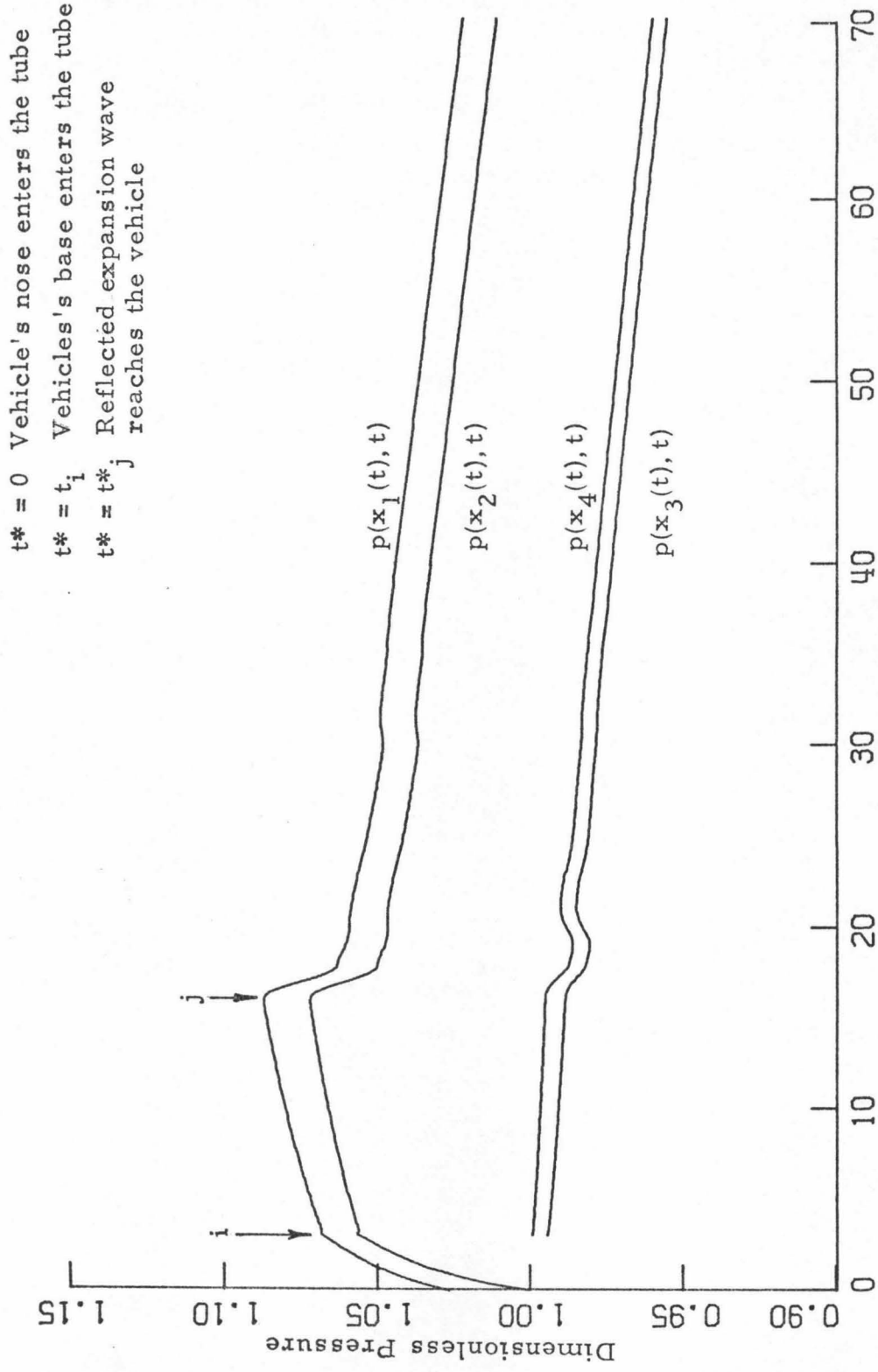

Fig. 29 The Variation of Pressure with Time for the Entry Problem

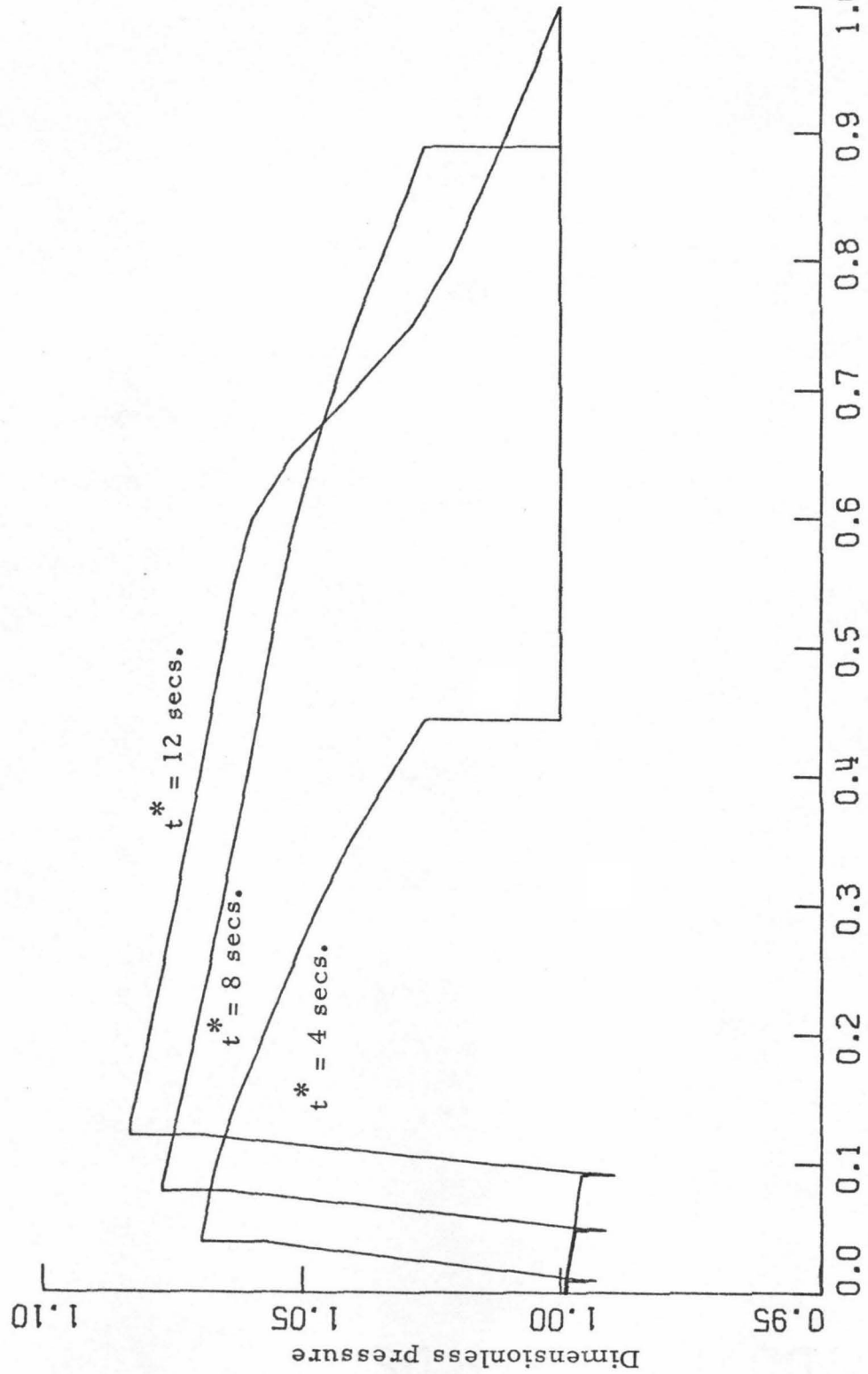

Fig. 30 The Pressure Variation along the Tube for the Entry Problem

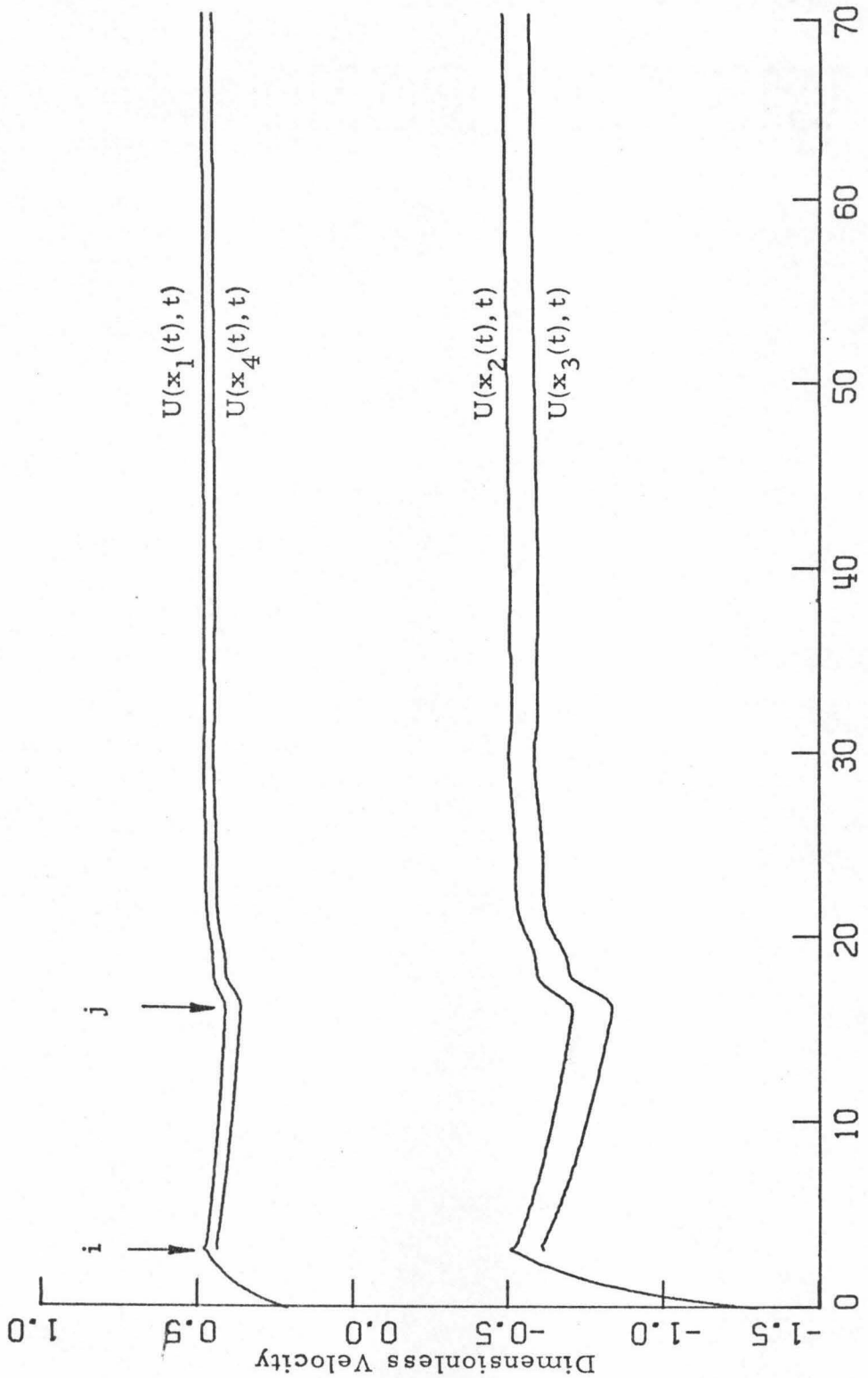

Fig. 31 The Flow Velocity Variation with Time for the Entry Problem

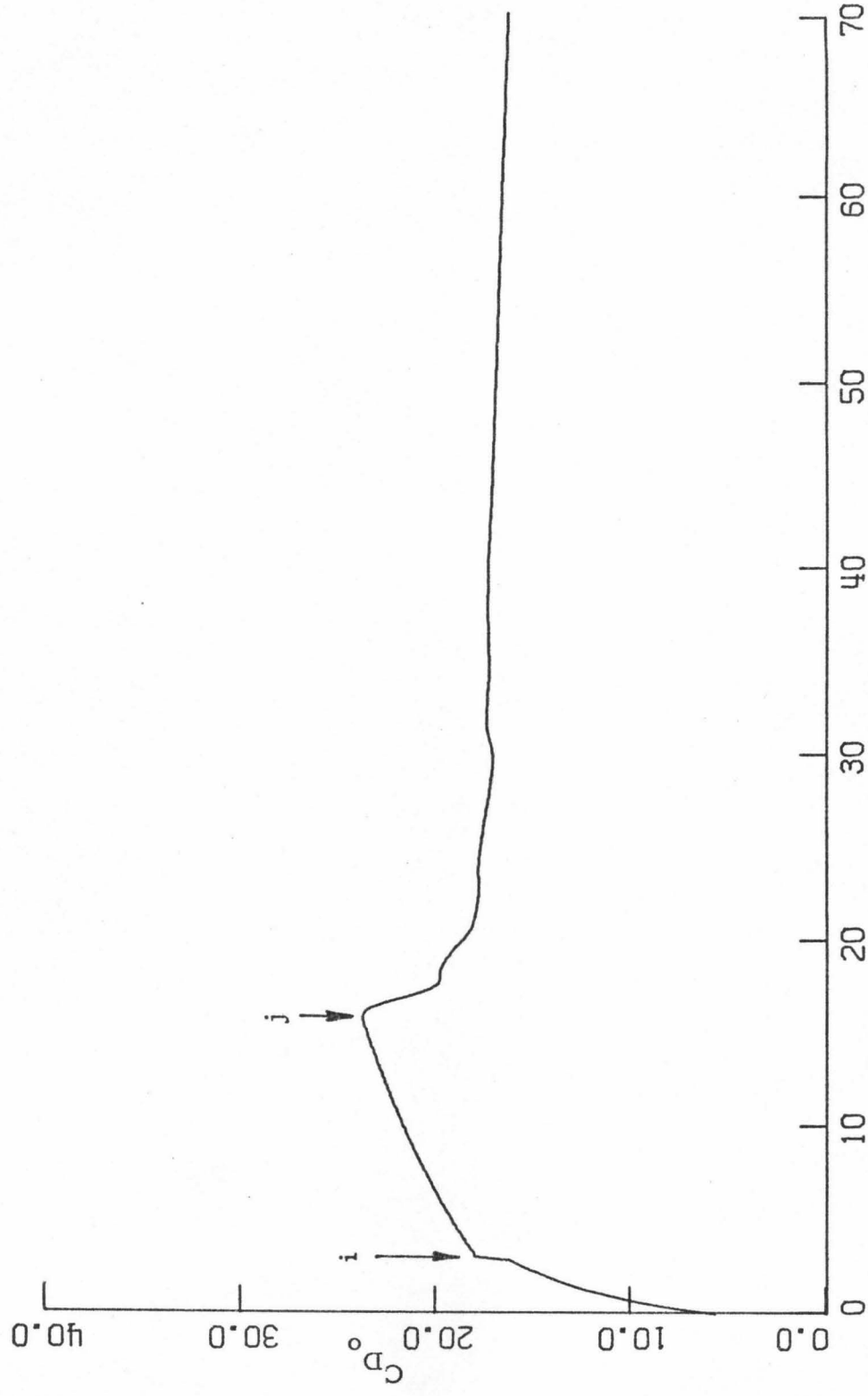

Fig. 32 The Drag Coefficient Variation with Time for the Entry Problem

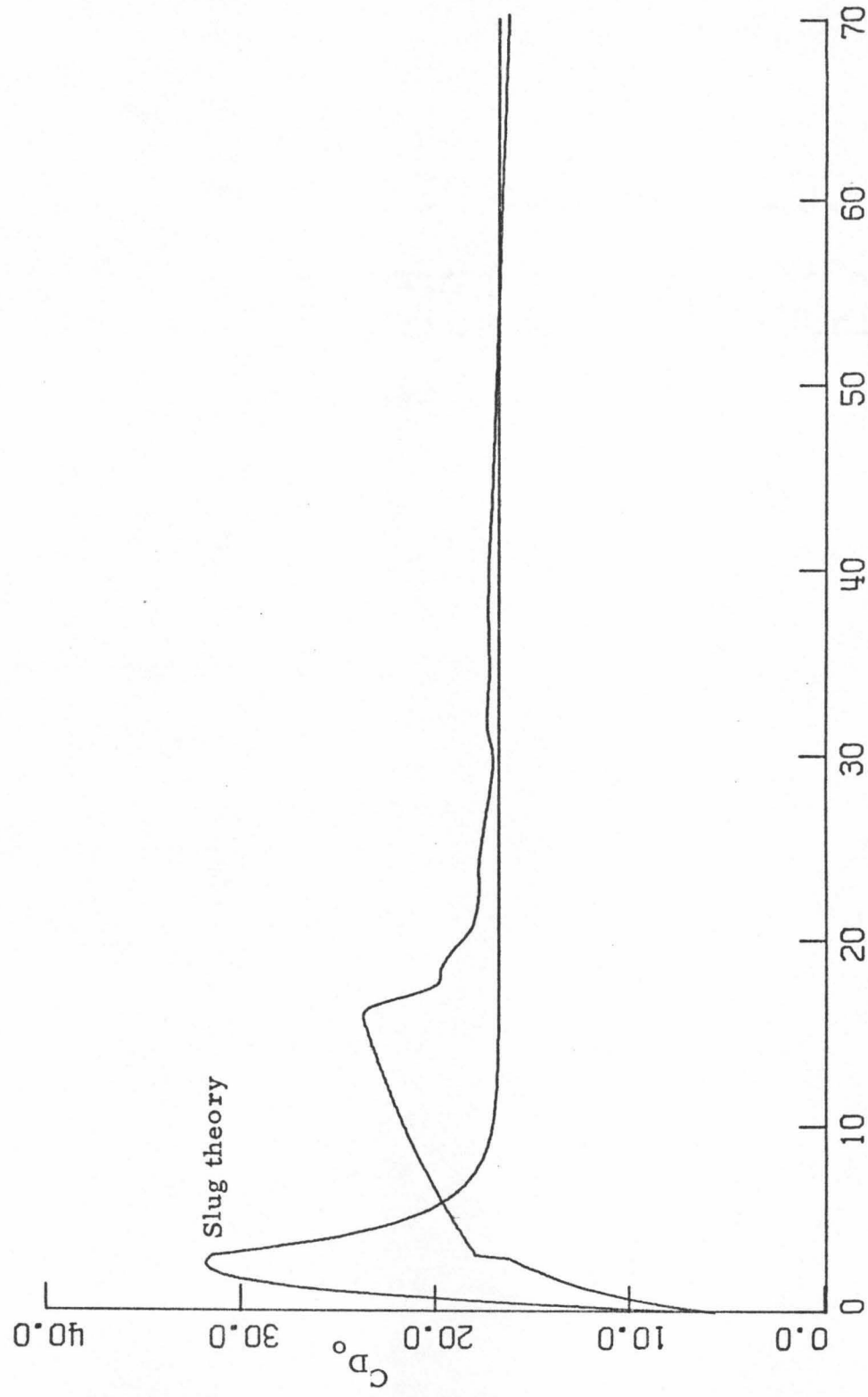

Fig. 33 Comparison of Drag Coefficients

APPENDIX A

Potential Solution of the Steady Tube-Vehicle Problem:

Using a point source and a point sink on the axis of a cylindrical tunnel, Lamb (Ref. 1A) solved the problem of a body (the Rankine "Ovoid") placed in a cylindrical wind tunnel. His solution is in terms of an infinite series involving Bessel functions. The convergence of the series is slow as the body is approached and becomes unsuitable for calculations close to the point sources. Watson (Ref. 2A) expressed the previous series in a new form which is convergent for x and r values satisfying the condition*

$$r^2 + (x-x_s)^2 < 4W^2$$

r, x are respectively the radial and axial coordinates. The source position is given by $(x_s, 0)$ and W is the radius of the tunnel. We are interested in finding the flow properties in the vicinity of the body. However, as the distance between the point source and the point sink placed on the x-axis is in general great enough so that Watson's series may not be applied, we consider solving the problem by using a distribution of ring (band) sources and sinks on the tube wall.

We are considering axially symmetric flow. We therefore deal with the Stokes' stream function ψ. In terms of this stream function the axial and radial flow velocity components are respectively given by

$$u = \frac{1}{r} \frac{\partial \psi}{\partial r}$$

$$v = -\frac{1}{r} \frac{\partial \psi}{\partial x}$$

---

* Symbols in this Appendix represent dimensional quantities

Fig. (1A) represents a ring source of radius R_R and width $x_o\ x_1$ with its axis coincident with the x-axis. Consider a point (x, r) lying on the circumference of disc (c) having radius r and centered at point (x, 0). The value $(2\pi\psi)$ at point (x, r) due to the ring source is equal to the volumetric flow rate discharged through disc (c). This flow rate is found by considering the contribution of the line source ab. The total discharge due to the ring is then found by integrating the contributions of all such elements comprising the ring. The following expressions are obtained. We represent the ring source strength density ($(ft^3/sec)/ft^2$) by P.

$$\psi_{ring} \equiv \psi(x, r; x_o, x_1, R_R, P) =$$

$$P\frac{R_R}{2\pi}\left\{\sqrt{(r+R_R)^2 + (x-x_s)^2}\,E + \frac{r-R_R}{\sqrt{(r+R_R)^2+(x-x_s)^2}}\left[(r+R_R)F + \frac{(x-x_s)^2}{r+R}\Pi\right]\right\}_{s=0}^{s=1}$$

$$, \quad r < R_R$$

$$\psi_{ring} \equiv (x, r; x_0, x_1, R_R, P) =$$

$$P\frac{R_R^2}{\pi}\left\{-\frac{\pi}{4}\,\frac{|x-x_s|}{R_R} + \frac{1}{k_s}\,E\right\}_{s=0}^{s=1} , \qquad r = R_R$$

$$u(x, r; x_0, x_1, R_R, p) =$$

$$P\,\frac{R_R}{\pi}\left\{\frac{1}{\sqrt{(r+R_R)^2+(x-x_s)^2}}\,F\right\}_{s=0}^{s=1} , \qquad r \le R_R$$

$$v(x, r; x_0, x_1, R_R, P) =$$

$$\frac{P}{4\pi}\sqrt{\frac{R_R}{r}}\left\{k_s \frac{(x-x_s)}{r}\left[\frac{R_R - r}{R_R + r}\,\Pi - F\right]\right\}_{s=0}^{s=1} ,$$

$$r < R_R$$

$$v(x, r; x_0, x_1, R_R, P) =$$

$$\frac{P}{4\pi}\left\{\pi\, \mathrm{sgn}(x-x_s) - \frac{(x-x_s)}{R_R}\, k_s\, F\right\}_{s=0}^{s=1} ,$$

$$r = R_R$$

where

$$k_s \equiv \sqrt{\frac{4r\,R_R}{(r+R_R)^2+(x-x_s)^2}}$$

$$\alpha^2 \equiv \frac{4r\,R_R}{(r+R_R)^2}$$

$F \equiv F(\frac{\pi}{2}, k_s)$ (elliptic integral of the first kind)

$E \equiv E(\frac{\pi}{2}, k_s)$ (elliptic integral of the second kind)

$\Pi \equiv \Pi(\frac{\pi}{2}, \alpha^2, k_s)$ (elliptic integral of the third kind)

$$\{\varphi\}_{s=0}^{s=1} \equiv \varphi\big|_{\text{evaluated at } s=1} - \varphi\big|_{\text{evaluated at } s=0}$$

The corresponding expressions for the stream function and the velocity components at a point (x, r) due to a point source of strength Q at point (x, 0) are

$$\psi_{source} \equiv \psi(x, r; x_s, Q) = -\frac{Q}{4\pi}\,\frac{x-x_s}{\sqrt{r^2 + (x-x_s)^2}}$$

$$u(x, r; x_s, Q) = \frac{Q}{4\pi} \frac{x - x_s}{[r^2 + (x-x_s)^2]^{3/2}}$$

$$v(x, r; x_s, Q) = \frac{Q}{4\pi} \frac{r}{[r^2 + (x-x_s)^2]^{3/2}}$$

and for a uniform flow with velocity $u = -U_\infty$

$$\psi(x, r) = -U_\infty \frac{r^2}{2}$$

$$u = U_\infty$$

$$v = 0$$

We assume 2n ring (band) sources of equal width are located on the tube wall which is of radius W (see Fig. 2A). In addition a source and sink of strengths $\pm Q$ are symmetrically located on the x-axis with respect to the plane x = 0. To find the ring source densities $P^{(i)}$ and the point source strength Q, n+1 linear algebraic equations need to be solved. n equations represent the condition that a single streamline coincides with the tube wall at n different points. The final equation specifies the vehicle's radius in the plane x = 0. The equations are given by

$$\sum_{i=1}^{2n} \psi_{ring}^{(i)} + \psi_{source} + \psi_{sink} = 0$$

$$\text{at } (x_j, W), \quad j = 1, 2, \ldots, n$$

$$\sum_{i=1}^{2n} \psi_{ring}^{(i)} + \psi_{source} + \psi_{sink} = r^2 \frac{U_\infty}{2}$$

$$\text{at } (0, R_v)$$

The body surface is that at which

$$\psi = 0$$

The pressure p at a point is given by

$$\frac{p - p_\infty}{\frac{1}{2} \rho U_\infty^2} = 1 - \frac{u^2 + v^2}{U_\infty^2}$$

Figure (3A) depicts the body shape (the surface $r = R_B(x)$ satisfying the relation $\psi = 0$) resulting when the blockage ratio $(R_v / W)^2 = 0.7$. In this case the point source and the point sink were located on the x-axis with respective coordinates 5 and -5. Both figures (4A) and (5A) which depict pressure and velocity variations across the tube indicate that the effect of the body on the uniform flow in the tube extends only a short distance ahead of the body.

References

1A Lamb, H., "On the Effect of the Walls of an Experimental Tank on the Resistance of a Model," Aeronautical Research Committee, Reports and Memoranda, No. 1010, 1926.

2A Watson, G. N., "The Use of Series of Bessel Functions in Problems Connected with Cylindrical Wind-Tunnels," Proc. Roy. Soc., Series A, Vol. 130, 1930-31, pp. 29-37.

3A Li, W. H., Lam, S. H., "Principles of Fluid Mechanics," Addison-Wesley Publishing Company, Inc., 1964.

4A Gradshteyn, I. S., Ryzhik, I. M., "Tables of Integrals Series and Products," Academic Press, Fourth Edition, 1965.

5A Byrd, P. F., Friedman, M. D., "Handbook of Elliptic Integrals for Engineers and Scientists," Springer-Verlag, Second Edition, 1971.

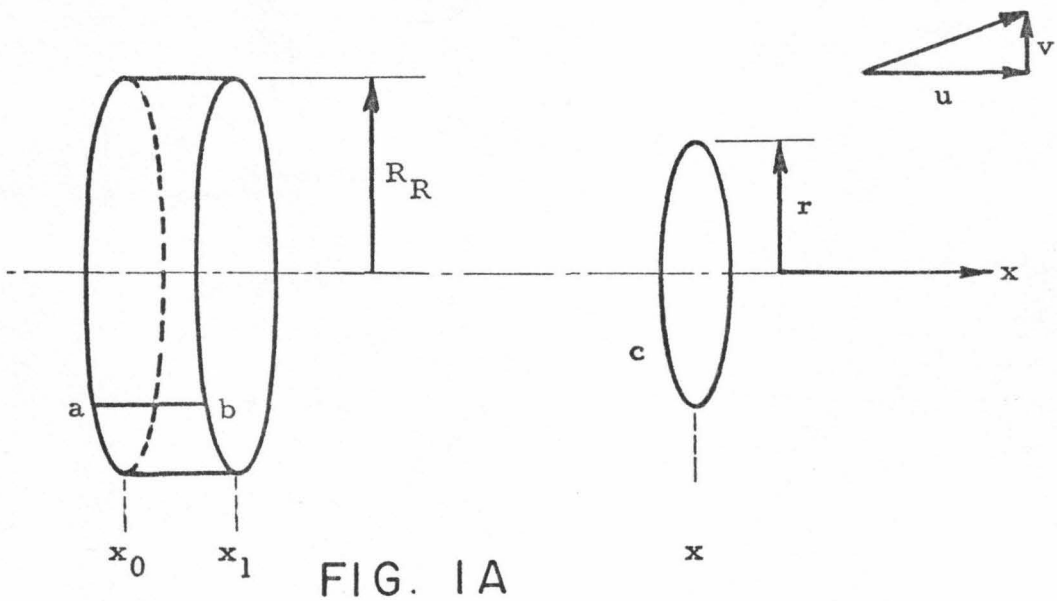

FIG. 1A

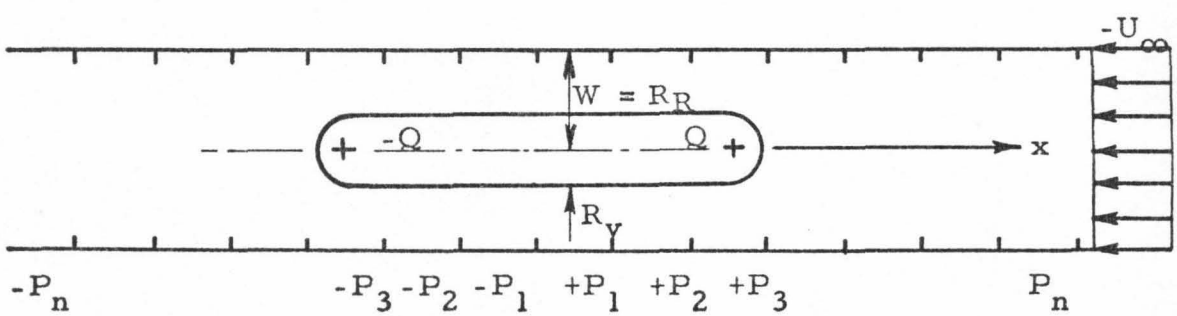

FIG. 2A

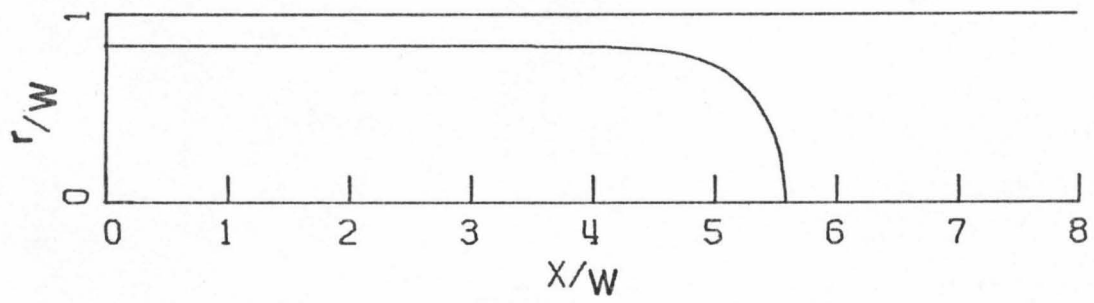

VEHICLE PROFILE

FIG. 3A

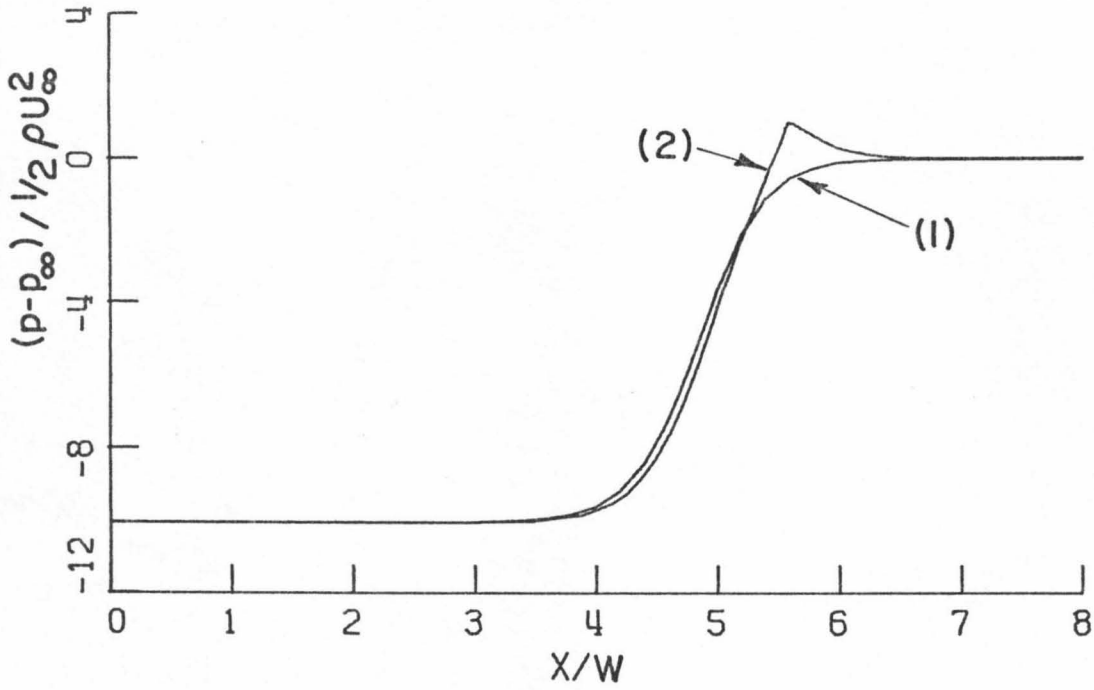

(1) PRESSURE DISTRIBUTION ALONG THE SURFACE $r/W = 0.94$

(2) PRESSURE DISTRIBUTION ALONG VEHICLE'S SURFACE AND THE X-AXIS AHEAD

FIG. 4A

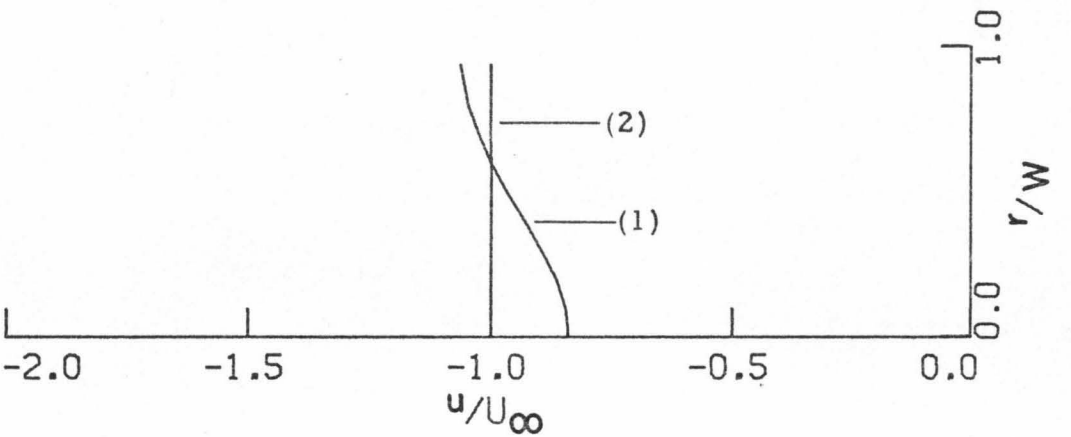

(1) FLOW VELOCITY PROFILE AT X/W =6.0

(2) FLOW VELOCITY PROFILE AT X/W =7.5

FIG. 5A

APPENDIX B

A Rough Estimate for the Boundary Layer Growth in the Tube

An idea about the time required for the boundary layer to fill the tube is obtained by considering a simple flow model. An incompressible flow is assumed to begin its motion from rest in an infinitely long tube. A boundary layer extends from the wall in the y-direction (see Fig. 1B), decreasing the radius $R^*(t)$(†) of the uniform inviscid core with time. The velocity distribution $u^*(r^*, t^*)$ in the boundary layer is related to the core velocity $\hat{U}(t^*)$ through the relation

$$\frac{u^*(r^*, t^*)}{\hat{U}^*(t^*)} = f(\eta) , \qquad \eta = \frac{y^*}{\delta^*}$$

where δ^* is the boundary layer thickness, and

$$y^* = W^* - r^*$$

W^* is the tube radius

The average flow velocity $U^*(t^*)$ is assumed to be known.

We introduce the following dimensionless quantities

$$r = \frac{r^*}{W^*} \qquad \bar{x} = \frac{x^*}{W^*} \qquad \bar{t} = t^* \frac{U_o^*}{W^*}$$

$$\bar{u} = \frac{u^*}{U_o^*} \qquad \bar{\tau} = \frac{\tau^*}{\rho_o^* U_o^{*2}}$$

where U_o^* is the final value for $U^*(t^*)$.

The momentum equation in dimensionless form is

$$\frac{\partial}{\partial \bar{t}} (r \bar{u}) = \frac{\partial}{\partial \bar{t}} (r \bar{U}) + \frac{\partial}{\partial r} (r \bar{\tau})$$

(†) Starred symbols represent dimensional quantities.

Integrating across the tube we get

$$\beta_1 \bar{\hat{U}}_t + \beta_1' \delta_t \bar{\hat{U}} = -2 \bar{\tau}_o \tag{1B}$$

where $\tau_o \equiv \bar{\tau}(W,t)$

$$\beta_1 \equiv 2(1-I_1)\delta - (1-2I_2)\delta^2$$

$$\beta_1' \equiv \frac{d\beta_1}{d\delta} = 2(1-I_1) - 2(1-2I_2)\delta$$

$$I_1 \equiv \int_o^1 f(\eta)d\eta$$

$$I_2 \equiv \int_o^1 f(\eta)d\eta$$

Substituting the relation

$$\bar{\hat{U}} = \frac{\bar{U}}{1-\beta_1}$$

into equation (1B) we get

$$\delta_t = \frac{-\beta_1 \bar{U}_t(1-\beta_1) - 2\bar{\tau}_o (1-\beta_1)^2}{\bar{U}\,\beta_1'}$$

The above equation is integrated numerically for a few examples. The average flow velocity $U^*(t^*)$ is assumed to increase with a constant acceleration e^* for $t^* < 20$ seconds, after which the flow is assumed to move with the final average velocity U_o^*. The velocity profile $f(\eta)$ is assumed to be of the form

$$f(\eta) = \eta^{\frac{1}{n}}$$

and the wall is assumed to have a friction factor

$$f_T = - \frac{\tau_o^*}{\frac{1}{2} \rho^* U^{*2}}$$

We take $W^* = 8$ ft.

Figures (2B), (3B), (4B) respectively show the rate of boundary layer growth for different values of the parameters e^*, n, f_T. It is seen from these estimates that the time required for the boundary layer to fill the tube is of order 20 seconds. This is comparable to the period of vehicle acceleration in which the maximum drag is experienced. It seems, therefore, of importance to investigate the effects of the boundary layer growth period.

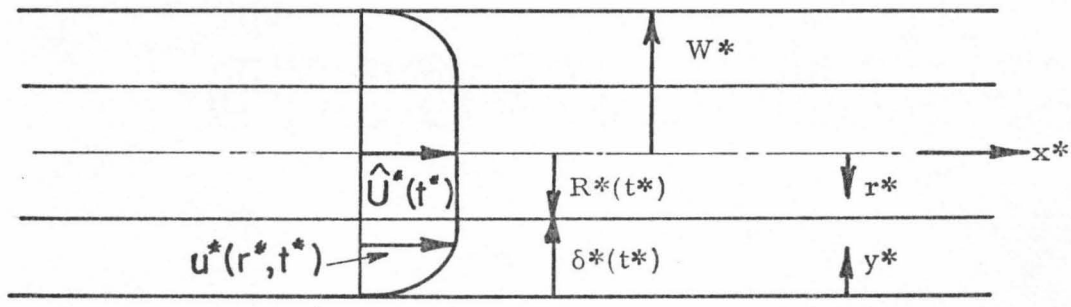
W*
x*
$\hat{U}^*(t^*)$
R*(t*)
r*
$u^*(r^*,t^*)$
δ*(t*)
y*

FIG. 1B

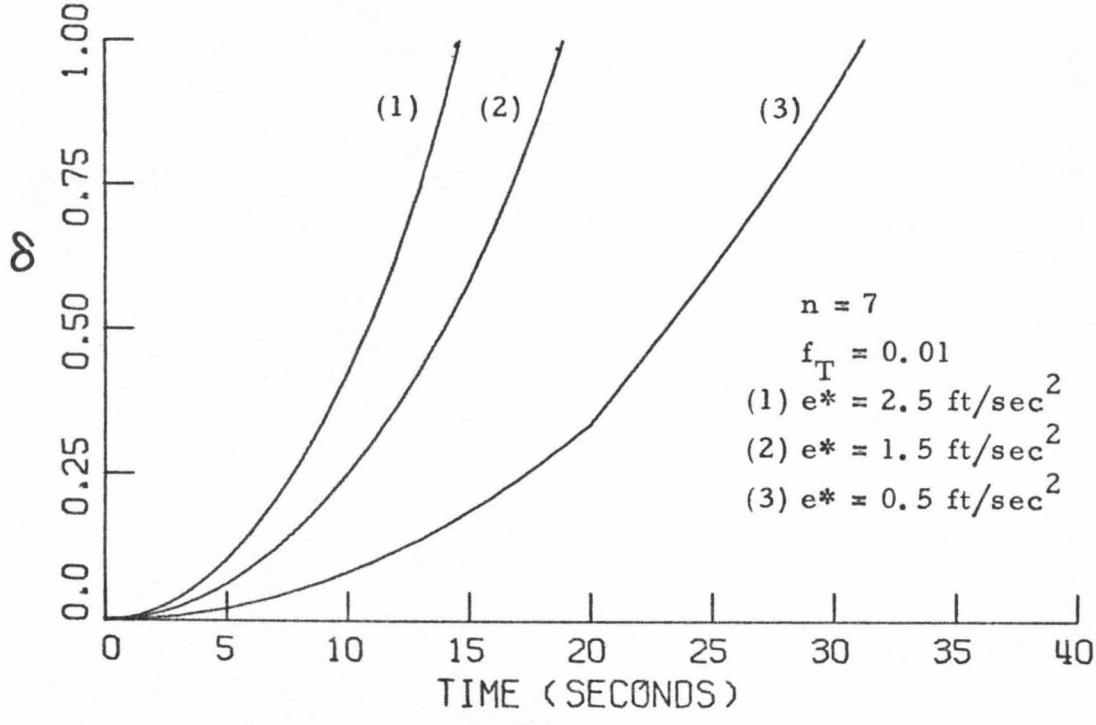
δ
0.0
0.25
0.50
0.75
1.00
(1)
(2)
(3)
n = 7
f_T = 0.01
(1) e* = 2.5 ft/sec^2
(2) e* = 1.5 ft/sec^2
(3) e* = 0.5 ft/sec^2
0
5
10
15
20
25
30
35
40
TIME (SECONDS)

FIG. 2B

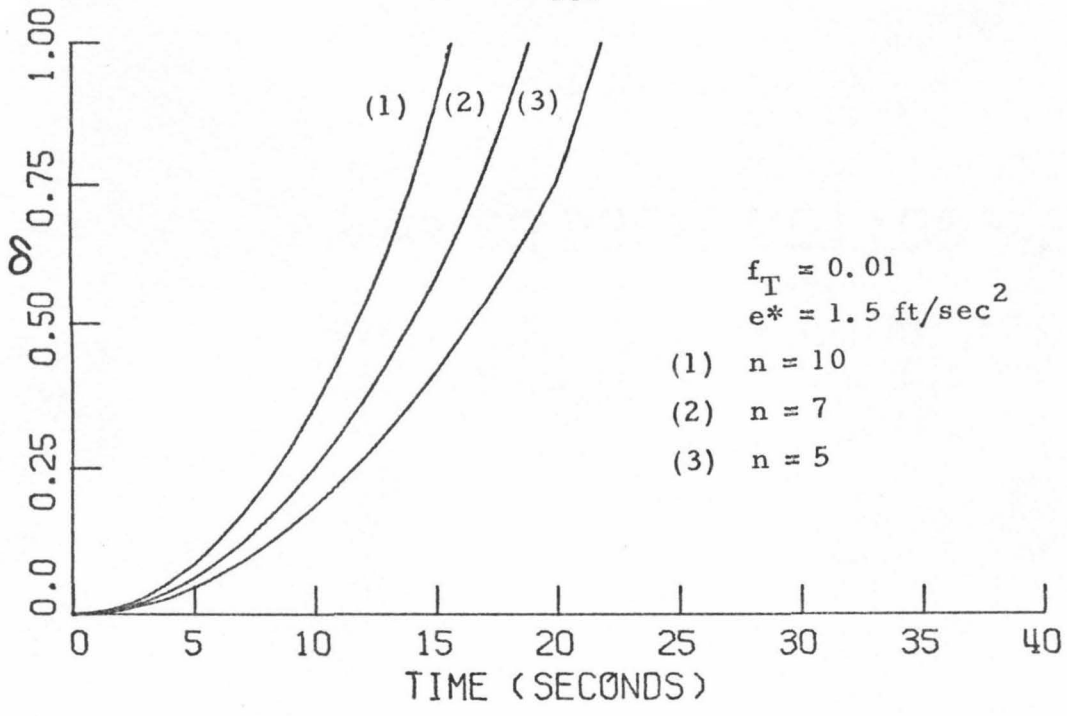
1.00
0.75
0.50
0.25
0.0
δ
(1)
(2)
(3)
f_T = 0.01
e* = 1.5 ft/sec^2
(1) n = 10
(2) n = 7
(3) n = 5
0
5
10
15
20
25
30
35
40
TIME (SECONDS)

FIG. 3B

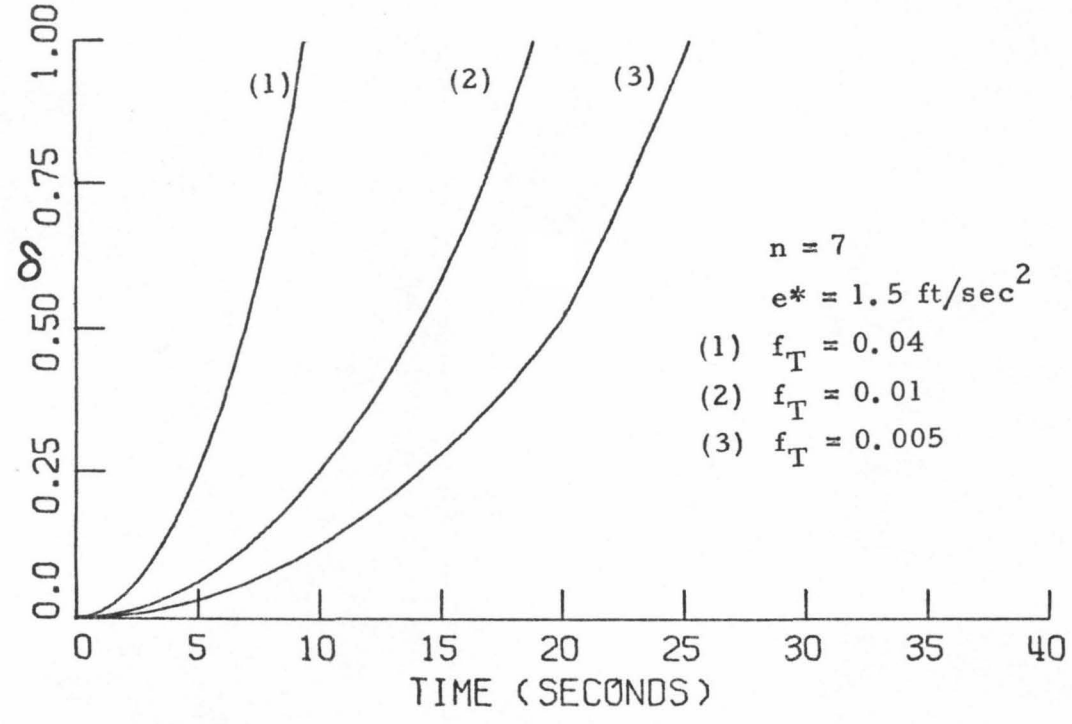
1.00
0.75
0.50
0.25
0.0
δ
(1)
(2)
(3)
n = 7
e* = 1.5 ft/sec^2
(1) f_T = 0.04
(2) f_T = 0.01
(3) f_T = 0.005
0
5
10
15
20
25
30
35
40
TIME (SECONDS)

FIG. 4B